3. SITE 1071[1]

Shipboard Scientific Party[2]

HOLE 1071A

Position: 39°22.9446′N, 72°43.6830′W

Start hole: 1300 hr, 23 June 1997

End hole: 0355 hr, 24 June 1997

Time on hole: 14.92 hr

Seafloor (drill pipe measurement from rig floor, mbrf): 99.4

Total depth (drill pipe measurement from rig floor, mbrf): 151.3

Distance between rig floor and sea level (m): 11.2

Water depth (drill pipe measurement from sea level, m): 88.2

Penetration (mbsf): 51.9

Coring totals:
    Type: APC
    Number: 7
    Cored: 36.3 m
    Recovered: 27.75 m (76.45%)

    Type: XCB
    Number: 3
    Cored: 15.6 m
    Recovered: 1.1 m (7.05%)

Lithology:
    Unit I: 0–51.9 mbsf; Holocene(?) to Pleistocene
    Dark gray to dark greenish gray clay, dark gray silty clay and clayey silt, and olive gray to dark olive sand

HOLE 1071B

Position: 39°22.9477′N, 72°43.6789′W

Start hole: 0945 hr, 25 June 1997

End hole: 0115 hr, 26 June 1997

Time on hole: 15.5 hr

Seafloor (drill pipe measurement from rig floor, mbrf): 99.4

Total depth (drill pipe measurement from rig floor, mbrf): 176.8

Distance between rig floor and sea level (m): 11.2

Water depth (drill pipe measurement from sea level, m): 88.2

Penetration (mbsf): 77.4

Coring totals:
    Type: W
    Number: 1
    Cored: not applicable
    Recovered: not applicable

---

[1]Austin, J.A., Jr., Christie-Blick, N., Malone, M.J., et al., 1998. *Proc. ODP, Init. Repts.,* 174A: College Station, TX (Ocean Drilling Program).
[2]Shipboard Scientific Party is given in the list preceding the Table of Contents.

Type: XCB
Number: 5
Cored: 37.6 m
Recovered: 11 m (29.3%)

Lithology:
    Unit I: 39.8–77.4 mbsf; Holocene(?) to Pleistocene
    Dark gray to dark greenish gray clay, dark gray silty clay and clayey silt, and olive gray to dark olive sand

HOLE 1071C

Position: 39°22.9486′N, 72°43.6827′W

Start hole: 2035 hr, 26 June 1997

End hole: 0500 hr, 29 June 1997

Time on hole: 56.42 hr (2.36 days)

Seafloor (drill pipe measurement from rig floor, mbrf): 99.4

Total depth (drill pipe measurement from rig floor, mbrf): 356.8

Distance between rig floor and sea level (m): 11.3

Water depth (drill pipe measurement from sea level, m): 88.1

Penetration (mbsf): 257.4

Coring totals:
    Type: W
    Number: 1
    Cored: not applicable
    Recovered: not applicable

    Type: XCB
    Number: 26
    Cored: 199.0 m
    Recovered: 67.55 m (33.94%)

Lithology:
    Unit I: 58.4–134.41 mbsf; Holocene(?), Pleistocene to late Pliocene(?)
    Dark gray to dark greenish gray clay, dark gray silty clay and clayey silt, and olive gray to dark olive sand

    Unit II: 134.41–256.74 mbsf; early Pliocene to late Miocene
    Very dark gray to dark greenish and brownish gray, bioturbated silty clay; dark gray bioturbated silty to sandy clay, bioturbated clayey to sandy silt, and dark greenish gray to olive gray pebbly glauconitic muddy to silty sand

HOLE 1071D

Position: 39°22.9449′N, 72°43.6888′W

Start hole: 2100 hr, 7 July 1997

End hole: 1240 hr, 8 July 1997

Time on hole: 15.67 hr

Seafloor (drill pipe measurement from rig floor, mbrf): 99.4

Total depth (drill pipe measurement from rig floor, mbrf): 185.1

Distance between rig floor and sea level (m): 11.4

Water depth (drill pipe measurement from sea level, m): 88.0

Penetration (mbsf): 85.7

Coring totals:
    Type: RCB
    Number: 12
    Cored: 85.7 m
    Recovered: 3.98 m (4.64%)

Lithology:
    Unit I: 0–66.9 mbsf; Holocene(?) to Pleistocene
    Dark gray silty clay

HOLE 1071E

Position: 39°22.9410′N, 72°43.6831′W

Start hole: 1510 hr, 8 July 1997

End hole: 2015 hr, 9 July 1997

Time on hole: 29.08 hr (1.21 days)

Seafloor (drill pipe measurement from rig floor, mbrf): 99

Total depth (drill pipe measurement from rig floor, mbrf): 358.8

Distance between rig floor and sea level (m): 11.4

Water depth (drill pipe measurement from sea level, m): 87.6

Penetration (mbsf): 259.8

HOLE 1071F

Position: 39°22.9321′N, 72°42.9398′W

Start hole: 0027 hr, 10 July 1997

End hole: 0840 hr, 12 July 1997

Time on hole: 56.22 hr (2.34 days)

Seafloor (drill pipe measurement from rig floor, mbrf): 101.5

Total depth (drill pipe measurement from rig floor, mbrf): 525.7

Distance between rig floor and sea level (m): 11.5

Water depth (drill pipe measurement from sea level, m): 90

Penetration (mbsf): 424.2

Coring totals:
    Type: RCB
    Number: 16
    Cored: 148.5 m
    Recovered: 20.07 m (13.52%)

Lithology:
    Unit II: 252–261.9 mbsf; late Miocene
    Very dark gray silty clay

    Unit III: 261.9–414.91 mbsf; late to middle Miocene
    Dark gray muddy sand with sandy mud; olive gray silty clay; gray pebbly siltstone

HOLE 1071G

Position: 39°22.9374′N, 72°42.9334′W

Start hole: 1247 hr, 12 July 1997

End hole: 0400 hr, 13 July 1997

Time on hole: 15.22 hr

Seafloor (drill pipe measurement from rig floor, mbrf): 101.5

Total depth (drill pipe measurement from rig floor, mbrf): 196.60

Distance between rig floor and sea level (m): 11.5

Water depth (drill pipe measurement from sea level, m): 90

Penetration (mbsf): 95.10

Comments: Logging while Drilling (LWD); no coring attempted

Principal results: Site 1071 is one of two sites approved for *JOIDES Resolution* drilling on the New Jersey continental shelf; these sites form part of a transect of holes from the slope (ODP Leg 150) to coastal outcrops (150X and 174AX) that constitute the Mid-Atlantic Sea-level Transect. The primary goals of the transect are (1) to date sequence boundaries of Oligocene to Holocene age and compare this stratigraphic record with the timing of glacial-eustatic changes inferred from deep-sea $\delta^{18}O$ variations; (2) to place constraints on the amplitudes and rates of sea-level change that may have been responsible for unconformity development; (3) to assess the relationships between depositional facies and sequence architecture; and (4) to provide a baseline for future scientific ocean drilling that will address the effects and timing of sea-level changes on this and other passive margins. Site 1071 provides information primarily about late middle Miocene and younger sequences at locations landward of their respective rollovers/breakpoints, the positions at which each sequence boundary steepens seaward into a clinoform.

The succession drilled and sampled at Site 1071 is divisible into four unconformity-bounded sequences of late middle Miocene to Pleistocene age. The sequence boundaries are characterized in seismic-reflection data by offlap; the sequences are arranged in a forestepping (overall progradational) pattern. The boundaries are informally designated, from youngest to oldest, as pp3(s), pp4(s), m0.5(s), and m1(s). The "s" designation following the "pp" (provisionally Pliocene/Pleistocene) and "m" (provisionally Miocene) sequence boundary identifications is meant to distinguish the shelf sequence boundaries, targeted for sampling and logging by Leg 174A, from similarly labeled and approximately correlative surfaces recognized on the slope by Leg 150 (Mountain, Miller, Blum, et al., 1994). A fifth seismic surface (pp5[s]), tentatively interpreted as a sequence boundary prespud, is reinterpreted as a flooding surface or interval of upward deepening. Site 1071 is not optimally located for dating these surfaces, but approximate ages are as follows: pp3(s), late Pleistocene (<0.78 Ma); pp4(s) = early Pleistocene–possibly latest Miocene (1.4–7.4 Ma); pp5(s) = latest Miocene (5.9–7.4 Ma); m0.5(s) = late Miocene (>7.4 Ma and probably >8.6 Ma); and m1(s) = late middle Miocene (>11.4 Ma).

The succession consists largely of sands, silts, and clays, with recovery predominantly from muddy intervals. The presence of sands in poorly recovered or unrecovered intervals is inferred by comparison with the gamma-ray log for the Continental Offshore Stratigraphic Test (COST-B2) well, which was drilled ~950 m to the southwest of Holes 1071A–1071E (a direction approximately parallel to depositional strike). These sediments have been divided into three lithostratigraphic units, primarily on the basis of abrupt changes in the vertical arrangement of lithofacies within the succession. Unit I (0–134.4 mbsf) is significantly less glauconitic overall than Unit II (143.5–261.9 mbsf), but sediments at the bases of both units are particularly glauconitic. Unit II is also characterized by significantly less calcite than Unit I. The recovered succession from Unit III (261.9–414.91 mbsf) is predominately silty and muddy sands. The base of Unit I corresponds approximately with sequence boundary pp4(s), the base of Unit II is thought to lie no more than a few meters above surface m0.5(s), and the base of Subunit III lies at or slightly below surface m1(s). The physical sedimentology, extensive bioturbation in fine-grained sediments, scattered shell fragments, benthic foraminifers, and local abundance of glauconite suggest that the succession is primarily shallow marine, with cyclicity at several scales related to presumed transgression and regression of the shoreline. An unexpected pattern to emerge for a location close to the modern shelf edge is that the preserved parts of sequences below both pp3(s) and pp4(s) are predominantly transgressive

overall, consistent with pronounced bypassing and erosion at both of these surfaces. Regional seismic data crossing the shelf near the site indicate that transgressive deposits thin seaward across their respective clinoform rollovers/breakpoints, beneath seaward-thickening and offlapping highstand units (regressive). Increasing amounts of offlap of successive sequence boundaries are consistent with increasing amplitudes of glacial-eustatic change from the late Miocene onward (~12–0 Ma).

Biostratigraphic resolution at Site 1071 is generally low for calcareous microfossils as a result of strong carbonate dissolution and shallow-water conditions that were unfavorable to these planktonic organisms. Nannofossils provide relatively useful zonations for the late Pleistocene, late Pliocene, and the early Pliocene–late Miocene. Utility of planktonic foraminifers for biostratigraphic zonation is restricted to the earliest Pliocene–middle Miocene. Pleistocene samples examined from Site 1071 yield benthic foraminiferal faunas that vary from inner neritic (0–50 m) assemblages, dominated almost exclusively by *Elphidium excavatum,* to more diverse upper middle neritic (~50–65 m) assemblages. These variations may reflect paleodepth fluctuations or substrates of diverse grain size, perhaps related to glacial/interglacial cycles. Miocene benthic foraminifer assemblages indicate middle neritic paleodepths (50–100 m), possibly with fluctuations within this depth zone. Organic microfossils also constrain the biostratigraphic framework at this site. Pollen is useful for dating middle to upper Pleistocene sediments; dinocysts provide biostratigraphic zonation of the early Pleistocene to late middle Miocene. Dinocysts suggest rapid sedimentation during the middle through late Pleistocene, the late late Miocene, and the early late Miocene. In contrast, hiatuses were identified in the Pliocene through early Pleistocene, middle late Miocene, and late middle Miocene, suggesting that hiatuses during these intervals correspond to stratigraphic surfaces pp4(s), m0.5(s), and m1(s).

Magnetic polarity was determined from magnetic inclination of archive-half samples after AF demagnetization at 20 mT and was also supported by a progressive AF-demagnetization experiment up to 80 mT on discrete-cube samples that were taken at a rate of one per section. Magnetic polarity changes downhole from normal to reverse at 61.5 mbsf in Hole 1071B and at 61.3–61.4 mbsf in Hole 1071C, which was confirmed by analyses of discrete-cube samples. Combined with the analysis of calcareous nannofossils, this reversal is considered to be the Brunhes/Matuyama (B/M) boundary (0.78 Ma). Magnetic polarity returns to normal at Cores 174A-1071B-6X and 174A-1071C-3X; however, the B/M boundary was not determined because of low recovery in this interval. No reversed-polarity chron was found downhole, which does not necessarily mean that the polarity is normal, but that remagnetization may have occurred during the Brunhes Chron. Magnetization intensity after 20-mT AF demagnetization drops from 10 to 100 mA/m above the B/M boundary to ~1 mA/m below the boundary. Magnetization intensity increases to >10 mA/m below 68 mbsf, fluctuating downhole, and then decreases to <1 mA/m below 200 mbsf. This low magnetization intensity may be related to the dissolution of magnetite and the formation of pyrite.

Routine squeezing of whole-round sediment samples shows complex and nonsteady-state interstitial water profiles. Pore waters are significantly fresher than seawater in two intervals, with minima at 30 mbsf and between 261 and 321 mbsf (Cl$^-$ to 431 mM at 26.45 mbsf, a 23% decrease, and 500 mM at 321 mbsf, an 11% decrease). These salinity minima likely reflect input of fresh (or brackish) water during late Pliocene–Pleistocene drops in sea level and subaerial exposure of the shelf. Pore waters show a rapid rise in alkalinity, ammonia, and phosphate below 150 mbsf, suggesting that substantial organic-matter diagenesis is occurring in this interval. Operations were highlighted by a spectacular fountain of water that flowed at pressure from the drill pipe upon reaching a depth of ~250 mbsf. The chemistry of fountain water is identical to that of surface seawater and significantly different from that of formation water. This strongly indicates that the fountain was caused by drilling procedures rather than direct drilling of a pressurized aquifer. A plausible explanation is that porous sand intervals were charged with pressurized water when unstable hole conditions caused cave-ins around shallower sections of the drill string.

Hydrocarbon gases were monitored by headspace sampling for every core, according to the safety guidelines for drilling in these water depths.

Concentrations of C_1 were below 9 ppmv, whereas those for C_2 through C_6 were at or below detection limits. The lack of hydrocarbon gas and the presence of interstitial water sulfate in cores at depth suggest that significant bacterial gas is not being generated in shallow sediment. Total organic carbon (TOC) increases downhole, averaging 0.3 wt% from 0 to 135 mbsf and 0.65 wt% from 135 mbsf to the base of the drilled section. Organic-matter degradation and siderite precipitation in Units II and III may be related to higher sediment TOC.

Physical properties of primary interest are density and *P*-wave velocity, which will aid in traveltime-depth conversion as well as production of synthetic seismograms for linking coring results to seismic reflections in both regional and site-specific profiles and logs. Density measurements were acquired at a variety of resolutions. Wet bulk-density data in Holes 1071A–1071C show a gradual overall increase consistent with effects of compaction; the greatest downhole increase in density appears in the upper 10 mbsf of Hole 1071A. Several smaller scale trends in density and velocity are approximately coincident with inferred lithologic boundaries. Although the *P*-wave logger on the multisensor track (MST) was turned off after the first few cores because of incompletely filled liners, discrete *P*-wave velocity measurements, primarily transverse to the core axis, were made with the same frequency as were index properties. Velocities are generally between 1600 and 1800 m/s. Intervals of uniform or gradually varying velocity are separated by abrupt changes at lithologic boundaries. The lithified sandstone at the base of Hole 1071C has a *P*-wave velocity in excess of 5000 m/s. It appears to be a thin layer, however, and its potential to generate a strong seismic reflection remains uncertain. In Hole 1071F, between ~359 and ~370 mbsf, velocities increase downhole from 1800 to 1900 m/s; below 370 mbsf velocities decrease downhole to 1700–1800 m/s. This velocity change at ~370 mbsf corresponds to the boundary between lithostratigraphic Subunits IIIA and IIIB and lies above the inferred position of sequence boundary m1(s). Natural gamma measurements were made on the MST at intervals of 20 cm. Coupled with discrete resistivity measurements (one to two per section), these will assist with future core-log correlations.

Logging-while-drilling (LWD) data were acquired at Site 1071 to a depth of only 88 mbsf at Hole 1071G, when unstable hole conditions prevented further penetration. However, log data acquired at the COST-B2 well, 950 m south-southwest of Holes 1071A–1071E, provided valuable indications of unrecovered lithology and depths to key horizons imaged in site-survey seismic profiles.

BACKGROUND AND OBJECTIVES

Site 1071 is the first of two sites drilled during Leg 174A on the outer continental shelf of the New Jersey margin, at a water depth of 88–90 m. Site 1071 is located ~130 km (77 nmi) east of Atlantic City, New Jersey, and ~40 km (25 nmi) north of Leg 150 Sites 902–904 and 906 on the continental slope. Holes 1071A–1071E are at the intersection of *Oceanus* 270 (Oc270) multichannel seismic (MCS) Profiles 885 and 806; and Holes 1071F and 1071G are located 1.1 km (0.6 nmi) to the east, at the intersection of Oc270 MCS Profiles 801 and 814. All holes are within the MAT-8B hazards grid. The geological context of this site, and a description of geophysical data supporting its selection, are described in the "Introduction" chapter (this volume).

Greenlee et al. (1992) used industry seismic-reflection and well data in the same area of the shelf to interpret unconformity-bounded sequences of Oligocene to Pleistocene age. Bounding surfaces in the Miocene and younger part of the succession were designated by colors (in ascending order): Green, Pink-2, Blue, Yellow-2, Tuscan, Yellow-1, Pink-1, and an unnamed surface. Recent mapping of sequence boundaries using Ew9009 and Oc270 MCS data reveals that, in the vicinity of Site 1071, Green and Pink-2 are ~m5.6(s) and m4(s) in a deep-shelf paleogeographic setting far seaward of their respective rollovers/breakpoints. (The term "rollover" or "breakpoint" is used here for the position at which the sequence boundary steepens

basinward into a clinoform; see "Introduction" chapter, this volume.) Blue is a surface that is close to but deeper than sequence boundaries m3(s), m2.5(s), and m2.3(s), which at the seismic resolution of the Oc270 data become amalgamated near Site 1071. Yellow-2 may be equivalent to m2.2(s), although the interpreted position of the rollover/breakpoint for m2.2(s) is landward of that indicated by Greenlee et al. (1992) for Yellow-2. Tuscan is m1(s). Site 1071 is located immediately seaward (<1 km in the case of Holes 1071A–1071E, and 1–2 km for Holes 1071F and 1071G) of the rollover/breakpoint for this latter surface, the primary target of drilling at Site 1071. Yellow-1 is reinterpreted in the vicinity of Site 1071 as a multiple with no primary stratigraphic significance. Pink-1 is m0.5(s). The unnamed sequence boundary of Greenlee et al. (1992) above Pink-1 is pp4(s). Above pp4(s), surface pp3(s) as identified on the Oc270 profiles was not interpreted by Greenlee et al. (1992). Boundaries m0.5(s), pp4(s), and pp3(s) are prominent offlap surfaces; each of them is landward of their rollovers/breakpoints at Site 1071. A final surface, informally designated pp5(s), was identified between pp4(s) and m0.5(s) and tentatively interpreted before Leg 174A as a sequence boundary on the basis of apparent onlap. An alternative interpretation is presented below (see "Summary and Conclusions" section, this chapter) on the basis of results at Site 1071. Pre-drill estimated depths for these surfaces are shown in the "Seismic Stratigraphy" section (this chapter).

The primary goals of Site 1071 are (1) to verify that the seismically identified and mapped surfaces are indeed sequence boundaries (mainly those intersected landward of their rollovers/breakpoints); (2) to attempt to date these surfaces and compare ages with those previously compiled by Miller et al. (1996); (3) to assess the relationships between depositional facies and sequence architecture; and (4) to place constraints on amplitudes and rates of sea-level change that may have been responsible for unconformity development. Site 1071 is specifically focused on the rollover/breakpoint of surface m1(s). It is also located close to the rollover/breakpoint for m0.5(s).

OPERATIONS

Transit To Site 1071

The vessel departed Halifax at 1812 hr on Friday, 20 June 1997. The 578-nmi transit to Site 1071 was accomplished at an average speed of 10.8 kt. The vessel arrived on location at 2330 hr on 22 June 1997. All times reported in the "Operations" sections in this volume are in local time (U.S. Eastern Time Zone; UTC – 4 hr).

Hole 1071A

Station Keeping

At 0009 hr on 23 June, the first beacon (14.0 kHz, 193 dB) was dropped on the dGPS coordinates for prospectus site MAT-8B3. During the process of stabilizing the ship on site, it became apparent that the automatic station keeping (ASK) system was experiencing short, unstable periods. At the time, it was assumed that strong bottom or eddy currents were causing the beacons to drift off location or flutter. Subsequently, it was determined that the beacon was dropped 20.7 m southwest of the intended location; this was assumed to be an artifact of an unstable dGPS signal (±20 m). Because the beacon's transmission signal angle provides a signal radius of ~15 m in 90-m water depth, the 20.7-m offset was considered unacceptable for shallow-water operations.

A second beacon (17.0 kHz, 193 dB), which was equipped with an iron bar through the anchor weight to prevent rolling, was dropped at 0302 hr; however, its signal was unstable. A third, more powerful beacon (15.0 kHz, 205 dB) was dropped at 0326 hr, but it had to be turned off because it was interfering with reception of the first beacon's signal. A fourth beacon (16.0 kHz, 198 dB) was dropped at 0720 hr; it landed ~12 m northeast of Hole 1071A, providing a dependable signal relative to previous beacons. However, the ASK system was still experiencing ~1.5-min unstable intervals when beacon

signals were poor, which was attributed to beacon motion in changing currents. Consequently, a stand, 1 m high, with an angle-iron square base and drill-string guide rings, was constructed out of scrap casing to place a beacon exactly on site and prevent its movement in currents. A fifth beacon (15.0 kHz, 193 dB) was placed in this stand and dropped to the seafloor along the pipe with the bit on bottom. Although the ASK system was still experiencing occasional signal losses from the two remaining active beacons, one in the stand and one on a tether, the improvement in the ship's dGPS system stability allowed coring operations to commence.

The advanced hydraulic piston corer (APC)/extended core barrel (XCB) bottom-hole assembly (BHA) was run to 78 m below rig floor (mbrf), followed by the vibration-isolated television (VIT) frame. A reference survey (video and sonar) was conducted on a 7.6-m square and revealed a clean, flat seafloor. The bit tagged a firm bottom at 99.4 mbrf (88.2 m below sea level [mbsl]), and Hole 1071A was spudded at 1300 hr on 23 June (Fig. 1), cutting APC Cores 174A-1071A-1H through 7H from 0 to 36.3 mbsf (76.4% recovery; Table 1). All seven cores were partial strokes with the bit advanced by recovery. Core 6H recovered liquefied sand, which was assumed to be mostly suck-in. Core 7H had a shattered liner that had to be heated and pumped out, which required 2 hr.

XCB Cores 174A-1071A-8X through 10X were cut from 36.3 to 51.9 mbsf (7.0% recovery). The coring parameters were varied in unsuccessful efforts to optimize recovery. A Davis-Villinger Temperature Probe (DVTP) was run after Core 9X at 49.3 mbsf. At 2330 hr on 23 June, a ground fault was detected in the top drive. Further investigation indicated that the motor field windings had burned out. Coring was terminated, and the bit was pulled to complete repairs, clearing the rotary at 0355 hr, ending Hole 1071A. Replacement of the top drive motor with a spare carried on board required 25 hr.

Hole 1071B

During the top-drive repairs, the ship was moved 10 m to the northeast (35° course along seismic Profile 806 in the direction of proposed site MAT-8B2) (Fig. 1). The same APC/XCB BHA used at Hole 1071A was rerun with a 10-1/8-in polycrystalline diamond compact (PDC) drill bit. The PDC bit was set at 93 mbrf, and an APC core was attempted at 0817 hr on 25 June; however, the BHA apparently moved and broke off the APC shoe and core barrel with no recovery. ASK excursion warnings, set at 4% (yellow light) and 8% (red light) of total water depth, shut down operations for 2.75 hr on 25 June.

Hole 1071B was spudded at 0945 hr on 25 June with an XCB core barrel (Table 1). Although the beacons were now reasonably stable, the ASK system was still experiencing numerous excursions. Therefore, the decision was made to drill ahead to bury the drill collars,
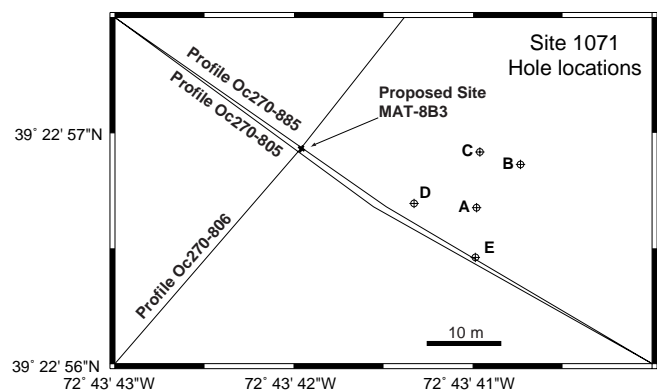

Figure 1. Location map of Holes 1071A–1071E with respect to originally proposed site location MAT-8B3 and site survey seismic data (Cruise Oc270 Profiles 806 and 885; see "Seismic Stratigraphy" section, this chapter).

Table 1. Site 1071 coring summary.

Core	Date (1997)	Time (EST)	Depth (mbsf)	Length cored (m)	Length recovered (m)	Recovery (%)
174A-1071A-						
1H	23 June	1320	0.0-5.1	5.1	5.16	101.2
2H	23 June	1420	5.1-7.9	2.8	2.77	98.9
3H	23 June	1510	7.9-12.0	4.1	4.14	101.0
4H	23 June	1550	12.0-16.2	4.2	4.20	100.0
5H	23 June	1630	16.2-25.7	9.5	9.67	101.8
6H	23 June	1710	25.7-26.8	1.1	1.11	100.9
7H	23 June	1740	26.8-36.3	9.5	0.70	7.4
8X	23 June	2000	36.3-39.9	3.6	0.18	5.0
9X	23 June	2120	39.9-49.3	9.4	0.05	0.5
10X	23 June	2350	49.3-51.9	2.6	0.87	33.5
Coring totals:				51.9	28.85	55.6
174A-1071B-						
1W	25 June	1330	0.0-39.8	NA	NA	NA
2X	25 June	1450	39.8-49.2	9.4	2.10	22.3
3X	25 June	1630	49.2-52.9	3.7	0.59	15.9
4X	25 June	2035	52.9-58.4	5.5	0.61	11.1
5X	25 June	2105	58.4-67.8	9.4	7.33	78.0
6X	25 June	2135	67.8-77.4	9.6	0.37	3.9
Coring totals:				37.6	11.00	29.3
174A-1071C-						
1W	27 June	0250	0.0-58.4	NA	NA	NA
2X	27 June	0410	58.4-67.8	9.4	6.07	64.6
3X	27 June	0510	67.8-77.4	9.6	0.70	7.3
4X	27 June	0815	77.4-86.8	9.4	0.00	0.0
5X	27 June	0900	86.8-96.2	9.4	0.00	0.0
6X	27 June	1005	96.2-105.6	9.4	1.01	10.7
7X	27 June	1105	105.6-114.9	9.3	0.41	4.4
8X	27 June	1215	114.9-124.5	9.6	1.59	16.6
9X	27 June	1340	124.5-134.0	9.5	4.70	49.5
10X	27 June	1550	134.0-143.5	9.5	0.41	4.3
11X	27 June	1630	143.5-148.5	5.0	6.00	120.0
12X	27 June	1710	148.5-152.9	4.4	5.18	117.7
13X	27 June	1750	152.9-157.9	5.0	4.53	90.6
14X	27 June	1820	157.9-162.4	4.5	5.25	116.7
15X	27 June	1900	162.4-171.8	9.4	9.91	105.4
16X	27 June	1940	171.8-181.3	9.5	3.61	38.0
17X	27 June	2005	181.3-190.8	9.5	0.00	0.0
18X	27 June	2035	190.8-200.1	9.3	0.21	2.3
19X	27 June	2130	200.1-209.5	9.4	1.26	13.4
20X	27 June	2230	209.5-219.0	9.5	5.47	57.6
21X	28 June	0220	219.0-228.4	9.4	0.00	0.0
22X	28 June	0315	228.4-237.7	9.3	2.13	22.9
23X	28 June	0410	237.7-247.0	9.3	2.11	22.7
24X	28 June	0520	247.0-251.6	4.6	1.00	21.7
25X	28 June	1935	251.6-256.4	4.8	5.66	117.9
26X	28 June	2030	256.4-256.9	0.5	0.34	68.0
27X	28 June		256.9-257.4	0.5	0.00	0.0
Coring totals:				199.0	67.55	33.9
174A-1071D-						
1R	7 July	2210	0.0-9.1	9.1	0.70	7.7
2R	7 July	2300	9.1-18.8	9.7	0.10	1.0

Core	Date (1997)	Time (EST)	Depth (mbsf)	Length cored (m)	Length recovered (m)	Recovery (%)
3R	7 July	2325	18.8-28.3	9.5	0.20	2.1
4R	8 July	0050	28.3-38	9.7	0.12	1.2
5R	8 July	0150	38.0-47.7	9.7	0.35	3.6
6R	8 July	0240	47.7-57.4	9.7	1.13	11.6
7R	8 July	0320	57.4-62.4	5.0	0.44	8.8
8R	8 July	0350	62.4-66.9	4.5	0.94	20.9
9R	8 July	0425	66.9-71.9	5.0	0.00	0.0
10R	8 July	0507	71.9-76.4	4.5	0.00	0.0
11R	8 July	0545	76.4-81.4	5.0	0.00	0.0
12R	8 July	0615	81.4-85.7	4.3	0.00	0.0
Coring totals:				85.7	3.98	4.6
174A-1071E-						
******Drilled from 0 to 259.8 mbsf******						
Total:				259.8		
174A-1071F-						
******Drilled from 0 to 252.0 mbsf******						
1R	11 July	30	252.0-261.4	9.4	3.12	33.2
2R	11 July	115	261.4-270.7	9.3	0.50	5.4
3R	11 July	210	270.7-280.1	9.4	0.00	0.0
******Drilled from 280.1 to 284.9 mbsf******						
4R	11 July	438	284.9-291.9	7.0	0.00	0.0
******Drilled from 291.9 to 310.8 mbsf******						
5R	11 July	645	310.8-320.2	9.4	0.00	0.0
6R	11 July	730	320.2-329.6	9.4	1.33	14.1
7R	11 July	815	329.6-339.0	9.4	1.71	18.2
8R	11 July	900	339.0-348.5	9.5	1.04	10.9
9R	11 July	943	348.5-357.9	9.4	3.02	32.1
10R	11 July	1030	357.9-367.4	9.5	5.30	55.8
11R	11 July	1115	367.4-376.9	9.5	3.37	35.5
12R	11 July	1200	376.9-386.3	9.4	0.03	0.3
13R	11 July	1240	386.3-395.8	9.5	0.10	1.1
14R	11 July	1315	395.8-405.2	9.4	0.10	1.1
15R	11 July	1355	405.2-414.8	9.6	0.34	3.5
16R	11 July	1520	414.8-424.2	9.4	0.11	1.2
Coring totals:				148.5	20.07	13.5%
Drilled:				275.7		
Total:				424.2		
174A-1071G-						
******Drilled from 0.0 to 95.1 mbsf******						
Total:				95.1		

Notes: An expanded version of this coring summary table that includes lengths and depths of sections, location of whole-round samples, and comments on sample disturbance is included on the CD-ROM in the back pocket of this volume. EST = U.S. Eastern Standard Time. NA = not applicable.

putting more flexible drill pipe in the water column below the ship. Therefore, Hole 1071B was washed from 0 to 39.8 mbsf, and a 1.31-m wash core (174A-1071B-1W) was recovered. Cores 174A-1071B-2X through 3X were cut from 39.8 to 52.9 mbsf, recovering 2.69 m (20.5%).

At 1515 hr on 25 June, the newly installed top drive began smoking. A jammed or dragging air brake was suspected; therefore, the bit was pulled out to the seafloor at 1610 hr on 25 June. The brake recess was cleaned out, and the top drive was returned to service after 3.25 hr.

The ship position had not changed, and the bit voluntarily reentered Hole 1071B at 1845 hr. The bit was run to bottom of the hole with very light reaming. A sepiolite mud sweep was conducted at 53 mbsf, and XCB coring resumed. Cores 174A-1071B-4X through 6X were recovered from 52.9 to 77.4 mbsf with 33.9% recovery. At 77.3 mbsf at 2200 hr on 25 June, the pipe became stuck when the bit was run to bottom in preparation for coring. The pipe was being worked up to 100,000 lb overpull and 800 A torque when the top drive failed. Unable to rotate or circulate, the pipe was pulled to 150,000 lb without success. Preparations were made to sever the pipe; however, a final effort to fracture the formation, with 3000 psi pump pressure at 500 gpm and 30 bbl of sepiolite mud, freed the pipe at 2245 hr. The

bit was pulled up to the ship for top-drive repairs, clearing the rotary at 0115 hr on 26 June. Parts were scavenged from the original (now backup) top drive to replace a pinion gear that had slipped down off the draft shaft; repairs were completed at 1845 on 26 June after 17.5 hr downtime.

Hole 1071C

During the third top-drive repair, the ship was moved 6.7 m at ~275° from Hole 1071B to Hole 1071C (Fig. 1) to permit time for ASK stability evaluation. Utilizing the same BHA and bit with an XCB core barrel, Hole 1071C was spudded at 2035 hr on 26 June (Table 1). To get the BHA buried as quickly as possible, the hole was washed to 58.4 mbsf.

XCB coring was initiated, but the drill pipe became stuck after Core 174A-1071C-4X (86.8 mbsf), stalling the rotary; the pipe would not move after 60,000-lb overpull. The drill pipe was freed after setting weight down on the BHA and increasing pump pressure and circulation. XCB Cores 174A-1071C-2X through 20X were cut from 58.4 to 219.0 mbsf with 43.1% recovery. A 20-bbl precautionary sepiolite mud sweep was circulated on every core to clean out loose, coarse sand.

At 2230 hr on 27 June, after Core 20X (219.0 mbsf), an ASK alert was sounded when a tidal surge caused a 30.5-m excursion. As a precaution, the pipe was set in the 500-T elevators with a maximum pull of 10,000 lb. A wiper trip was made to 94 mbrf to examine the pipe located at the seafloor, which was essentially undamaged. The pipe was run back to bottom with no fill.

XCB Cores 174A-1071C-21X through 24X were taken from 219.0 to 251.6 mbsf with 16.8% recovery. A heavy backflow of fluid and coarse sand pushed the barrel for Core 25X back out of the pipe. Fluid flow initially reached the top drive, located halfway up the derrick, and deposited ~5 cm of coarse sand and shell debris on the rig floor. No hydrocarbons had been noted in the previous core or in the water flowing out of the pipe; therefore, there did not appear to be a safety risk either to equipment or to personnel. Despite the heavy backflow, the drill string seemed to remain free. A precautionary 20-bbl sepiolite mud sweep was circulated in an effort to remove any loose sand bridges, but it had no effect on the flow of fluid. The initial conclusion was that the lockable float valve (LFV) had failed in the XCB assembly and that a charged aquifer had been penetrated, allowing fluid to vent up the pipe. However, subsequent chemical analyses of both the fluid and surface seawater indicated that the flowing water was in fact surface seawater pumped down as drilling fluid (see "Inorganic Geochemistry" section, this chapter, for additional details).

The bit was pulled to 74.8 mbsf, the core barrel was retrieved, and the VIT was deployed to view the hole at the seafloor. An 8-m-wide, round crater with billowing water and sand was observed, but no strong flow was evident. Two 4-m-long pock marks indenting the side of the crater indicated where the drill pipe had been forced into the crater rim during previous ASK excursions. The BHA was then pulled to the ship, and the LFV was replaced with a flapper valve (FV), in which the flapper is normally closed (by a spring) and does not lock open. Hole 1071C was reentered easily and cleaned out to 251.6 mbsf through a few minor, soft bridges.

XCB Cores 174A-1071C-25X through 27X were recovered from 251.6 to 257.4 mbsf. A 0.3-m-thick, well-indurated sandstone was recovered in Core 26X; the core barrel was pulled early because of the slow rate of penetration (ROP; 0.4 m/hr). After cutting Core 27X through an estimated 0.25 m of the sandstone and 2–3 m of very soft, presumably sandy, material, the pipe became stuck at 257.4 mbsf at 2115 hr on 28 June. The pipe was moved up 2 m with overpulls up to 220,000 lb in an unsuccessful attempt to free the drill string. Wireline logging through the pipe was considered, but logging could not be attempted because pipe connection positions above the rig floor were unsuitable for breaking the string to insert logging tools. Efforts to sever the pipe were then delayed for 2.25 hr because eddy currents set off ASK system alerts. At 0225 hr on 29 June, the pipe was severed at 130.2 mbsf, between the top two joints of 5-in drill pipe. The pipe cleared the rig floor at 0500, 7.75 hr after getting stuck, ending Hole 1071C. Core 27X was not retrieved.

Transit Back to Site 1071

The ship was moved in dynamic positioning (DP) mode 1.9 nmi west from Site 1072, returning to Hole 1071C. A beacon (18.0 kHz) was deployed through the moonpool at 1910 hr on 7 July, followed by a second beacon (15.0 kHz) at 1940 hr.

Hole 1071D

In previous holes, Site 1071 was cored only with the APC/XCB system and was plagued by unstable hole problems. However, the upper 350 mbsf at Site 1072 had been successfully cored with the rotary core barrel (RCB) coring system; therefore, we returned to Site 1071 in an attempt to RCB core down through the upper 250 mbsf and further deepen the hole. The seafloor was tagged at 88 mbsl (99.4 mbrf), and Hole 1071D was spudded at 2100 hr on 7 July (Fig. 1; Table 1). RCB Cores 174A-1072D-1R through 12R were cut from 0 to 85.7 mbsf; however, recovery was negligible despite taking half-cores. In

an effort to improve recovery, the pump rate was reduced by 50%, but the pipe became stuck while going back to bottom with the next core barrel. The pipe was worked with up to 150,000 lb overpull and 1100 A torque (maximum allowed) without success; the aft counterbalance sling on the top drive was broken in the process. The core barrel was removed through the top of the blocks, and the pipe was worked in tight hole ~6 m higher. The pipe came free while circulating at 1000 gpm and slacking off weight (until the pipe stood up in the elevators) with 1100 A torque. The bit was pulled through the rotary at 1240 hr on 8 July.

Hole 1071E

A last attempt was made to drill down through the unstable sands at Site 1071 to log and core the remaining section quickly before hole instability again became a problem. The ship was moved 12 m from Hole 1071D at ~125° past Hole 1071A (Fig. 1). The seafloor was tagged at 87.6 mbsl (99.0 mbrf), and Hole 1071E was spudded at 1510 hr on 8 July, drilling to 259.8 mbsf using 20-bbl mud sweeps every 19 m (Table 1). A short trip was made to 45 mbsf and found 15.6 m of soft fill. The hole was displaced with sepiolite mud, and the drilling BHA was pulled to change to a logging BHA rather than drop the bit in the hole. The bit change took 4 hr, and a VIT-TV survey of the seafloor showed a 3-m-diameter crater with the beacon container from Hole 1071A in view and still upright. The logging bit was positioned at 45.8 mbsf after reaming fill at 39 m. The Dual Induction (DIT-E)/Long-Spaced Sonic (LSS)/Natural Gamma-ray Tool (NGT) tool string was unable to pass 60 mbsf (15 m below the bit). The logging bit was washed to 74 mbsf, and another attempt was made to log. The logging tool only got 7 m out of the pipe with the pipe standing up in the elevators, indicating that it was stuck. In addition, heavy backflow of seawater and fine sand was observed, suggesting that the hole was collapsing. The pipe was freed and pulled out, clearing the rotary at 2015 hr on 9 July, ending Hole 1071E.

Hole 1071F

Approval was received to move to two alternate sites in the MAT-8B hazards survey grid, which were projected to have higher silt and clay content in the deeper section than at site MAT-8B3. Approval also was given to keep the same Site 1071 designation and drill through the unstable upper section to 250 mbsf. The ship was moved in DP mode ~1 km east to newly designated site MAT-8B4 (Fig. 2). A bottom survey was conducted over a flat, featureless seafloor.

The seafloor was tagged at 90 mbsl (101.5 mbrf), and Hole 1071F was spudded at 0027 hr on 10 July, drilling from 0 to 230.0 mbsf, where the pipe became stuck (Table 1). The drill pipe was worked free by setting weight down on the BHA, and using high torque (900
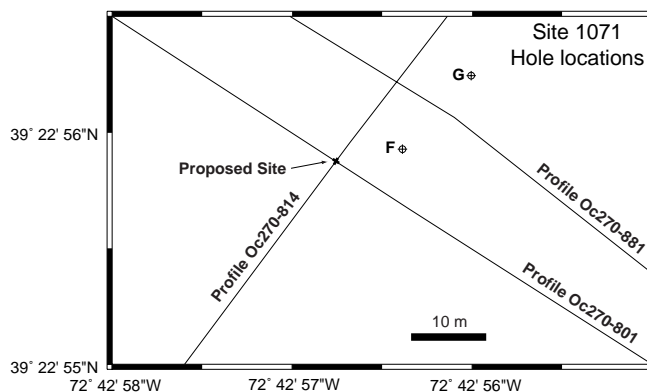
Figure 2. Location map of Holes 1071F and 1071G with respect to proposed site MAT-8B4 and site survey seismic data (Cruise Oc270 Profiles 801 and 814; see "Seismic Stratigraphy" section, this chapter).

Table 2. Lithostratigraphic summary of Holes 1071A, 1071B, 1071C, and 1071F.

Subunit	Series	Core, section, interval (mbsf)	Lithology
IA	Holocene(?)-upper Pleistocene	174A-1071A-1H-1, 0 cm, to 5H-1, 113 cm (0-17.3)	Silty clays and clayey silts interbedded with sandy silts and sand.
IB	upper Pleistocene	5H-1, 113 cm, to 10X-CC, 29 cm (17.3-52); 174A-1071B-2X-1, 0 cm, to 5X-3, 1 cm (39.8-61.4); 174A-1071C-2X-1, 0 cm, to 2X-2, 100 cm (58.4-60.9)	Silty clay and clay interbedded with sand. Sands generally exhibit sharp bases and gradational tops.
IC	Pleistocene-lower Pliocene(?)	174A-1071B-5X-3, 1 cm, to 6X-CC, 37 cm (61.4-77.4); 174A-1071C-2X-2, 100 cm, to 10X-CC, 41 cm (60.9-134.4)	Sandy clay, sandy silt, and sand intervals separated by intervals of no recovery, which suggests that Subunit IC is dominated by sand. Thinly bedded sands and sand lenses.
IIA	lower Pleistocene-upper Miocene	174A-1071C-10X-CC, 41 cm, to 16X-CC, 26 cm (134.4-175.4)	Silty clay with scattered quartz granules, rare shell and wood fragments, and scattered nodules of siderite and pyrite. Interbeds of sandy silt.
IIB	upper Miocene	16X-CC, 26 cm, to 20X-CC, 37 cm (175.4-214.97)	Silty clay and sand. Poor core recovery suggests that Subunit IIB is composed predominantly of sand. Scattered granules, pebbles, and shell fragments present at base.
IIC	upper Miocene	20X-CC, 37 cm, to 26X-1, 34 cm, and 174A-1071F-1R-1, 0 cm, to 2R-1, 8 cm (214.97-261.48)	Interbeds of silty clay and silty sand separated by intervals of no core recovery (which suggests that sand is present between beds). A cemented interval of glauconitic pebbly sandstone at base.
IID	upper Miocene	174A-1071F-2R-1, 8 cm, to 2R-CC, 5 cm (261.48-261.90)	Silty clay, laminated, with organic detritus and localized granules and pebbles.
IIIA	upper-middle Miocene	2R-CC, 5 cm, to 11R-CC, 8 cm (261.90-370.77)	Micaceous, muddy sand and sandy mud containing graded and laminated beds as well as carbonate beds and nodules. Poor recovery suggests that sand is dominant.
IIIB	upper-middle Miocene	11R-CC, 8 cm, to 16R-CC, 15 cm (370.77-414.91)	Micaceous silty clay with rare siderite beds. Poor recovery suggests that sand is dominant.

A) and high circulation rates (700 gpm at 175 psi). The hole was reamed to 53.5 mbsf with the top drive, and 12 m of fill was cleaned out. Drilling continued from 230.0 to 233.5 mbsf, where the pipe became stuck again. The pipe was freed as before using high circulation rates and torques. Shortly thereafter, ASK system alarms shut down operations for 2.24 hr, after which the hole was then drilled ahead from 233.5 to 252.0 mbsf. RCB Cores 174A-1071F-1R through 3R were recovered from 252.0 to 280.1 mbsf; however, torque and drag were high through this presumed sandy interval. The pipe was conditioned by reaming out and back in with the top drive, and then drilling from 280.1 to 284.9 mbsf. Coring resumed with Core 174A-1071F-4R (284.9–291.9 mbsf), but with no recovery. The interval from 291.9 to 310.8 mbsf was drilled with no coring, after which coring resumed with Cores 174A-1071F-5R through 16R from 310.8 to 424.2 mbsf. Low recovery in Cores 12R through 16R suggested another interval of unconsolidated sands, so we judged it prudent to cease coring operations and attempt to obtain logs to total depth.

A wiper trip was made to 43 mbrf, experiencing no drag or overpull with 48 m of fill. The bit was released in the hole, the hole was displaced with sepiolite mud, and the pipe was pulled out with the top drive to 53 mbsf for logging. During the first logging run, the LSS/DIT-E logging tool stopped 21 m below the end of pipe. The open-ended pipe was washed down to 87.7 mbsf; however, the hole appeared to be closing in rapidly. Therefore, logging was terminated and the pipe cleared the rotary at 0840 hr on 12 July, ending Hole 1071F.

Hole 1071G

A final attempt was made to obtain logs using the LWD tools. The ship was moved 15 m at ~035° from Hole 1071F (Fig. 2). The seafloor was tagged at 90 mbsl (101.5 mbrf), and Hole 1071G was spudded at 1247 hr on 12 July (Table 1). The hole was drilled with the LWD assembly to 95.1 mbsf in 4.5 hr; however, the pipe became stuck after making the next connection. Attempts to free the pipe with increased circulation rates, mud sweeps, and use of the jars were unsuccessful; therefore, it was assumed that the top of the hole had collapsed. Consequently, it was necessary to run the LWD Inductive Coupling (LINC) tool to retrieve the radioactive sources and download the logging data. After successfully retrieving sources and data, and while preparations were being made to sever the pipe, the pipe came free and was retrieved. The bit cleared the rotary at 2315 hr, ending Hole 1071G and operations at Site 1071.

LITHOSTRATIGRAPHY

Site 1071 was positioned primarily to determine facies changes across the upper middle Miocene m1(s) sequence boundary where it truncates the top of a well-defined set of clinoforms near their seaward edge or rollover/breakpoint as observed on seismic-reflection profiles. The site was also designed to sample and date sequence boundaries and discontinuity surfaces that are both younger and older than m1(s) (see "Introduction" chapter, this volume, and "Background and Objectives" section, this chapter). Drilling was terminated at a maximum depth of ~415 mbsf (Hole 1071F), the approximate position of m1(s); only a partial record of Holocene(?) through middle Miocene sedimentation was obtained.

Subdivision of the cored intervals into lithostratigraphic units was complicated by several factors, the most important of which were poor sediment recovery (Table 2; Figs. 3, 4) and the lack of complementary logs from Site 1071 holes. The recovered intervals are predominantly muds with subordinate amounts of sand. Unrecovered intervals (Fig. 3) tend to be sandy. General support for this interpretation comes from comparison with the downhole gamma-ray wireline log for the COST-B2 well (Scholle, 1977), which was drilled ~950 m from Site 1071 (Fig. 3; see "Downhole Logging" section, this chapter). However, as a caveat, it should be stressed that the LWD log completed to 88 mbsf in Hole 1071G indicates that significant intervals of unrecovered upper Pleistocene section are argillaceous (Fig. 3; see "Downhole Logging" section, this chapter). An additional complicating factor was the limited variability in general lithology throughout the recovered parts of the succession. Three lithostratigraphic units are defined. The boundaries between these units are delineated primarily on the basis of abrupt changes in the vertical arrangement of lithofacies within the succession. Units I, II, and III are subdivided into three (IA–IC), four (IIA–IID), and two (IIIA, IIIB) subunits, respectively. Subunits are delineated on the basis of discontinuities inferred from sedimentologic, multichannel seismic (MCS), or other data (see "Seismic Stratigraphy" section, this chapter) or, in intervals of poor recovery, at arbitrary horizons between sediments of different lithology.

Unit I

Intervals: 174A-1071A-1H-1, 0 cm, to 10X-CC, 29 cm; 174A-1071B-2X-1, 0 cm, to 6X-CC, 37 cm; and 174A-1071C-2X-1, 0 cm, to 10X-CC, 41 cm
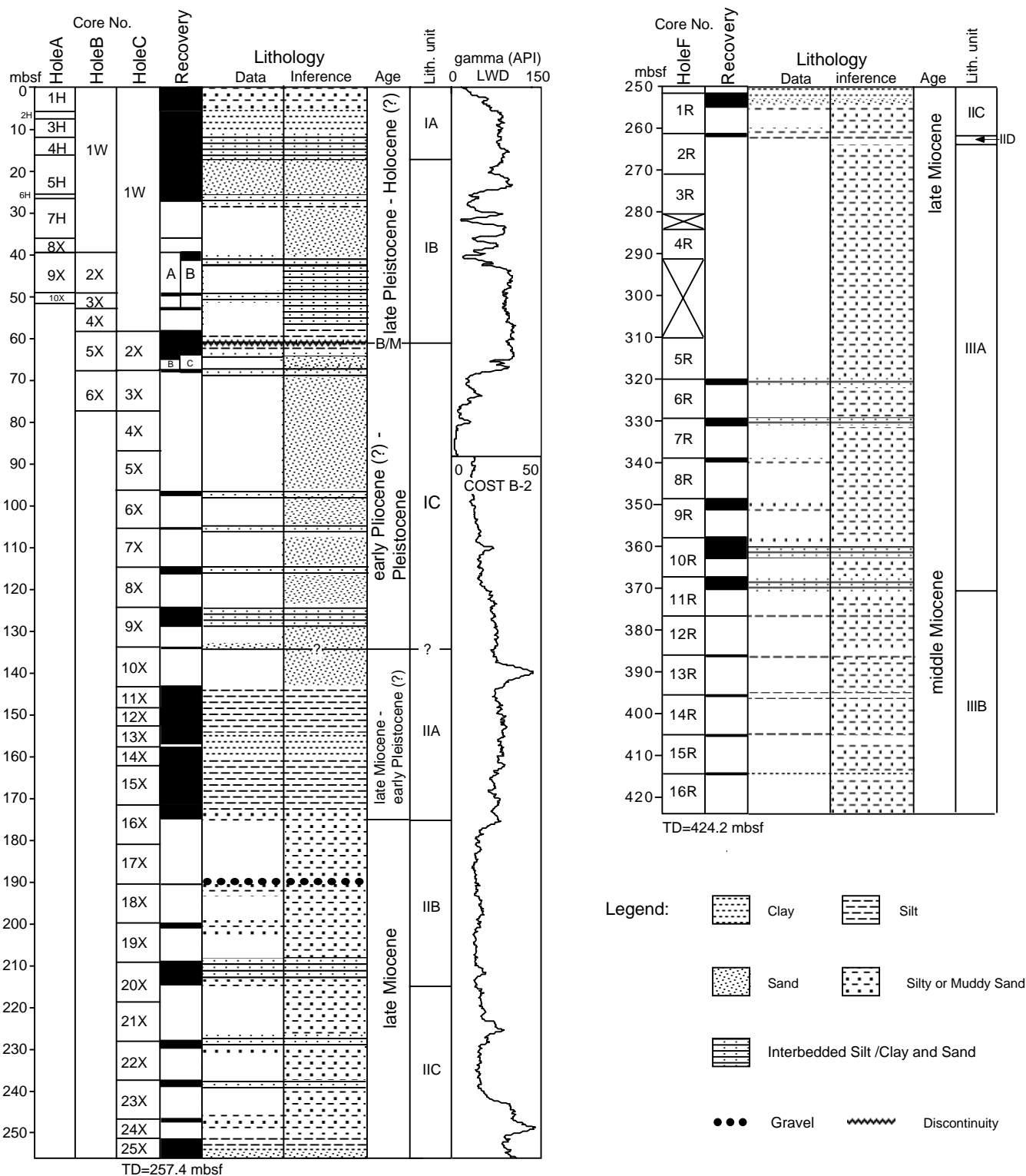
Figure 3. Generalized summary for Holes 1071A–1071C and 1071F, showing core recovery, lithology, age, and lithologic subunits. The lithology column shows the lithology based on recovered cores (data) and lithology for intervals of nonrecovery (inference) based on the gamma-ray signature from the uppermost ~88 mbsf of Hole 1071G and a wireline log from the nearby COST-B2 well for depths below 90 mbsf (see "Downhole Logging" section, this chapter). Because the wireline log from the COST-B2 well (water depth = 86.6 m) is appended to the log from Hole 1071G (water depth = 90 m), the COST-B2 gamma-ray values are shifted 3.4 m deeper than their true depths. B/M = Brunhes/Matuyama boundary.

Depth: 0–134.4 mbsf
Age: Holocene(?), Pleistocene possibly through early Pliocene(?)

Subunit IA

Interval: 174A-1071A-1H-1, 0 cm, to 5H-1, 113 cm
Depth: 0–17.3 mbsf

Excellent recovery (~97%) throughout Subunit IA allowed recognition of a complete coarsening-upward succession (Figs. 3, 4). The uppermost 5.2 m of this subunit (interval 174A-1071A-1H-1, 0 cm, to 1H-CC, 14 cm) is characterized by olive gray to dark olive gray, quartzose, micaceous, fine- to medium-grained sand containing localized concentrations of fragmented mollusk shells. The interval from 5.2 to 7.8 mbsf (interval 174A-1071A-2H-1, 0 cm, to 2H-CC, 22 cm) is locally stained by hydrotroilite and dominated by dark to very dark gray clayey silt intercalated with silty clay and sandy silt. The underlying 4 m of sediment (interval 174A-1071A-3H-1, 0 cm, to 3H-CC, 12 cm) is characterized by dark gray silty clay with rare thin beds of clayey silt. From 12 to 16.2 mbsf (interval 174A-1071A-4H-1, 0 cm, to 4H-CC, 25 cm), silty clay remains dominant, but thin interbeds of silt and fine sand, some of which exhibit irregular bases and normal grading, are more abundant. The lowermost 1.2 m of this subunit (16.2–17.4 mbsf; interval 174A-1071A-5H-1, 0 cm, to 5H-1, 112 cm) is characterized by interbeds of medium thickness composed of dark gray clay and fine sands with normal grading and erosional bases. Beds in Subunit IA generally lack internal stratification. Sediment homogeneity is attributed to extensive bioturbation, although distinct, unidentified burrows generally are observed only where silt- or sand-filled burrows crosscut silty clays.

Subunit IB

Intervals: 174A-1071A-5H-1, 113 cm, to 10X-CC, 29; 174A-1071B-2X-1, 0 cm, to 5X-3, 1 cm; and 174A-1071C-2X-1, 0 cm, to 2X-2, 100 cm
Depth: 17.3–61.4 mbsf (in Hole 1071B)

Subunit IB is an interval of relatively poor recovery (28%; Figs. 3, 4). The upper 10.2 m of this subunit (17.3–27.5 mbsf; interval 174A-1071A-5H-2, 112 cm, to 7H-7, 70 cm) is dominated by dark gray, predominantly fine-grained, quartz sand containing abundant mica and glauconite, and rare mud clasts. Thick to thin interbeds of dark brownish gray to dark gray clay and silty clay are present in the upper and lower parts of this sand (intervals 174A-1071A-5H-1, 113 cm, to 5H-2, 120 cm; and 174A-1071A-6H-1, 29 cm, to 7H-1, 70 cm). Sands in these interbedded intervals generally exhibit sharp bases and gradational tops (Fig. 5). Recovery from the subjacent 12.3 m of the hole (27.5–39.8 mbsf; interval 174A-1071A-7H-1, 70 cm, to 174A-1071B-2X-1, 0 cm) was extremely poor and only a very thin (~20 cm thick) interval of shelly, grayish brown to olive greenish gray sand was recovered from a depth of 36.3–36.5 mbsf (interval 174A-1071A-8X-CC, 0–14 cm). Presumably, similar sands compose the bulk of the unrecovered sediments. From 39.8 to 61.4 mbsf (interval 174A-1071A-8X-CC, 0–14 cm, to 10X-CC, 29 cm; and 174A-1071B-2X-1, 0 cm, to 5X-3, 1 cm), four intervals of sediment were recovered. The uppermost interval (39.8–41.7 mbsf; interval 174A-1071B-2X-1, 0 cm, to 3X-CC, 15 cm) is characterized by dark gray to dark greenish gray clay interbedded with thin, quartzose, micaceous, and locally glauconitic, fossiliferous, pyritiferous, and/or pebbly fine sands. The clays are homogeneous as a result of bioturbation and are locally crosscut by sand-filled burrows. The two underlying recovered intervals (intervals 174A-1071A-10X-1, 0 cm, to 10X-CC, 29 cm, and 174A-1071B-3X-1, 0 cm, to 3X-CC, 15 cm; and interval 174A-1071B-4X-1, 0–53 cm) are dominated by bioturbated, dark gray to very dark gray, micaceous silty clay and clay with dispersed small pebbles, granules, and shell fragments. The lowermost interval of Subunit IB (58.4–61.4 mbsf; interval 174A-1071B-5X-1, 0 cm, to 5X-3, 1 cm; and 174A-1071C-2X-1, 0 cm, to 2X-2, 100 cm) is also dominated by bioturbated silty clays as above, but its base is characterized by thin interbeds of brownish gray sand. Although most sand

interbeds are fine-grained, the basal sand is medium-grained and glauconitic and exhibits a very sharp erosional base (Fig. 6). The latter surface defines the boundary between Subunits IB and IC and is close to seismic discontinuity pp3(s) (Fig. 4B; see "Seismic Stratigraphy" and "Summary and Conclusions" sections, this chapter).

Subunit IC

Intervals: 174A-1071B-5X-3, 1 cm, to 6X-CC, 37 cm; and 174A-1071C-2X-2, 100 cm, to 10X-CC, 41 cm
Depth: 61.4 (in Hole 1071B) to 134.4 mbsf

Subunit IC is characterized by extremely poor recovery (~13%). As in Subunits IA and IB, unrecovered intervals are inferred from the COST-B2 wireline logs to be dominated by sands (Figs. 3, 4; see "Downhole Logging" section, this chapter). The top part of Subunit IC (intervals 174A-1071B-5X-3, 1 cm, to 5X-CC, 26 cm; and 174A-1071C-2X-2, 100 cm, to 2X-CC, 34 cm) is characterized by homogeneous, olive gray, pyritic silty clay, which, in the lower 3 cm, contains thin interbeds of fine- to medium-grained sand and scattered shell fragments. Only four short (<1.5 m), isolated cores were recovered from interval 174A-1071C-2X-CC, 34 cm, to 9X-1, 0 cm. The upper three of these (Cores 174A-1071C-3X-1, 6X-1, and 7X) are predominantly dark gray or greenish gray sandy clays with thin, partly bioturbated interbeds of micaceous, glauconitic, fine-grained quartzose sands. The fourth core (Core 174A-1071C-8X-1) consists, from top to base, of interbedded dark olive gray clayey silts, silty clays, silty sands, and fine sands. Stratification is partly disrupted by bioturbation and, in the upper part, distorted by slumping (Fig. 7). The 4.7-m-thick interval recovered from 124.5 to 129.5 mbsf (Core 174A-1071C-9X) is characterized by, in descending order, dark grayish brown to grayish brown, bioturbated sandy silt with localized thin beds and lenses of fine sand; interbedded bioturbated, olive gray to grayish olive fine sand and silty clay; and interbedded heavily bioturbated sandy silt and normally graded sand. All of these contain nodules or incipient nodules. A thin section of a nodule from 127.25 mbsf (thin-section Sample 174A-1071C-9X-3, 121–125 cm) reveals quartz and glauconite sand and silt grains floating in a mica-bearing clayey silt matrix, which has been partially cemented or replaced by submicroscopic dolomite or siderite. The quartz grains in the nodule are medium to coarse, mostly well rounded to rounded, and commonly fractured. The glauconite grains are medium sized, well rounded to subrounded, and commonly immature (McCracken et al., 1996). The base of the unit at 134.4 mbsf is placed below another unrecovered interval at the bottom of a distinctive 34-cm-thick bed of dusky blue green, glauconitic, fine-grained sand (Core 174A-1071C-10X) with scattered pebbles and shell fragments. This boundary corresponds approximately with seismic discontinuity pp4(s) (see "Seismic Stratigraphy" and "Summary and Conclusions" sections, this chapter).
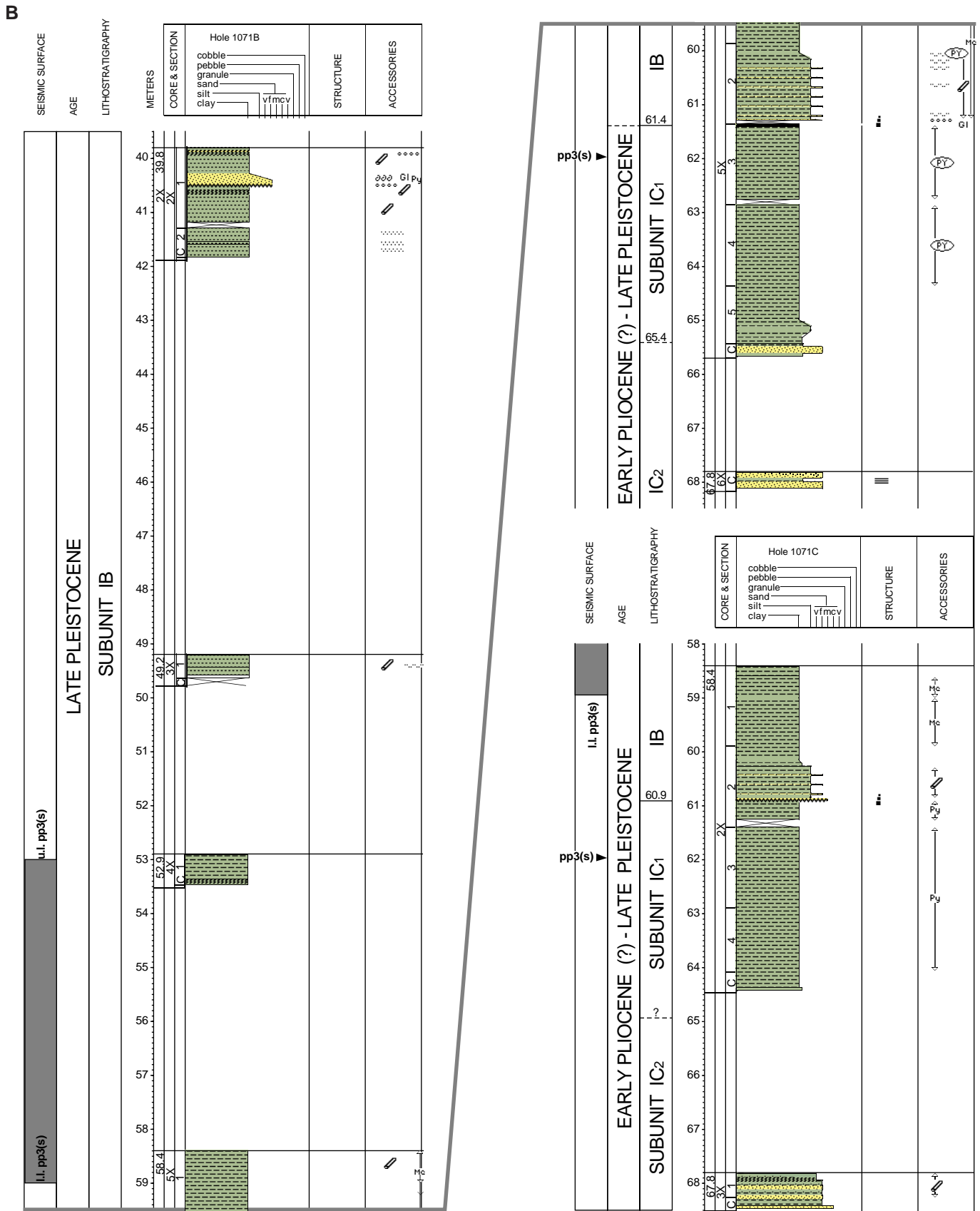
Unit II

Intervals: 174A-1071C-10X-CC, 41 cm, to 26X-CC, 35 cm; and 174A-1071F-1R-1, 0 cm, to 2R-CC, 5 cm
Depth: 134.4–261.9 mbsf
Age: early Pleistocene(?) to late Miocene

Subunit IIA

Interval: 174A-1071C-10X-CC, 41 cm, to 16X-CC, 26 cm
Depth: 134.4–175.4 mbsf

Core recovery in Subunit IIA was 83% (Figs. 3, 4). Virtually all of the core loss was from the upper 7 m of the subunit (interval 174A-1071C-10X-CC, 41 cm, to 11X-1, 0 cm), which is inferred to be sand-dominated. The bulk of the recovered sediment is composed of dark brownish gray, dark greenish gray, or dark to very dark gray silty clay, which is bioturbated (diffusely burrow mottled) and contains scattered nodules of pyrite and carbonate (siderite?), quartz pebbles, and rare shell and wood fragments. Interbeds of dark brownish

Figure 4 (see facing page). Lithostratigraphic columns showing subunits in Holes 1071A–1071C and 1071F, and their inferred ages, depths below seafloor, and relationship to seismic surfaces. Symbols for lithology, structures, and accessories are defined in the "Explanatory Notes" chapter, this volume. Dark gray bars in seismic surface column show depths calculated using the velocity curve derived from Oc270, Profile 51; solid arrowheads show depth of seismic horizons calculated from checkshot survey at Hole 1072B (see "Seismic Stratigraphy" and "Downhole Logging" sections, this chapter). Numbers in the closed "meters" column indicate drilled depths as recorded in the barrel sheets; where italicized, these numbers indicate that the drilled depths deviate from depths shown in the figure. The difference arises because, in some cases, recovery was >100%. In the figure, excess core lengths are plotted using the assumption that additional sediment was derived from the interval above that drilled (and which failed to be recovered in the previous coring run). Alternative explanations for depth deviations include core expansion and inaccurate drill depths.

A

10 meters unrecovered omitted

B

Figure 4 (continued).

C

Figure 4 (continued).

Figure 4 (continued).

Figure 4 (continued).

F

Figure 4 (continued).

Poor recovery to T.D. 424.2 mbsf
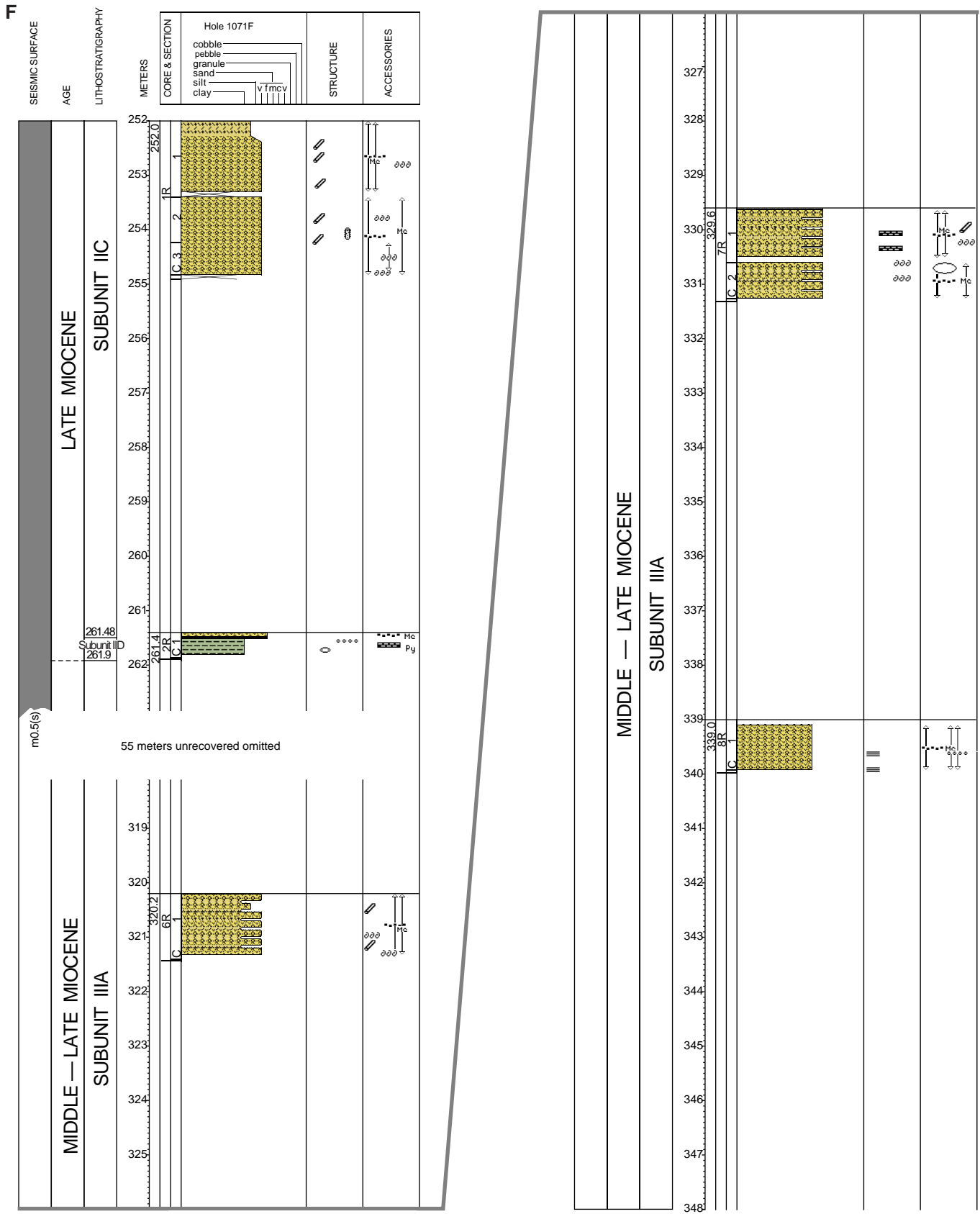
Figure 4 (continued).
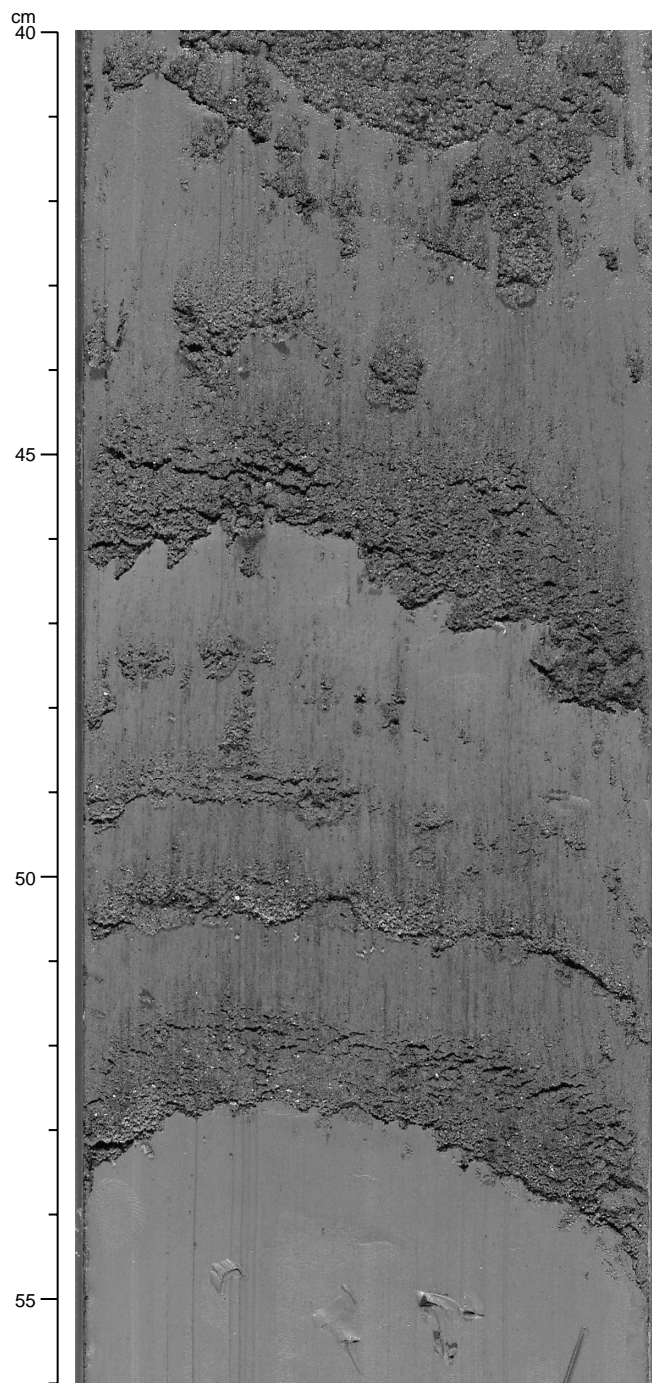
Figure 5. Sand interbeds within dark brownish clay in Subunit IB; sharp bases and gradational tops suggest storm beds (interval 174A-1071A-6H-1, 40–56 cm).

Figure 6. Medium-grained, glauconitic sand at the base of Subunit IB. Note the sharp, probably erosional, basal contact (interval 174A-1071C-2X-2, 90–106 cm).

gray silty sandy clay (interval 174A-1071C-11X-1, 52–110 cm), dark greenish gray sandy silt (interval 174A-1071C-12X-1, 5–25 cm), and dark to very dark gray silt and clayey silt with fossil fragments and incipient siderite(?) nodules are present in the silty clay. The silt and clayey silt beds are thick-bedded between 154.6 and 157.8 mbsf (interval 174A-1071C-13X-2, 100 cm, to 14X-1, 120 cm), but thin-bedded from 158.5 to 160.2 mbsf (interval 174A-1071C-14X-2, 0 cm, to 14X-3, 53 cm). The basal part of this subunit is characterized, from the top downward, by thin interbeds of bioturbated, dark gray sandy clay and micaceous, shelly, pebbly fine sand (interval 174A-

1071C-16X-1, 64 cm, to 16X-2, 17 cm); interbedded bioturbated, dark gray, pebbly muddy sand and sandy mud (interval 174A-1071C-16X-2, 17–143 cm; Fig. 8); and normally graded, olive gray, glauconitic, poorly sorted, pebbly, medium to very coarse muddy sand (interval 174A-1071C-16X-3, 0 cm, to 16X-CC, 26 cm).

Based on thin-section study (Sample 174A-1071C-16X-CC, 9–11 cm), the lowermost muddy sand is composed of matrix-supported quartz and glauconite with a clayey matrix that has been partly cemented or replaced, probably before compaction, by micritic ankerite
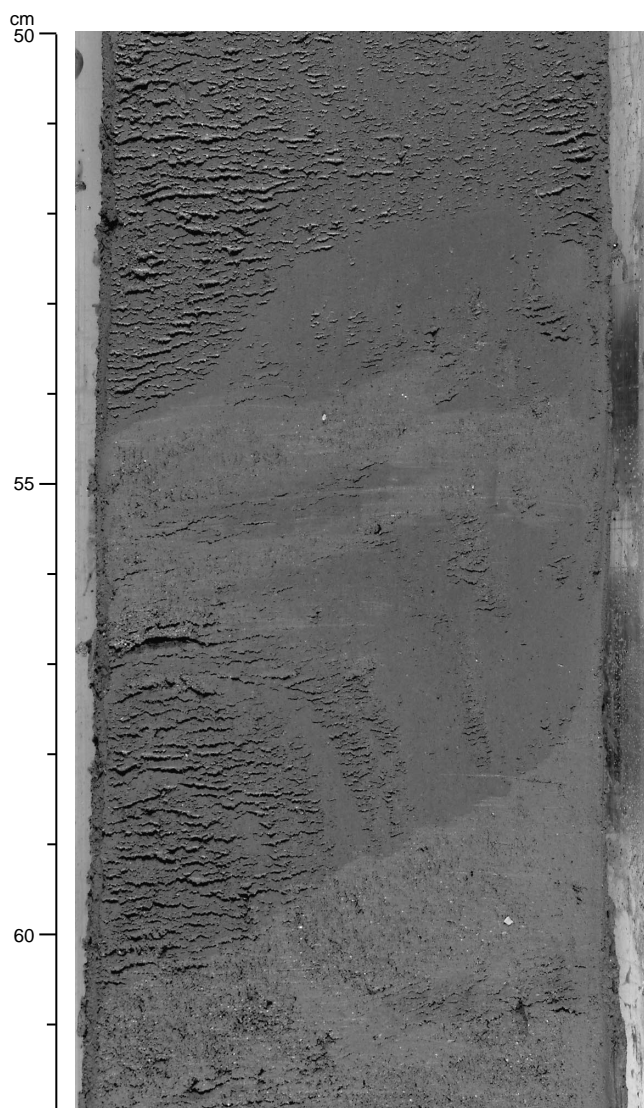
Figure 7. Distorted interbedded silty sands and silty clays in Subunit IC (interval 174A-1071C-8X-1, 50–62 cm).

Figure 8. Dark gray, pebbly muddy sand in Subunit IIA. Most pebbles are rounded to subrounded and quartzose (interval 174A-1071C-16X-2, 28–54 cm).

(Fe-dolomite). The quartz grains are rounded to subrounded, typically monocrystalline, and variably deformed (uniform to undulose extinction, Boehm lamellae, and some fracturing), with incipient corrosion and replacement by microcrystalline carbonate. The glauconite grains are typically well rounded and immature, although some exhibit shrinkage cracks and alteration rims. Feldspars (microcline and other K-feldspar), which are a minor component of the sand, are highly corroded and replaced. The base of Subunit IIA corresponds approximately with seismic surface pp5(s) (Fig. 4D; see "Seismic Stratigraphy" and "Summary and Conclusions" sections, this chapter).

Subunit IIB

Interval: 174A-1071C-16X-CC, 26 cm, to 20X-CC, 37 cm
Depth: 175.4–214.97 mbsf

Subunit IIB is characterized by very poor recovery (~18%), presumably caused by the predominance of sand (Figs. 3, 4). Between the top of the subunit at 175.4 mbsf down to 209.5 mbsf (interval 174A-1071C-16X-CC, 22 cm, to 20X-1, 0 cm), only two thin intervals of core were recovered. Interval 174A-1071C-18X-CC, 0–21 cm, contains a well-sorted, glauconitic, and quartzose gravel com-

posed of granules and fine pebbles that is underlain by dark gray, glauconitic, pebbly, fine silty sand (Fig. 9). The lower interval (interval 174A-1071C-19X-1, 0–105 cm) contains a bioturbated dark gray, glauconitic fine silty sand that grades downward to dark gray muddy sand with scattered quartzose granules and pebbles. The basal part of Subunit IIB (interval 174A-1071C-20X-1, 0 cm, to 20X-3, 150 cm) is dominated by thin interbeds of dark gray, dark olive gray, and dark greenish gray, micaceous, glauconitic, very fine to coarse silty sand and silty clay with scattered bivalve fragments and/or granules and pebbles. Stratification is moderately to highly disrupted by bioturbation, and indistinct sand-filled burrows are common in the silty clays. The lowermost bed in Subunit IIB (interval 174A-1071C-20X-4, 0 cm, to 20X-CC, 37 cm) is a completely bioturbated, dark greenish gray, glauconitic, very poorly sorted, medium-grained silty sand that contains scattered granules, pebbles, and shell fragments.

Subunit IIC

Intervals: 174A-1071C-20X-CC, 37 cm, to 26X-1, 34 cm, and 174A-1071F-1R-1, 0 cm, to 2R-1, 8 cm
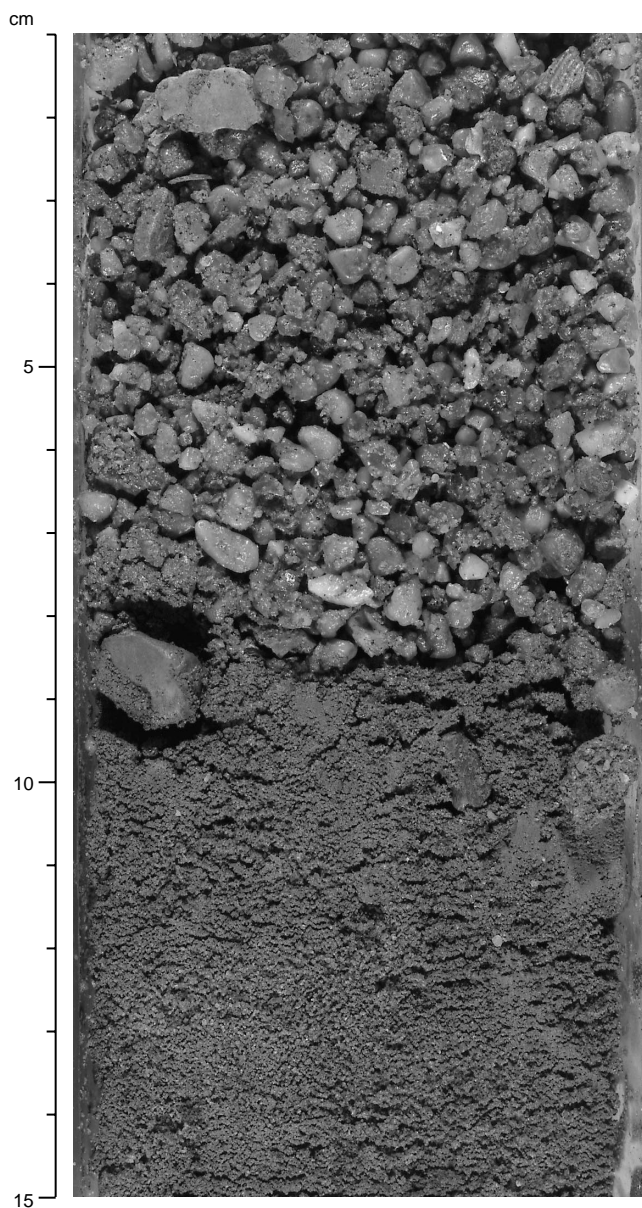
Figure 9. Well-sorted glauconitic, quartzose granule- and fine-pebble gravel overlying glauconitic, pebbly fine silty sand in Subunit IIB. Some mollusk fragments are present in the gravel (interval 174A-1071C-18X-CC, 0–15

Depth: 214.97–261.48 mbsf

Subunit IIC also is characterized by poor recovery (27%). In the interval from 215 to 250.8 mbsf (interval 174A-1071C-20X-CC, 37 cm, to 25X-1, 0 cm), only three short (<2 m) cores were recovered. The upper two, at 228.4–230.5 mbsf (Core 174A-1071C-22X) and 237.7–239.8 mbsf (Core 174A-1071C-23X), are characterized by thin interbeds of dark greenish gray, micaceous, glauconitic, quartzose, fine-to-medium silty sand and dark gray silty clay. The third core, from 247 to 248 mbsf (Core 174A-1071-24X), is dominated by silty sand similar to that of the upper two cores. Bioturbation in these intervals is intensive, although burrows are indistinct. The basal part of the subunit (interval 174A-1071C-25X-1, 0 cm, to 26X-1, 34 cm) includes, downward, dark gray, bioturbated, micaceous, sandy silt; dark gray, bioturbated clay and silty clay with rare thin beds and lenses of sandy silt; dark gray sandy clay grading downward into a bioturbated, glauconitic, clayey sand; and a well-indurated, dolo-
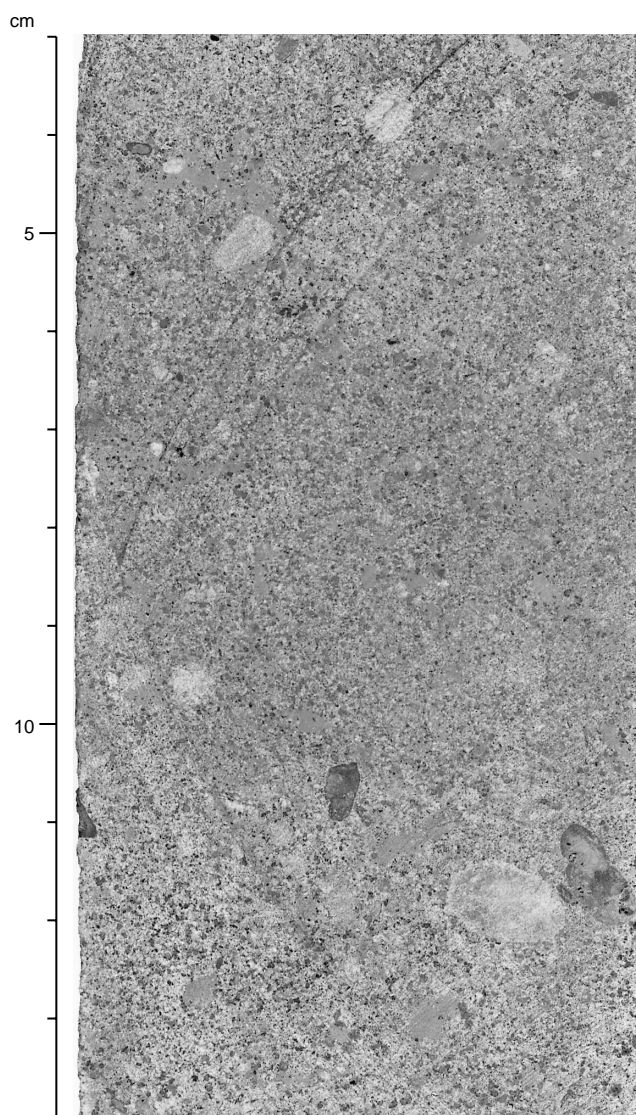
Figure 10. Well-indurated, dolomite-cemented, glauconitic pebbly sandstone in Subunit IIC (interval 174A-1071C-26X-1, 3–14 cm; see "Seismic Stratigraphy" and "Downhole Logging" sections, this chapter).

mite-cemented, dusky green and greenish gray, glauconitic, pebbly sandstone (Fig. 10). Sediments throughout this basal part typically contain pyrite and/or carbonate (siderite?) nodules and scattered wood fragments. The basal glauconitic sandstone is located close to seismic surface m0.5(s) (Fig. 4E; see "Seismic Stratigraphy" and "Summary and Conclusions" sections, this chapter).

Thin-section analysis shows that the basal indurated sandstone (Sample 174A-1071C-26X-1, 10–13 cm) is a glauconitic quartz arenite with lesser amounts of lithoclasts, feldspars, and accessory minerals. Early cement is circumgranular, isopachous dolomitic(?) micrite. This grades into a later sparry dolomite cement toward the centers of pores. The lack of apparent grain-to-grain contacts and a visually estimated, minus-cement porosity of ~35% indicate that cementation was initiated before significant compaction. The quartz grains are medium to coarse, mostly monocrystalline, and well rounded to subrounded, although the edges of some are corroded or replaced by carbonate. Quartz grains range from undulose to nonundulose and some grains may be fractured, contain fluid inclusions or Boehm lamellae, and/or exhibit abraded syntaxial overgrowths. Glauconite grains are

commonly well rounded, but exhibit a range of alteration. Some are fresh or immature grains, and some have shrinkage cracks and alteration rims, whereas others are partly to nearly completely replaced by pyrite. Feldspars (mostly microcline and other K-feldspars) are angular to subrounded and are highly corroded and partly replaced by cements.

Subunit IID

Interval: 174A-1071F-2R-1, 8 cm, to 2R-CC, 5 cm
Depth: 261.48–261.9 mbsf

Subunit IID is apparently only 0.52 m thick, although the true thickness of the lithofacies on which it is based may be considerably thicker. This subunit is characterized by very dark gray, carbonaceous silty clay containing rare, very small pebbles. Organic detritus is scattered throughout but is locally concentrated in thin, laminated beds 1–2 cm thick (Fig. 11). The lithologic character and palynomorph assemblage (see "Biostratigraphy" section, this chapter) suggest deposition in a marginal marine setting (e.g., estuary or lagoon).

Unit III

Interval: 174A-1071F-2R-CC, 5 cm, to 16R-CC, 15 cm
Depth: 261.90–414.91 mbsf
Age: late to middle Miocene

Subunit IIIA

Interval: 174A-1071F-2R-CC, 5 cm, to 11R-CC, 8 cm
Depth: 261.90–370.77 mbsf

Core recovery in Subunit IIIA was generally poor, particularly in the upper half of the subunit. No sediment was recovered in the uppermost 58.21 m (interval 174A-1071F-2R-CC, 5 cm, to 6R-1, 0 cm; 261.90–320.20 mbsf), which presumably reflects the predominance of relatively clean sands. Below this, six relatively short cores were obtained (generally < 3 m thick), separated by intervals of nonrecovery. The upper part of this succession of cores (Sections 174A-1071F-6R-1 through 9R-CC, and interval 174A-1071F-10R-1, 0–85 cm) is dominated by dark gray, slightly micaceous, very fine to fine, carbonaceous muddy sand and, subordinately, sandy mud. Organic debris is generally scattered, but is locally concentrated in laminae. Muddy sand and sandy mud generally appear to be completely bioturbated, although discrete burrows are rare. Toward the bottom, in Core 174A-1071F-9R and interval 10R-1, 0–85 cm, some beds contain planar lamination and, possibly, ripple cross lamination, as well as concretionary carbonate (calcite) beds and nodules.

The remainder of Core 174A-1071F-10R (interval 174A-1071F-10R-1, 85 cm, to 10R-CC, 17 cm) is characterized by normally graded beds of dark gray muddy sand through olive silty clay (Fig. 12). Bases of beds are typically sharp and marked by rare granules or pebbles, and the tops are commonly marked by thin (<0.5 cm) concretionary layers of siderite or dolomite. Most beds exhibit faint planar lamination; biogenic structures (e.g., *Terebellina* and *Teichichnus*) and bioturbation in general are restricted to a few horizons. The graded beds are interpreted as turbidites. This facies is reminiscent of Subunit VA in the roughly coeval submarine-canyon-fill sediments described from Site 906, Leg 150 (Shipboard Scientific Party, 1994b).

The basal part of Subunit IIIA includes olive-colored sandy muds, silty clays, and muddy sands. All of these sediments are micaceous and carbonaceous and contain nodules and thin, graded, and/or laminated beds of concretionary carbonate (siderite or dolomite). Pyrite nodules and shell fragments are observed locally. Bioturbation is evident locally, although faint planar and/or cross lamination is present at some horizons.

Subunit IIIB

Interval: 174A-1071F-11R-CC, 8 cm, to 16R-CC, 15 cm
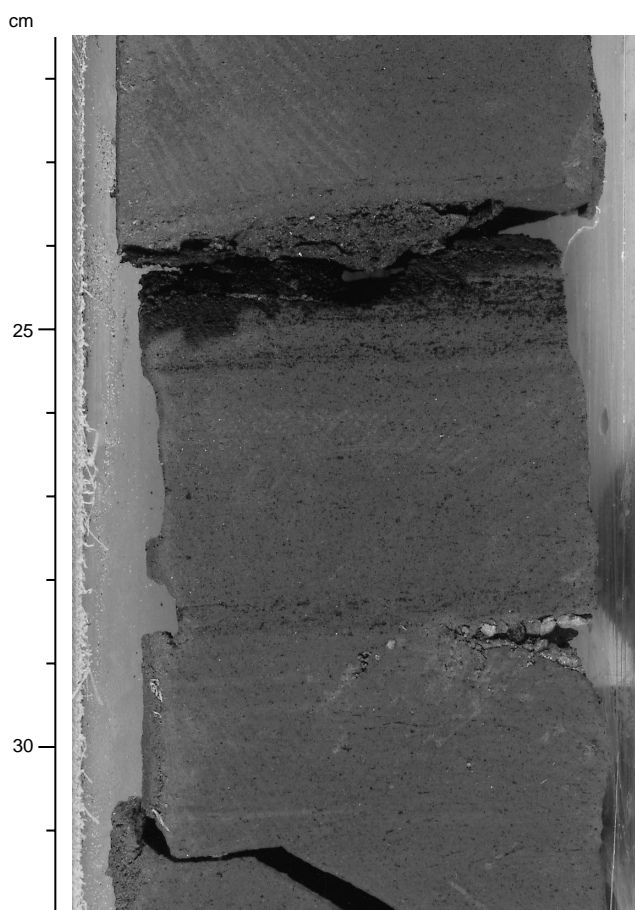
Figure 11. Faintly laminated silty clay with high concentrations of woody organic matter (e.g., 24.5 cm) and quartz granules/very small pebbles (e.g., 28.5 cm). This facies is interpreted as paralic, possibly lagoonal or estuarine (interval 174A-1071F-2R-1, 21.5–32 cm).

Depth: 370.77–414.91 mbsf

Recovery in Subunit IIIB was extremely poor (<1%), presumably because of the predominance of clean sands. Only five very short (<42 cm) cores were recovered over the ~45 m drilled (Cores 174A-1071F-12R through 16R). The upper four cores are characterized by dark gray, slightly micaceous silty clay with rare, thin siderite beds. The lowermost core is a gray pebbly siltstone with sand-filled burrows, some of which are identified as *Ophiomorpha*. The seismic surface m1(s) occurs near the base of Subunit IIIB (between 372 and 412 mbsf; see "Physical Properties," "Seismic Stratigraphy," and "Summary and Conclusions" sections, this chapter).

Mineralogy

X-ray diffraction (XRD) results (Table 3; Fig. 13) indicate that the abundance of detrital minerals varies significantly with depth. However, these variations show no obvious or systematic relations to unit or subunit boundaries, probably because of the necessarily biased nature of the samples through incompletely recovered intervals. Diagenetic minerals do appear to vary systematically with depth. Abundances of calcite and dolomite decrease markedly at the base of Subunit IB and generally remain low to the bottom of the hole (Fig. 13), with the exception of a dolomite peak (based on a single analysis) near the base of Subunit IC. In contrast, both siderite and pyrite appear to increase in abundance progressively downhole to Subunit IID, below which they persist at moderate abundances. These trends
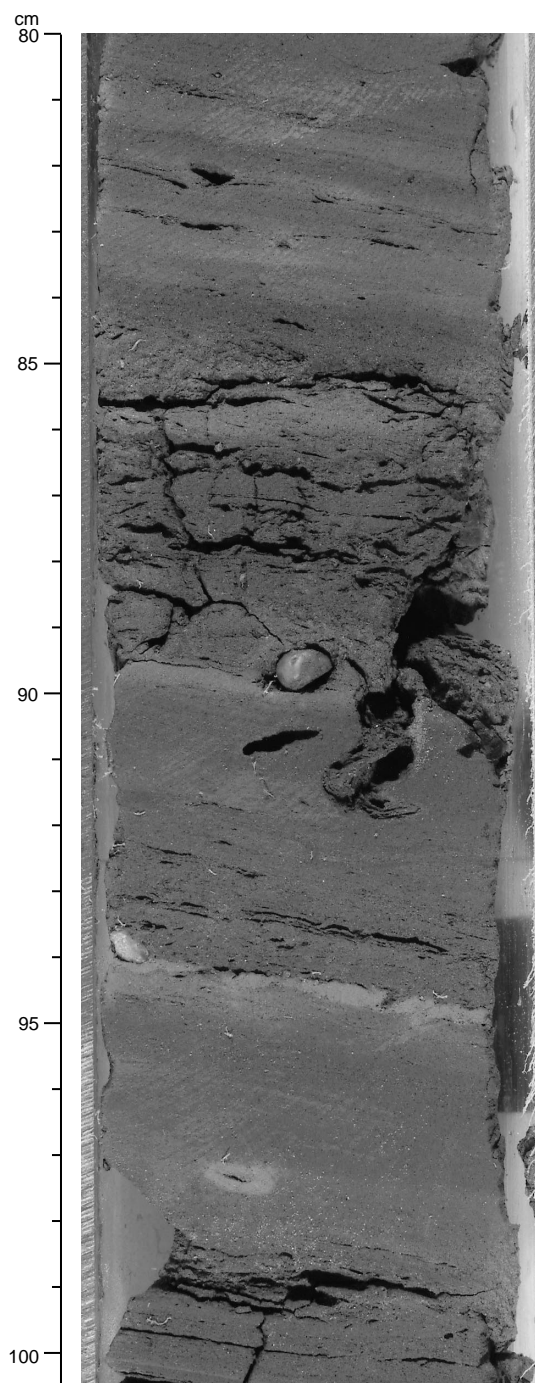
Figure 12. Sharp-based, normally graded beds of coarse sand to silty clay interpreted as turbidites (e.g., 94–89.5 cm; interval 174A-1071F-10R-2, 80–100.5 cm).

reflect changes in diagenetic regimes that are also recorded by downhole changes in alkalinity, pH, and organic carbon (see "Organic Geochemistry" and "Inorganic Geochemistry" sections, this chapter).

Smear-slide analyses also reveal vertical/temporal variations in the abundance of sediment components (Fig. 14). However, smear-slide data are rather limited, particularly for Subunits IA and IB, and significant variations in component abundance may be strongly controlled by grain sizes of the samples. We feel confident commenting on only two components: calcareous and siliceous microfossils. Calcareous microfossils (primarily nannofossils) are absent in Unit I, rel-

atively common in Subunits IIB and IIC, and rare in Unit III. Siliceous microfossils (mostly diatoms and sponge spicules) are restricted largely to Subunits IIC and IIIA. Trends in both calcareous and siliceous microfossils may reflect changes in depositional setting, diagenetic regime, or some combination of both. Peaks in abundance of siliceous microfossils occur near the bases of Subunits IIC and IIIA; these may be interpreted as intervals of condensation and/ or enhanced productivity associated with transgression.

BIOSTRATIGRAPHY

Biostratigraphic resolution at Site 1071 is generally low for calcareous microfossils as a result of strong carbonate dissolution and shallow water conditions that were unfavorable to these planktonic organisms. Nannofossils provide relatively useful zonations for the late Pleistocene, late Pliocene, and the early Pliocene–late Miocene (Figs. 15, 16). Utility of planktonic foraminifers for biostratigraphic zonation is restricted to the earliest Pliocene–middle Miocene.

Pleistocene samples examined from Site 1071 yield benthic foraminiferal faunas that vary from inner neritic (0–50 m) assemblages dominated almost exclusively by *Elphidium excavatum* to more diverse upper middle neritic (~50–65 m) assemblages. These variations may reflect paleodepth fluctuations, substrate (finer grained vs. sandier sediments), and/or changes in depositional input. Miocene benthic foraminifer assemblages indicate middle neritic paleodepths (50–100 m), possibly with fluctuations within this depth zone. Miocene biofacies changes may reflect paleoenvironmental and paleobathymetric changes that occur within a sequence-stratigraphic framework.

Organic microfossils also constrain the biostratigraphic framework at this site. Pollen is useful for dating middle to upper Pleistocene sediments; dinocysts provide biostratigraphic zonation of the early Pleistocene to late middle Miocene. Dinocysts suggest rapid sedimentation during the middle through late Pleistocene, during the late late Miocene, and during the early late Miocene. In contrast, hiatuses were identified in the Pliocene through early Pleistocene, middle late Miocene, and late middle Miocene, suggesting hiatuses during these intervals corresponding to stratigraphic surfaces pp4(s), m0.5(s), and m1(s).

Calcareous Nannofossils

All core-catcher samples, plus additional samples from within several cores, were examined for nannofossils. Nannofossils are generally absent or rare at this site because of strong carbonate dissolution and very shallow water conditions that were unfavorable to these planktonic organisms. Thus, nannofossil biostratigraphic resolution is minimal. The oldest sediment is dated as late Miocene–early Pliocene.

Hole 1071A samples are barren of nannofossils. One to a few specimens of the long-ranging taxa, *Coccolithus pelagicus* and *Reticulofenestra* sp., were found in a few samples (Samples 174A-1071A-3H-CC, 4H-CC, and 8X-CC; 12, 16.16, and 36.45 mbsf), and they are considered reworked from older sediments.

Samples from Hole 1071B are also barren of nannofossils except Sample 174A-1071B-5X-CC (65.69 mbsf), which contains *Gephyrocapsa parallela, Pseudoemiliania lacunosa,* and *Gephyrocapsa* spp. The first two taxa constrain the sample to be nannofossil Subzone CN14a (0.46–0.9 Ma).

The first sample from Hole 1071C (Sample 174A-1071C-2X-CC; 64.42 mbsf) yields *Gephyrocapsa parallela*, *Pseudoemiliania lacunosa, Gephyrocapsa* spp., *Calcidiscus leptoporus,* and *Braarudosphaera bigelowii,* and thus also belongs to Subzone CN14a. Samples from Cores 174A-1071C-3X through 10X (68.46–134.4 mbsf) are barren of nannofossils. Sample 174A-1071C-11X-1, 19 cm (143.7 mbsf), contains rare specimens of *Coccolithus pelagicus, Sphenolithus* spp., and *Reticulofenestra pseudoumbilicus*. The presence of the last two taxa indicate an age of early Pliocene or older. On the other hand, the absence of *Cyclicargolithus floridanus*, a gener-

Table 3. Relative intensity of main peaks for minerals in representative samples from Holes 1071A, 1071B, 1071C, 1071D, and 1071F.

Depth (mbsf)	Quartz	Feldspar	Amphibole	Calcite	Dolomite	Siderite	Pyrite	Clays	Opal-CT
7.25	2359	208	23	207	182	15	21	56	0
10.04	1355	101	32	229	194	16	25	59	0
14.13	1222	134	25	192	87	20	16	62	0
16.83	1174	106	26	200	185	17	24	64	0
40.06	622	208	0	76	63	0	51	41	0
41.72	1378	94	36	146	153	17	18	28	0
49.58	2166	175	30	199	174	17	20	56	0
53.26	1914	250	0	193	156	15	17	33	0
59.28	1558	170	0	153	104	0	28	37	0
59.29	1858	145	48	142	96	0	16	31	0
62.29	877	401	0	243	129	0	28	84	0
63.55	1069	199	0	171	86	0	40	37	0
67.96	1218	62	16	10	23	27	16	41	0
68.30	2410	70	22	15	0	0	23	0	0
96.91	1746	65	17	18	0	34	29	21	0
116.05	3535	475	13	22	70	0	9	26	0
126.64	1743	44	0	30	421	65	13	35	0
134.06	374	30	19	20	0	0	38	74	0
148.56	2234	50	0	17	35	86	16	58	0
152.41	1627	68	20	11	0	103	8	72	0
155.04	3164	116	0	29	32	52	37	49	0
158.79	3711	151	106	9	0	57	29	37	0
167.76	2294	38	25	17	0	45	11	69	0
172.43	2369	156	0	6	30	37	57	65	0
174.15	5620	13	22	26	0	26	13	27	0
200.75	4041	113	25	21	16	56	113	28	0
229.36	4213	31	21	21	13	80	31	41	0
238.50	3638	40	25	20	13	78	40	42	18
247.46	4951	56	26	16	15	51	56	28	13
256.59	2977	24	22	11	12	42	24	50	0

Note: See Figure 13.
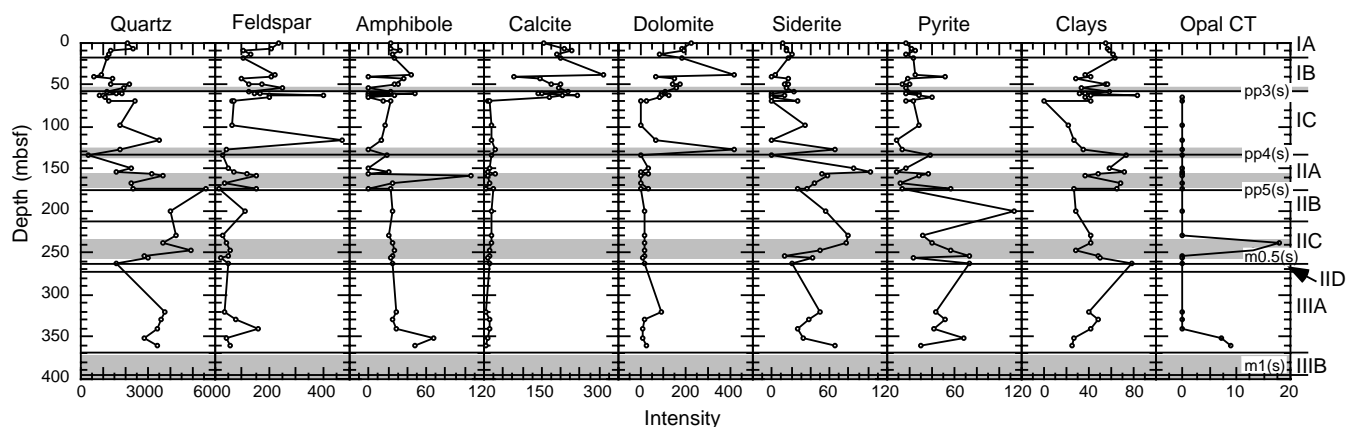
Figure 13. Peak intensities vs. depth (mbsf) in XRD analyses of common minerals at Site 1071. Lithologic subunit boundaries (IA–IIIB) are shown as solid lines. Gray shaded areas show depth ranges of seismic surfaces calculated using the velocity curve derived from Oc270, Profile 51 (see Table 40, "Seismic Stratigraphy" section, this chapter).

ally abundant species in the middle Miocene and older marine sediments worldwide, indicates an age of late Miocene or younger for this sample. Rare specimens of *Reticulofenestra pseudoumbilicus* and/or *Sphenolithus* spp. were found in a number of samples downhole to Sample 174A-1071C-24X-CC (248 mbsf), whereas *Cyclicargolithus floridanus* is absent. Thus, this interval is assigned an age of late Miocene–early Pliocene. Samples 174A-1071C-25X-3, 14 cm (254.7 mbsf), and 25X-CC (257.2 mbsf) from the last core of this hole are barren of nannofossils.

The first five samples of Hole 1071D (Samples 174A-1071D-1R-CC through 5R-CC; 62–38.3 mbsf) are barren of calcareous nannofossils. Samples 174A-1071D-6R-CC (48.77 mbsf) through 8R-CC (63.26 mbsf) contain rare to few specimens of small *Gephyrocapsa* spp., which are of little biostratigraphic value.

Hole 1071F yields *Reticulofenestra pseudoumbilicus, R. producta,* small *Reticulofenestra, Sphenolithus* spp., and *Coccolithus pelagicus.* These assemblages indicate an age of early Pliocene or older, but do not provide a useful constraint for the older age limit.

Planktonic Foraminifers

To the total depth of 50.13 mbsf (Sample 174A-1071A-10X-CC) in Hole 1071A, samples were essentially barren of planktonic foraminifers. Only two samples at 12.00 and 25.83 mbsf (Sample 174A-1071A-3H-CC: one specimen; and Sample 174A-1071A-5H-CC: three specimens) contained juvenile foraminifers and the long-ranging species *Globigerina bulloides*. The paucity of planktonic foraminifers is most likely attributable to dissolution and the shallow (inner-middle neritic) paleoenvironments, as interpreted from benthic foraminifers. Based on the benthic foraminifers and pollen present in this section, these samples are presumed to be no older than late Pleistocene age.

Sediments from 41.85 to 68.14 mbsf in Hole 1071B (Samples 174A-1071B-2X-CC through 6X-CC) are also essentially barren of planktonic foraminifers, again as a result of dissolution and shallow paleoenvironments. Samples 174A-1071B-2X-CC (41.85 mbsf) and 174A-1071B-3X-CC (49.74 mbsf) contain one and two juvenile
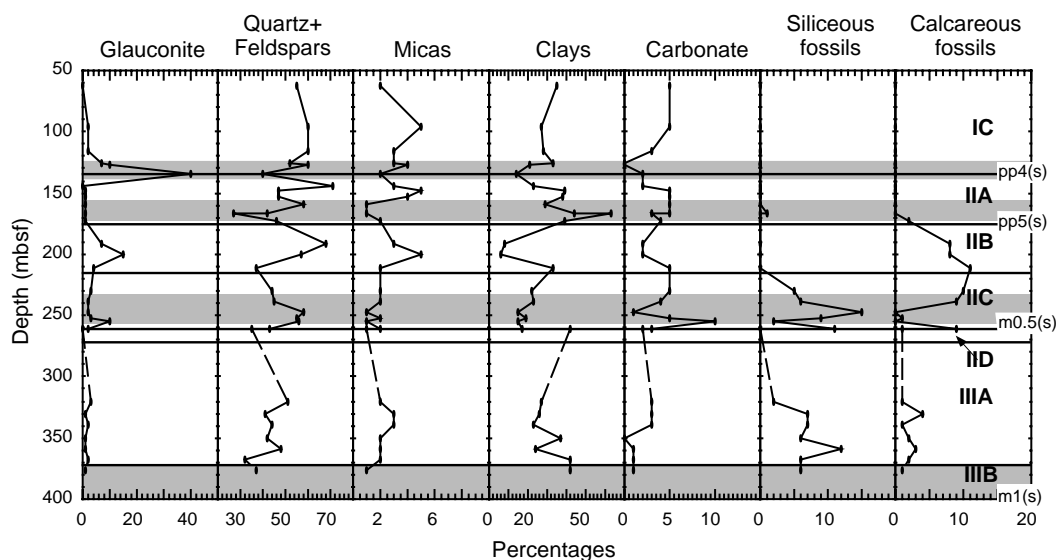
Figure 14. Percentages of glauconite, quartz + feldspars, micas, clays, carbonate, siliceous fossils (mostly diatoms and sponge spicules), and calcareous fossils (mostly nannofossils) based on smear slides of Hole 1071C. Lithologic subunit boundaries (IC–IIIB) are shown. Gray shaded areas show depths of seismic surfaces calculated using the velocity curve derived from Oc270, Profile 51 (see "Seismic Stratigraphy" section, this chapter).

planktonic foraminifers, respectively. This stratigraphic interval extends down through the upper Pleistocene, based on calcareous nannofossil biostratigraphy.

Sediments in Hole 1071C from 64.42 (Sample 174A-1071C-2X-CC) to 129.2 mbsf (Sample 174A-1071C-9X-CC) are presumed to be of Pliocene–Pleistocene age, based on calcareous nannofossil biostratigraphy. Only three samples contained planktonic foraminifers in this part of the section. When present, they continue to be very rare to frequent in abundance. Species found in this section include *Globigerina bulloides, Globigerinoides trilobus, Globorotalia inflata, Globigerinella pseudobesa, Neogloboquadrina pachyderma,* and *Orbulina universa.* All of these species are long-ranging and do not assist in biostratigraphic zonation of this part of the stratigraphic interval. Sample 174A-1071C-10X-CC, at 134.4 mbsf, is barren of foraminifers and is composed almost solely of glauconite. This sample is coincident with the predicted depth range of pp4(s), a stratigraphic discontinuity interpreted from seismic data at the site (see "Seismic Stratigraphy" section, this chapter). Below this surface, sediments containing planktonic foraminifers are diagnostic of lowermost Pliocene to upper Miocene sediments from 143.69 (Sample 174A-1071C-11X-1, 19–21 cm) to 172.3 mbsf (Sample 174A-1071C-15X-CC). In the lowermost Pliocene to upper Miocene section, planktonic foraminifers range in abundance from rare to common. The fauna is characterized by *Globigerina bulloides, Globigerina woodi, Globigerinita glutinata, Globigerinoides trilobus, Globorotalia menardii, Globorotalia scitula, Globorotalia juanai,* and *Neogloboquadrina pachyderma* (right and left coiling). The presence of *Globorotalia juanai,* although very rare, at 163.11 mbsf (Sample 174A-1071C-14X-CC) suggests that the sediments are earliest Pliocene to late Miocene (4.9–8.1 Ma; Chaisson and Leckie, 1993; Berggren et al., 1995). The planktonic faunas from this interval suggest that sediments between seismic surface pp5(s) (156–172 mbsf; see "Seismic Stratigraphy" section, this chapter) and seismic surface pp4(s) (124–138 mbsf; see "Seismic Stratigraphy" section, this chapter) are earliest Pliocene to late Miocene in age. Furthermore, changes are present in the relative abundances of *Globigerina bulloides* (cool- to temperate-water indicator) and *Neogloboquadrina pachyderma* (cold-water indicator). In the lower part of this interval, from 172.3 (Sample 174A-1071C-15X-CC) to 157.38 mbsf (Sample 174A-1071C-13X-CC), *Globigerina bulloides* dominates over the abundance of *Neogloboquadrina pachyderma.* Some samples contain abundant *Globigerina bulloides* but few to no specimens of *Neogloboquadrina pachyderma.* Where *Neogloboquadrina pachyderma* is present (rare abundances) in this lower part of the interval, it is consistently sinistrally coiled. In the upper part of the interval, from 153.63 to 143.69 mbsf (Samples 174A-1071C-12X-CC, 11X-CC, and 11X-1, 19–21 cm), *Neogloboquadrina pachyderma* (exclusively dextrally coiled) is present in much higher abundances than *Globigerina bulloides.* Ratios of *Neogloboquadrina pachyderma* to *Globigerina bulloides* are as high as 17:2. Further shore-based studies may allow for a better understanding of potential climatic variations recorded in this early Pliocene to late Miocene stratigraphic interval.

In Hole 1071D, planktonic foraminifers are absent to extremely rare from 0.62 (Sample 174A-1071D-1R-CC) to 48.77 mbsf (Sample 174A-1071D-6R-CC). Sample 174A-1071D-4R-CC (28.30 mbsf) yields two unidentifiable, broken specimens, and Sample 174A-1071D-5R-CC (38.30 mbsf) contains one *Neogloboquadrina pachyderma* and one *Orbulina universa.* Planktonic foraminifers are rare to frequent from 57.83 (Sample 174A-1071D-7R-CC) to 63.26 mbsf (Sample 174A-1071D-8R-CC). The latter sample contains *Globigerina bulloides, Globigerina quinqueloba, Globigerinoides immaturus, Globigerinoides ruber, Globigerinoides sacculifer, Globorotalia inflata,* and *Neogloboquadrina pachyderma.*

In Hole 1071F, planktonic foraminifers are absent to extremely rare from 255.04 (Sample 174A-1071F-1R-CC) to 351.47 mbsf (Sample 174A-1071F-9R-CC). The presence of extremely rare *Neogloboquadrina pachyderma* in Sample 174A-1071F-2R-CC (261.85 mbsf) suggests an age of <9.2 Ma. Because this sample is calibrated to be just above the m0.5(s) seismic boundary (see "Seismic Stratigraphy" section, this chapter), sediments immediately above this boundary are probably no older than 9.2 Ma (Fig. 16). In the interval from 363.15 (Sample 174A-1071F-10R-CC) to 405.57 mbsf (Sample 174A-1071F-15R-CC), planktonic foraminifers are rare to frequent. The exception is in Samples 174A-1071F-13R-CC (386.35 mbsf) and 14R-CC (395.87 mbsf), where planktonic foraminifers are absent. Species found in the interval from 363.15 (Sample 174A-1071F-10R-CC) to 405.57 mbsf (Sample 174A-1071F-15-CC) include *Globigerina bulloides, Globigerina* cf. *brazieri, Globigerina praebulloides, Globoquadrina* cf. *dehiscens, Neogloboquadrina continuosa, Neogloboquadrina mayeri,* and *Neogloboquadrina pachyderma.* The presence of *Neogloboquadrina mayeri* in Samples 174A-1071F-10R-CC (363.15 mbsf), 12R-CC (376.94 mbsf), and 15R-CC
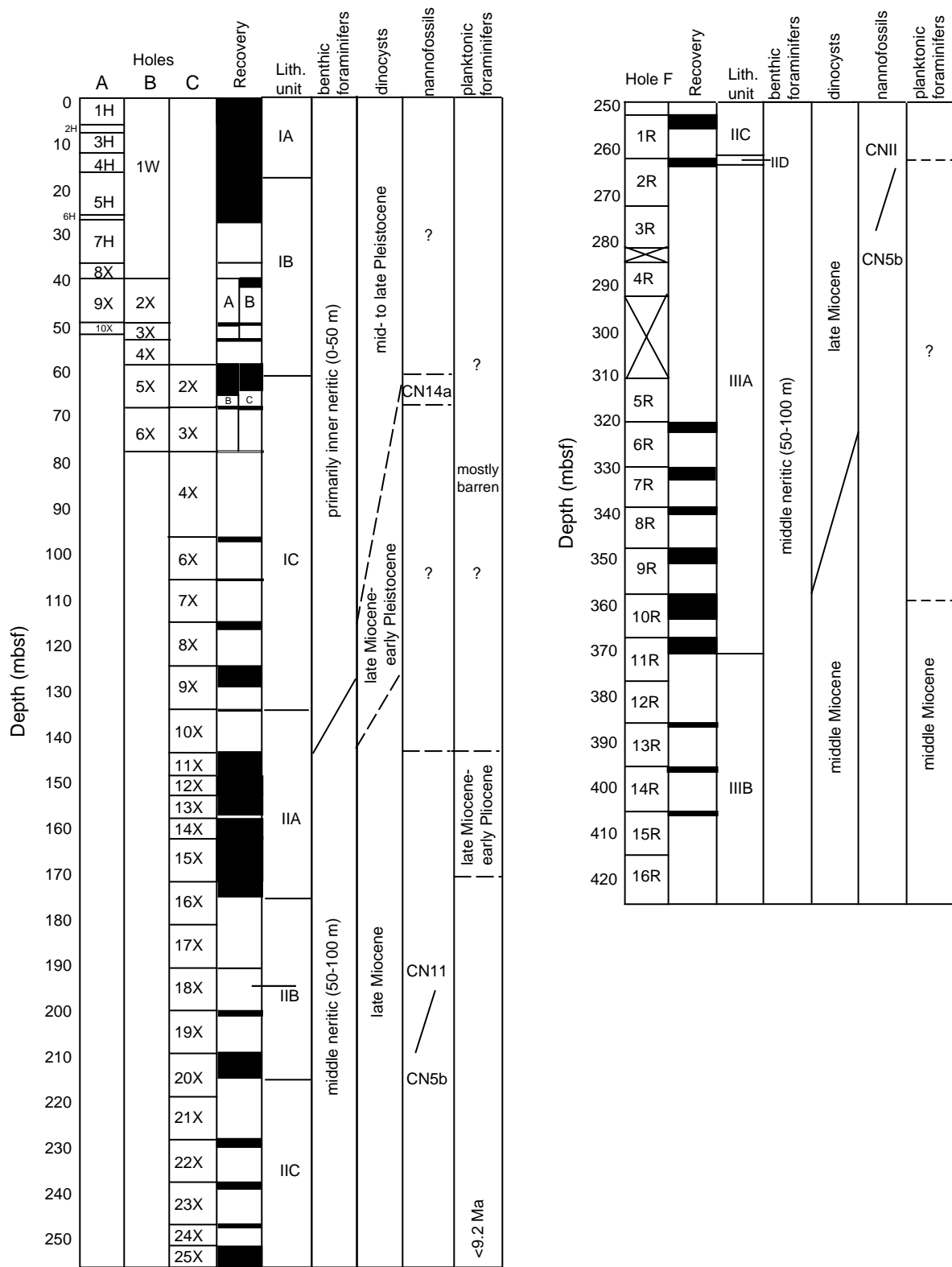
Figure 15. General geologic ages interpreted from dinocyst, nannofossil, and planktonic foraminiferal assemblages, and paleobathymetry as interpreted from benthic foraminifers, at Site 1071.
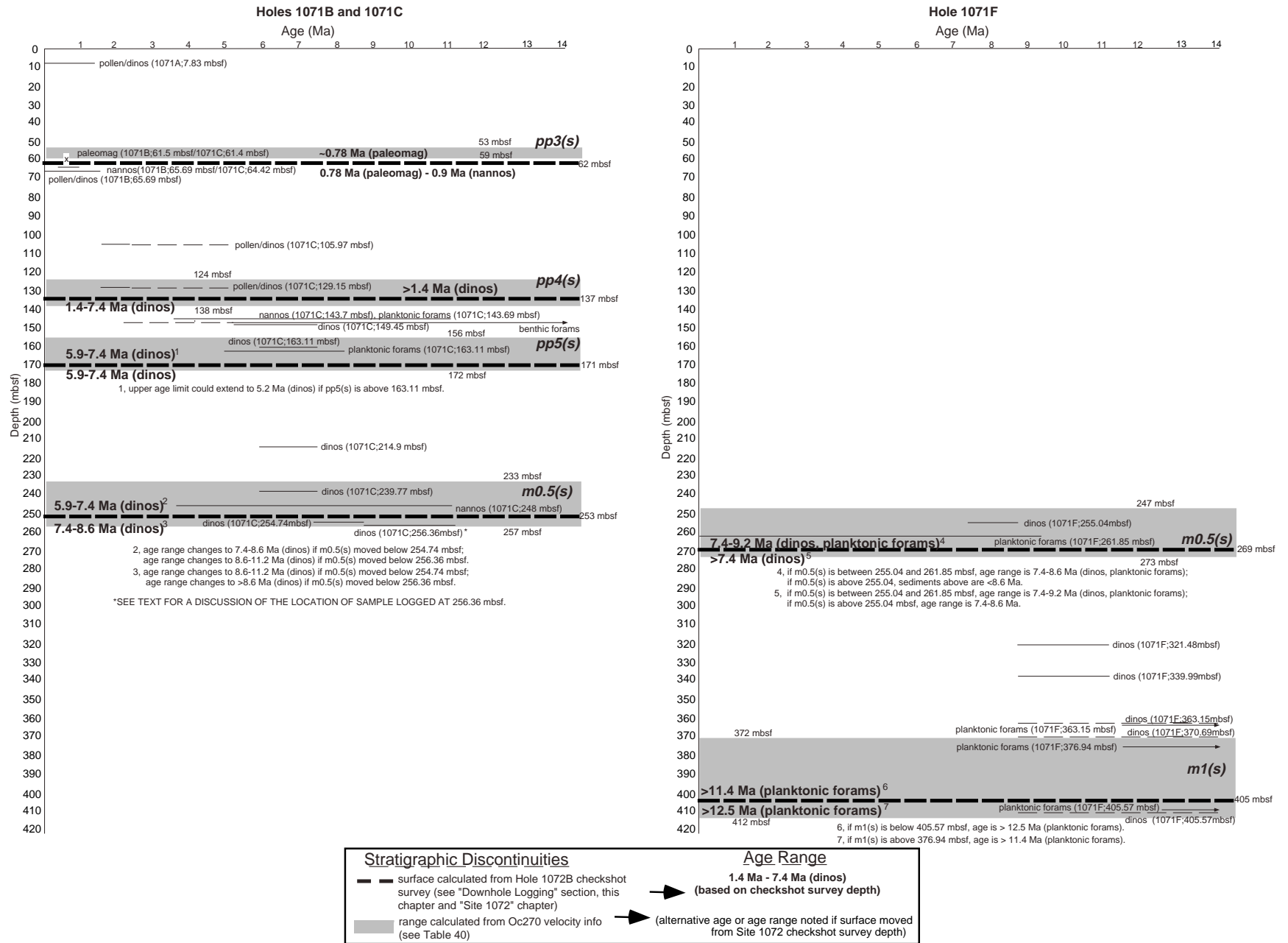
Holes 1071B and 1071C

Hole 1071F

Figure 16. Age-depth plot, showing the age ranges interpreted from microfossil assemblages at Site 1071. Stratigraphic discontinuities pp3(s), pp4(s), pp5(s), m0.5(s), and m1(s) are also illustrated (see "Seismic Stratigraphy" and "Downhole Logging" sections, this chapter). Dinos = dinocysts; paleomag = paleomagnetism; nannos = nannofossils; forams = foraminifers.

(405.57 mbsf) suggests that the sediments are >11.4 Ma in age. Furthermore, the presence of *Paragloborotalia acrostoma* (LAD in Zone N11 = 12.7–12.5 Ma) in Sample 174A-1071F-15R-CC (405.57 mbsf) indicates an age of >12.5 Ma. These data suggest that m1(s) is at least as old as 11.4 Ma (see also "Seismic Stratigraphy" section, this chapter).

Wherever possible, the percentage of planktonics relative to total foraminifers was noted for all samples studied. In Holes 1071A and 1071B, the percentage of planktonic foraminifers is 0%–3%. In the interval from 143.69 (Sample 174A-1071C-11X-1, 19–21 cm) to 172.27 mbsf (Sample 174A-1071C-15X-CC) of Hole 1071C, the percentage of planktonic foraminifers varies from <1% (Sample 174A-1071C-13X-CC; 157.38 mbsf) to 40% (Sample 174A-1071C-15X-CC; 172.27 mbsf), with an average of 13% in Samples 174A-1071C-11X-1, 19–21 cm, 11X-CC, and 12X-CC. In Holes 1071D and 1071F, the percentage of planktonic foraminifers is 0%–5%.

Benthic Foraminifers

Core-catcher samples and samples from within cores were examined for benthic foraminifers from Holes 1071A, 1071B, 1071C, 1071D, and 1071F. Benthic foraminiferal abundances range from barren to common in Pleistocene samples examined from Site 1071 (Samples 174A-1071A-1H-CC through 174A-1071C-9X-3, 52–54 cm; 5.12–128.02 mbsf). Most of the Pleistocene samples are dominated by *Elphidium excavatum*, indicating inner neritic paleodepths (0–50 m) based on the distribution of modern *Elphidium* biofacies on the New Jersey shelf (Poag et al., 1980) and the Chesapeake Bay shelf (Ellison and Nichols, 1976). Relative abundance changes of *Elphidium excavatum forma clavatum* (glacial; decrease in water depth) and *Elphidium excavatum forma lidoensis* (interglacial; increase in water depth; Buck and Olson, in press) in core-catcher samples indicate that a high-resolution study may provide a detailed record of relative water-depth changes and glacial/interglacial cycles in the Pleistocene section at Site 1071. In addition to *Elphidium* spp., other species that are rare to common in the Pleistocene section include *Astacolus hyalacrulus, Cibicides lobatulus, Nonionella miocenica stella,* and *Quinqueloculina seminulum.* Several sporadic Pleistocene samples yield more diverse benthic foraminiferal assemblages, including *Astacolus hyalacrulus, Bolivina subaenariensis, Buccella frigida, Bulimina marginata, Cibicides lobatulus, Cibicidoides* spp., *Globobulimina auriculata, Nonionella miocenica stella,* and *Quinqueloculina seminulum.* These more diverse assemblages may reflect slightly deeper paleodepths, possibly within the upper middle neritic zone. Stratigraphic biofacies distribution may also be related to substrate (finer grained vs. sandier sediments) and/or changes in sediment input.

Benthic foraminifers are absent to common in Miocene samples from Holes 1071C and 1071F (Samples 174A-1071C-11X-1, 19–21 cm, through 24X-CC, 143.69–247.96 mbsf; and Samples 174A-1071F-1R-CC through 15R-CC, 255.04–405.57 mbsf). *Buliminella gracilis* and *Uvigerina juncea* are the most abundant species found in most of the Miocene samples from Hole 1071C (Samples 174A-1071C-11X-1, 19–21 cm, through 19X-1, 85–89 cm; 143.69–200.95 mbsf), indicating middle neritic paleodepths (50–100 m). Miocene faunas from Hole 1071F (Samples 174A-1071F-1R-CC through 15R-CC; 255.04–405.57 mbsf) are characterized by high abundances of *Buliminella gracilis.* Samples containing more abundant *Buliminella gracilis* may indicate slightly shallower paleodepths (50–80 m) than samples containing more abundant *Uvigerina juncea* (75–100 m), based on faunal studies from New Jersey Coastal Plain boreholes (Miller et al., 1997). Other typical species in these *Buliminella-Uvigerina*-dominated faunas include *Cassidulina laevigata, Nonionella miocenica, Quinqueloculina seminulum,* and *Textularia agglutinans.* This *Buliminella-Uvigerina* biofacies may indicate a paleoenvironment that was rich in organic carbon and/or low in dissolved oxygen content (Snyder et al., 1989; Miller et al., 1997). In contrast,

Buliminella and *Uvigerina* are rare or absent from Samples 174A-1071C-22X-1, 90–92 cm, through 174A-1071F-1R-CC (229.30–255.04 mbsf); these samples are characterized by *Cibicidoides* spp., *Lenticulina americana spinosa,* and *Marginulina dubia,* and may reflect less restricted paleoenvironmental conditions. Detailed studies may reveal that these biofacies changes reflect paleoenvironmental and paleobathymetric fluctuations that occur within a sequence-stratigraphic framework.

Palynomorphs

Sediments examined above ~105.97 mbsf at Site 1071 are assigned an age of less than ~1.4 Ma based on the rich pollen assemblage, with high percentages of *Picea* (spruce) and nonarboreal pollen suggesting glacial conditions on the New Jersey margin from Samples 174A-1071A-2H-CC through 174A-1071B-5X-CC (7.83–65.69 mbsf). Sparse dinocyst assemblages dominated by *Brigantedinium* spp. and *Algidasphaeridium minutum* (= *Multispinula minuta*) over this interval are consistent with the pollen interpretation. Samples 174A-1071C-7X-CC (105.97 mbsf) and 9X-CC (129.15 mbsf) contain richer dinocyst assemblages that can be assigned to the uppermost Miocene to lowermost Pleistocene based on the presence of *Operculodinium israelianum, Brigantedinium* spp., *Habibacysta tectata, Achomosphaera* spp., *Spiniferites* spp., *Tectatodinium pellitum, Filisphaera microornata,* and *Invertocysta lacrymosa.* Sample 174A-1071C-11X-CC (149.45 mbsf) is late Miocene in age, based on the presence of *Pyxdiella simplex, Operculodinium janduchenei, Filisphaera microornata, Operculodinium? eirikianum,* and *Lingulodinium machaerophorum.* Samples 174A-1071C-14X-CC (163.11 mbsf), 20X-CC (214.9 mbsf), and 23X-CC (239.77 mbsf) are assigned to late late Miocene Zone DN10 (7.4–5.9 Ma) of de Verteuil and Norris (1996), based on the common occurrence of *Spiniferites* spp., *Achomosphaera andalousiensis, Lejeunecysta* spp., *Selenopemphix brevispinosa, Operculodinium janduchenei, Habibacysta tectata, Lingulodinium machaerophorum, Brigantedinium* spp., and *Tectatodinium pellitum* in a rich dinocyst flora, together with *Operculodinium israelianum, Selenopemphix quanta, Trinovantedinium papulum, Melitasphaeridium choanophorum,* and *Cyclopsiella granosa.* Sample 174A-1071F-1R-CC (255.04 mbsf) is assigned to Miocene Zone DN9 (8.6–7.4 Ma) of de Verteuil and Norris (1996) based on the occurrence of *Barssidinium evangelineae,* whose first appearance datum (FAD) defines the base of this zone, together with several specimens of *Hystrichosphaeropsis obscura,* which last occurs at the top of Zone DN9. Protoperidinioid taxa dominate the assemblage in this sample (e.g. *Selenopemphix dionaeacysta, Selenopemphix brevispinosa, Trinovantedinium papulum, Lejeunecysta* spp., and *Brigantedinium* spp.), although *Polysphaeridium zoharyi, Operculodinium israelianum, Tectatodinium pellitum,* and *Habibacysta tectata* are also present. Sample 174A-1071C-25X-3, 14–17 cm (254.74 mbsf), is also dominated by protoperidinioid cysts like *Lejeunecysta* spp., *Brigantedinium* spp., and *Selenopemphix nephroides,* and is assigned to middle late Miocene Zone DN9 of de Verteuil and Norris (1996) based on the occurrence of *Dapsilidinium pseudocolligerum,* whose last appearance datum (LAD) around 7.4 Ma defines the top of Zone DN9. The presence of rare specimens of *Paleocystodinium golzowense* in Sample 174A-1071C-25X-CC (257.22 mbsf), together with *Selenopemphix brevispinosa, Selenopemphix dionaeacysta, Operculodinium centrocarpum, Hystrichosphaeropsis obscura,* and *Brigantedinium* spp., suggests deposition during the early late Miocene (DN8; ~11.2–8.6 Ma). No dinocysts were found in Sample 174A-1071F-2R-CC (261.85 mbsf), but the sample is pollen rich and contains fungal spores, suggesting nearshore conditions with a high influx of terrigenous material or possible subaerial exposure. Samples 174A-1071F-6R-CC (321.48 mbsf) and 8R-CC (339.99 mbsf) are assigned to Zone DN8. *Selenopemphix brevispinosa* is common in these samples, together with *Selenopemphix nephroides, Selenopemphix dionaeacysta, Trinovantedinium papulum, Trino-*

vantedinium harpagonium, Brigantedinium spp., *Operculodinium piaseckii, Lingulodinium machaerophorum, Achomosphaera* spp., *Habibacysta tectata*, and *Paleocystodinium golzowense*, whose LAD marks the top of Zone DN8.

Samples 174A-1071F-10R-CC (363.15 mbsf) and 11R-CC (370.69 mbsf) contain relatively sparse dinocyst assemblages that are strongly dominated by protoperidinioid taxa (e.g. *Brigantedinium* spp., *Selenopemphix nephroides, Selenopemphix brevispinosa*, and *Trinovantedinium papulum*), recording nearshore/shallow water conditions. The presence of *Batiacasphaera sphaerica* constrains the age of these samples to older than Zone DN9 (8.6–7.4 Ma), whereas the presence of *Habibacysta tectata* constrains the age to <14 Ma; it was not possible to constrain the age more definitively than this. If, however, the planktonic foraminifers in this interval are in situ, the sediments must be >11.4 Ma. If the age of the lower boundary of Zone DN8 is correct (11.2 Ma), these sediments must belong to Zones DN5, DN6, or DN7, and in the absence of *Systematophora placantha* and *Cannosphaeropsis passio,* which occur consistently in Zones DN5 and DN7 respectively (de Verteuil and Norris, 1996), these samples are tentatively assigned to Zone DN6, which spans ~13.2–12.7 Ma. Sample 174A-1071F-15R-CC (405.57 mbsf) is less tentatively (although not definitively) assigned to Zone DN6, based on the presence of both *Paleocystodinium golzowense* and *Habibacysta tectata* in a protoperidinioid-dominated assemblage (with common *Brigantedinium* spp., *Lejeunecysta* spp., *Selenopemphix nephroides*, and *Trinovantedinium papulum* (cf. de Verteuil and Norris, 1996, p. 13). Thus, the age of the sediments below the stratigraphic discontinuity interpreted to be m1(s) appears to be ~13.2–12.7 Ma, which is compatible with the age of >12.5 Ma that was interpreted from planktonic foraminifers (see "Seismic Stratigraphy" section, this chapter).

Terrigenous organic matter is common to abundant in all samples studied, recording neritic conditions since the late middle Miocene. The absence of marine palynomorphs in Sample 174A-1071F-2R-CC (261.85 mbsf) probably records estuarine conditions. The abundance of protoperidinioid dinocysts in most samples also records neritic conditions. Dinocyst abundance is generally much higher prior to the middle Pleistocene, probably reflecting greater productivity and/or less dilution by inorganic sediments before the advance of ice sheets to middle latitudes in North America. Rapid sedimentation is recorded through the middle to late Pleistocene, during the late late Miocene, and during the early late Miocene. In contrast, hiatuses were identified in the Pliocene through early Pleistocene, middle late Miocene, and late middle Miocene, suggesting hiatuses during these intervals corresponding to stratigraphic surfaces pp4(s), m0.5(s), and m1(s). There is no palynological evidence for a hiatus associated with surfaces pp3(s) or pp5(s), which occur within dinocyst zones.

Biostratigraphic Age Control of Stratigraphic Discontinuities

Where possible, biostratigraphic ages or age ranges were calibrated with stratigraphic discontinuities pp3(s), pp4(s), pp5(s), m0.5(s) and m1(s) for Site 1071. Biostratigraphic age control is derived from three holes: 1071B, 1071C and 1071F. Because Holes 1071B and 1071C are ~1 km from Hole 1071F, and some of the stratigraphic discontinuities vary in depth over that distance, two separate calibration charts were made for Site 1071 (Fig. 16).

Holes 1071B and 1071C are useful in dating late Miocene through Pleistocene stratigraphic discontinuities. Using the Hole 1072B checkshot survey, pp3(s) was estimated at 62 mbsf (see "Downhole Logging" sections, this chapter and "Site 1072" chapter, this volume). Based on the paleomagnetic interpretation of the B/M boundary (0.78 Ma), in conjunction with compatible pollen, dinocyst, and calcareous nannofossil data, the best age estimate from this site is ~0.78 Ma for the sediments above and 0.78–0.9 Ma for sediments below 62 mbsf (Fig. 16). Changing the depth of pp3(s) to be within the predrill estimated interval of the surface (53–59 mbsf) based on

Oc270 seismic velocity information would not significantly alter this age interpretation for Holes 1071B and 1071C (see "Seismic Stratigraphy" section, this chapter).

The age assignment of sediments above and below pp4(s) in Holes 1071B and 1071C is derived from the Hole 1072B checkshot survey depth estimate of 137 mbsf (Fig. 16; see "Downhole Logging" section, this chapter). Pollen and dinocysts indicate that sediments above the surface must be >1.4 Ma. Sediments below pp4(s) range from 1.4 to 7.4 Ma based on dinocysts; this age range is compatible with calcareous nannofossils and planktonic foraminifers also recovered from sediments below pp4(s). A variation in depth for pp4(s) within the predrill, seismically predicted range of this surface (124–138 mbsf) would not significantly alter these age estimates (see "Seismic Stratigraphy" section, this chapter).

Dinocysts provide age estimates for sediments above and below pp5(s) in Holes 1071B and 1071C. Based on the Hole 1072B checkshot survey depth estimate of 171 mbsf for this surface, sediments above and below pp5(s) are of the same age range of 5.9–7.4 Ma (Fig. 16; see "Downhole Logging" section, this chapter). These ages are compatible with planktonic foraminifers recovered above pp5(s). The age range of sediments above pp5(s) could be 5.2–7.4 Ma, if pp5(s) were actually located above 163.11 mbsf within the predrill seismically predicted interval (156–172 mbsf; see "Seismic Stratigraphy" section, this chapter).

Because three holes (1071B, 1071C, and 1071F) may have penetrated m0.5(s), and there is relief on this surface over an ~1-km distance (see "Seismic Stratigraphy" section, this chapter), separate biostratigraphic calibrations were made for Holes 1071B and 1071C and Hole 1071F (Fig. 16). At Holes 1071B and 1071C, dinocysts suggest that sediments above m0.5(s) range in age from 5.9 to 7.4 Ma, whereas sediments below the surface (~253 mbsf based on Hole 1072B checkshot survey) range in age from 7.4 to 8.6 Ma (Fig. 16). The interpretation of ages is complicated by both a somewhat condensed stratigraphic interval and potential imprecision in the position with depth of m0.5(s) (see "Summary and Conclusions" section, this chapter). For example, if within the seismically predicted interval for this surface (233–257 mbsf) m0.5(s) is repositioned below 254.74 mbsf, the age range of sediments above and below the boundary becomes significantly older. In this case, sediments above m0.5(s) would have an age range of 7.4–8.6 Ma and sediments below m0.5(s) would range in age from 8.6 to 11.2 Ma. Calcareous nannofossils from within the seismically predicted interval do not allow for further age refinement. If m0.5(s) were repositioned below 256.36 mbsf, sediments above the surface would be 8.6–11.2 Ma and sediments below m0.5(s) would be >8.6 Ma based on dinocysts. The depth location of this particular dinocyst sample (256.36 mbsf; Fig. 16) is problematic and quite crucial for determining the age of sediments associated with m0.5(s). This particular sample (174A-1071C-25X-CC) was logged in at 257.22 mbsf on deck; however, because recovery was 117% (i.e., recovery > penetration), the sample is here logged in at 256.36 mbsf (Fig. 16), which is compatible with barrel sheets for this section (see "Lithostratigraphy" section, this chapter). It is possible, therefore, that this sample is actually from a slightly lower depth than 256.36 mbsf. Because three separate dinocyst zones are present between 239 and 259 mbsf, the repositioning of either samples or stratigraphic surfaces with depth results in significantly different geologic conclusions.

Hole 1071F permits age assignments for sediments in proximity to m0.5(s) and m1(s). The checkshot survey depth for m0.5(s) is ~269 mbsf (see "Downhole Logging" sections, this chapter and "Site 1072" chapter, this volume). Both dinocysts and planktonic foraminifers indicate an age range of 7.4–9.2 Ma for sediments above the surface. Dinocysts constrain the age range of the sediments below the boundary to >7.4 Ma (Fig. 16). Moving the depth of m0.5(s) within the seismically predicted interval (247–273 mbsf, see "Seismic Stratigraphy" section, this chapter) would result in changes in the age interpretations. If m0.5(s) is moved to above 255.04 mbsf, the age

range for sediments above the surface would then be <8.6 Ma. The age for sediments underlying m0.5(s) positioned above 255.04 mbsf would be 7.4–8.6 Ma. If m0.5(s) were between 255.04 and 261.85 mbsf, sediments above the surface would be 7.4–8.6 Ma and sediments below the surface would be 7.4–9.2 Ma. Discrepancies appear to exist between the age range of sediments above and below m0.5(s) at Holes 1071B and 1071C and Hole 1071F. This may be a result of the calibration of m0.5(s) with depth between locations, stratigraphic geometries (e.g., relief of the surface between Hole 1071A–Hole 1071E and Hole 1071F–Hole 1071G), or perhaps other geologic or sampling reasons.

Planktonic foraminifers and dinocysts provide age calibration for m1(s) in Hole 1071F. At the checkshot survey depth of 405 mbsf, sediments above m1(s) are >11.4 Ma, and sediments below the surface are >12.5 Ma. (If the tentative assignment of Zone DN6 [~13.2–12.7 Ma] at 405.57 mbsf is correct, further age refinement may be possible.) If m1(s) were moved within the seismically predicted range (372–412 mbsf) to below 405.57 mbsf, the age of sediments above m1(s) would be >12.5 Ma. If m1(s) were shifted to above 376.94 mbsf, the age of sediments below the surface could be as young as 11.4 Ma.

The age interpretations of these stratigraphic discontinuities are based solely on biostratigraphic data produced during the cruise. Because of problems with dissolution, reworking, and shallow paleobathymetry at this site (see sections on specific fossil groups in this report), caution should be employed when using any of these age determinations. Further shore-based work on biostratigraphy, paleomagnetism, and isotope stratigraphy may help fine-tune these ages.

PALEOMAGNETISM

All archive-half sections from Holes 1071A (APC and XCB cores), 1071B, and 1071C (XCB cores) were subjected to routine pass-through measurements except sections from Core 174A-1071A-1H and Sections 174A-1071A-5H-2 through 5H-7, because they were sandy and highly disturbed by drilling (Tables 4–23 on CD-ROM, back pocket, this volume). The natural remanent magnetization (NRM) was remeasured routinely using the pass-through cryogenic magnetometer at intervals of 5 cm. After measuring the NRM, sections were partially demagnetized at 10 mT and 20 mT to remove overprints and were remeasured. More detailed demagnetization up to 40 mT was conducted for several selected samples. Higher resolution measurements were also made at intervals of 5 mm on selected archive-half sections.

Discrete cube samples were taken one per section and AF demagnetized at nine steps up to 80 mT (Table 24). Typical examples of demagnetization plots for discrete cube samples and archive sections are presented in Figure 17. Figures 17B, D, and F are plots for archive-half sections, and Figures 17A, C, E, G, and H are for discrete cube samples. Stable magnetization components were obtained for most of the sediments above 200 mbsf, whereas below 200 mbsf, the sediment samples showed relatively unstable character due to low magnetization intensity (Figs. 17G, H). The NRM inclinations are almost always strongly biased toward high positive inclinations, which is inconsistent with the ~58° inclination expected for an axial dipole field at the latitude of this site. The observed inclinations indicate that a magnetic overprint is present as identified on many previous DSDP and ODP legs. This secondary overprint is characterized by steep inclinations and is probably acquired during drilling. These overprints were usually removed by AF demagnetization up to 20 mT.

After removing a drill string-overprint steep positive inclination, the paleomagnetic directions of discrete cube samples and archive samples of corresponding horizons agreed very well for most of the APC core samples (Figs. 17A, B). However, some of the archive-half sections showed paleomagnetic directions (e.g., Fig. 17D) with opposite magnetic polarity from those of discrete samples (e.g., Fig. 17C).

This kind of pseudo-reversal was also found in archive-half sections of APC cores on Leg 161 (Shipboard Scientific Party, 1996c). The mechanism is not clear; however, mechanical drag of sediment at the margin of the core close to the core liner enables acquisition of a relatively stable anomalous magnetization. Hence, magnetization with opposite sign from discrete samples of the working half can appear in pass-through measurements. During Leg 172 (Sites 1056–1059; Keigwin, Rio, Acton, et al., 1998), the model magnetization of archive-half samples was calculated from the predicted inclination, assuming simple shear by vertical drag with a core liner as a function of log distance from the center, and the model magnetization was successfully matched with the observed inclination. Thus, in addition to a steep positive, low coercivity component, which may be acquired as isothermal remanent magnetization (IRM), a negative inclination, high coercivity component can be acquired during drilling by mechanical realignment of magnetic grains.

The declinations of archive-half sections are almost always about 320°; this does not agree with those for discrete samples (e.g., Figs. 17E, F). Inclinations do agree with each other after removing the steep positive overprint. The phenomenon that the magnetization measured on archive-half sections is close to "core-north" was observed during Legs 154, 159, 161 (Shipboard Scientific Party, 1995, 1996b, 1996a). In those cases, the phenomenon was explained as a vector sum of radially concentric remagnetization of whole cores that was called "pervasive radial remagnetization" (PRR). In light of such observations, archive APC-half sections show declination close to core-north (zero), and XCB sections tend to be offset several tens of degrees. This can be explained in terms of circular drag by rotation of the core liner relative to the sediment during the coring process.

Magnetostratigraphy

Magnetic polarity was determined by measuring magnetic inclination of archive-half samples after AF demagnetization at 20 mT (Table 25). This was supported by an AF demagnetization experiment on discrete cube samples (Table 24). Paleomagnetic results are plotted for Holes 1071A and 1071B from 0 to 70 mbsf (Fig. 18), and for Hole 1071C from 50 to 260 mbsf (Fig. 19). The polarity is normal both in Holes 1071B and 1071C from the seafloor to about 61.5 mbsf, with significant gaps caused by poor core recovery. Magnetization intensities after demagnetization are generally high, spanning 10–100 mA/m. Magnetic polarity changes from normal to reverse downhole at 61.5 mbsf in Hole 1071B and 61.4 mbsf in Hole 1071C. Combined with the biostratigraphic constraints (calcareous nannofossils) that 174A-1071B-5X-CC (65.69 mbsf) and 1071C-2X-CC (64.42 mbsf) are <0.9 Ma (see "Biostratigraphy" section, this chapter), it can be concluded that this reversal is the boundary between Chrons C1n (Brunhes Chron) and C1r.1r (Matuyama Chron), dated at 0.78 Ma.

Magnetostratigraphic interpretation below 65.7 mbsf is difficult, because the recovery is poor. However, magnetic polarity is normal below 67.8 mbsf (Cores 174A-1071B-6X and 1071C-3X). There should be a boundary between Chrons C1r.1r and C1r.1n (Jaramillo termination; 0.99 Ma) within the core break between 65.7 and 67.8 mbsf (between Cores 174A-1071B-5X and 6X, and Cores 174A-1071C-3X and 4X). This is supported by the biostratigraphic constraints (see "Biostratigraphy" section, this chapter) that 174A-1071B-5X-CC (65.69 mbsf) and 1071C-2X-CC (64.42 mbsf) are <0.9 Ma (calcareous nannofossils), and 1071C-8X-CC is >1.4 Ma (dinocysts). A short normal polarity zone between 67.8 and 68.4 mbsf (Cores 174A-1071B-6X and 1071C-3X) may correspond to Chron C1r.1n (0.99–1.07 Ma). However, it is difficult to correlate normal polarity zones at 96.77–96.79 mbsf (Sample 174A-1071C-6X-1, 57–59 cm), 114.9–116.4 mbsf (Section 174A-1071C-8X-1), and 124.5–129.1 mbsf (Section 174A-1071C-9X-1) to polarity chrons.

Recovery is fairly good for Cores 174A-1071C-11X through 16X (134.4–175.4 mbsf), where sediments are silt or clay (Subunit IIA;

Table 24. Paleomagnetic and rock magnetic parameters of discrete samples for Site 1071.

Core, section, interval (cm)	Depth (mbsf)	NRM Intensity (A/m)	Declination	NRM at 20 mT Inclination	Intensity (A/m)	MDF (mT)	Susceptibility (SI)	K_{arm} (SI)
174A-1071A-								
2H-1, 59-61	5.69	5.30E-01	167.5	37.9	1.51E-01	8	5.81E-04	5.82E-03
2H-2, 59-61	7.19	6.42E-01	123.1	49.2	2.13E-01	5	9.16E-04	4.57E-03
3H-1, 59-61	8.49	1.29E-01	34.5	59.1	5.01E-02	10	9.73E-04	5.79E-03
3H-2, 59-61	9.99	5.97E-01	62.1	48.0	1.95E-01	7	9.31E-04	3.77E-03
3H-3, 57-59	11.47	3.19E-01	86.3	47.5	5.41E-02	4	6.34E-04	3.79E-03
4H-1, 57-59	12.57	5.30E-01	34.1	68.0	1.46E-01	7	7.11E-04	4.86E-03
4H-2, 57-59	14.07	5.10E-01	42.3	56.0	1.38E-01	6	9.01E-04	4.09E-03
4H-3, 57-59	15.57	5.56E-01	46.7	38.5	2.45E-01	15	8.51E-04	4.49E-03
5H-1, 58-60	16.78	2.06E-01	57.9	62.1	2.32E-02	4	6.51E-04	1.77E-03
6H-1, 59-61	26.29	7.17E-02	-125.1	49.3	2.54E-02	6	2.42E-04	2.92E-04
10X-1, 18-20	49.48	3.10E-01	117.0	66.9	1.26E-01		1.06E-03	1.05E-04
174A-1071B-								
2X-1, 93-95	40.73	1.22E-01	120.6	79.3	4.22E-02	10	8.24E-04	2.98E-03
2X-2, 14-16	41.44	1.31E-01	144.2	63.8	6.69E-02	20	5.78E-04	2.60E-03
3X-1, 11-13	49.31	3.42E-01	107.5	70.3	1.55E-01	18	1.38E-03	7.13E-03
4X-1, 3-5	52.93	3.70E-01	97.9	76.4	1.83E-01	20	1.49E-03	6.87E-03
5X-1, 59-61	58.99	9.30E-02	43.0	68.1	3.90E-02	14	7.93E-04	4.99E-03
5X-2, 59-61	60.49	6.37E-02	142.0	77.5	2.62E-02	13	5.88E-04	1.96E-03
5X-3, 59-61	61.99	1.20E-02	211.3	-24.2	2.91E-03	3	3.50E-04	6.90E-04
5X-4, 59-61	63.49	1.67E-02	302.5	-25.3	2.13E-03	3	3.57E-04	5.94E-04
5X-5, 59-61	64.99	3.79E-02	66.0	-35.6	2.63E-03	3	8.20E-04	7.87E-04
174A-1071C-								
2X-1, 59-61	58.99	1.35E-01	223.2	57.6	7.23E-02	21	7.39E-04	4.79E-03
2X-2, 59-61	60.49	5.63E-02	138.1	77.6	2.67E-02	18	5.19E-04	1.89E-03
2X-3, 60-62	62.00	1.03E-02	165.4	-34.7	2.27E-03	3	3.64E-04	5.88E-04
2X-4, 59-61	63.49	2.97E-02	218.2	-52.4	3.54E-03	3	7.05E-04	7.69E-04
3X-CC, 8-10	68.34	6.11E-02	191.3	53.3	1.79E-02	9	4.91E-04	2.21E-03
6X-1, 57-59	96.77	2.60E-02	174.5	64.9	4.22E-03	5	3.69E-04	1.35E-03
8X-1, 72-74	115.62	6.17E-02	143.7	60.4	1.74E-02	8	5.55E-04	
9X-1, 55-57	125.05	3.99E-02	201.9	43.5	6.57E-03	5	4.32E-04	1.81E-03
9X-2, 59-61	126.59	3.50E-02	148.8	50.7	9.46E-03	7	4.08E-04	1.65E-03
9X-3, 59-61	128.09	4.33E-02	186.7	53.4	9.79E-03	7	4.95E-04	2.95E-03
11X-1, 57-59	144.07	2.71E-01	113.3	64.4	1.73E-01	30	7.89E-04	8.36E-03
11X-2, 57-59	145.57	1.13E-01	126.3	75.1	6.22E-02	22	4.84E-04	3.95E-03
11X-3, 59-61	147.09	1.63E-01	118.1	68.5	9.70E-02	28	5.95E-04	3.68E-03
11X-4, 59-61	148.59	1.59E-01	136.0	63.3	9.87E-02	31	6.69E-04	5.21E-03
12X-1, 57-59	149.07	1.53E-01	115.2	68.3	9.90E-02	34	8.49E-04	6.17E-03
12X-2, 54-56	150.54	1.87E-01	138.8	77.5	1.28E-01	34	7.20E-04	6.98E-03
12X-3, 57-59	152.07	2.34E-01	103.3	57.9	1.66E-01	36	9.72E-04	1.01E-02
12X-CC, 12-14	153.32	1.53E-01	245.8	64.4	1.15E-01	38	8.19E-04	6.69E-03
13X-1, 59-61	153.49	1.30E-01	243.1	15.5	5.95E-02	16	4.77E-04	7.10E-03
13X-2, 59-61	154.99	1.77E-02	261.2	22.6	6.73E-03	10	1.55E-04	1.32E-03
13X-3, 59-61	156.49	5.76E-03	175.9	62.7	2.47E-03	15	1.07E-04	4.55E-04
14X-1, 56-58	158.46	1.78E-02	145.7	52.9	1.06E-02	27	1.65E-04	1.35E-03
14X-2, 16-18	159.56	1.76E-02	354.7	72.2	1.17E-02	31	1.91E-04	1.33E-03
14X-3, 123-125	162.13	6.02E-03	157.2	57.8	2.67E-03	16	9.32E-05	6.84E-04
15X-1, 54-56	162.94	2.82E-02	130.2	58.8	2.10E-02	34	1.69E-04	1.09E-03
15X-2, 59-61	164.49	2.65E-02	118.9	68.8	1.81E-02	39	4.04E-04	2.55E-03
15X-3, 59-61	165.99	5.58E-02	41.9	72.2	3.84E-02	39	4.85E-04	4.22E-03
15X-4, 59-61	167.49	5.27E-01	131.0	69.3	2.85E-01	23	2.20E-03	1.93E-02
15X-5, 59-61	168.99	6.65E-02	142.5	69.0	4.05E-02	30	4.61E-04	4.07E-03
15X-6, 58-60	170.48	1.13E-02	275.8	80.1	4.18E-03	13	2.64E-04	1.88E-03
16X-1, 57-59	172.37	4.60E-03	95.2	58.4	9.66E-04	8	1.16E-04	8.02E-04
16X-2, 56-58	173.86	1.13E-02	222.3	80.4	6.50E-03	27	1.54E-04	6.48E-04
19X-1, 59-61	200.69	1.30E-03	331.2	74.7	5.87E-04	16	1.04E-04	9.57E-05
20X-1, 60-62	210.10	1.06E-03	302.0	40.7	3.83E-04	8	5.37E-05	8.98E-05
20X-2, 59-61	211.59	1.01E-03	242.6	41.2	3.10E-04	5	6.49E-05	1.22E-04
20X-3, 59-61	213.09	1.18E-03	117.5	65.6	3.33E-04	8	7.43E-05	9.64E-05
22X-1, 62-64	229.02	5.62E-04	39.5	25.0	2.53E-04	3	3.24E-05	8.10E-05
22X-2, 24-26	230.14	4.20E-04	253.4	32.1	3.04E-04	7	3.24E-05	1.03E-04
23X-1, 59-61	238.29	5.85E-04	0.6	62.9	4.04E-04	4	3.51E-05	8.46E-05
24X-1, 59-61	247.59	9.70E-04	123.4	66.6	4.21E-04	8	5.00E-05	9.06E-05
25X-2, 60-62	253.70	1.72E-03	108.8	65.0	3.71E-04	8	7.84E-05	
25X-3, 59-61	255.19	2.72E-03	114.3	55.5	1.02E-03	15	1.19E-04	2.19E-04
25X-4, 41-43	256.51	1.34E-03	357.0	42.5	3.86E-04	13	2.78E-04	2.23E-04
26X-1, 8-10	256.48	7.76E-04	8.9	0.7	6.15E-04	58	3.79E-05	0.00E+00
174A-1071D-								
6R-1, 59-61	48.29	1.33E-01	90.2	73.6	8.18E-02	27	1.15E-03	6.84E-03
8R-1, 59-61	62.99	1.34E-03	9.3	-51.0	1.38E-03	58	2.58E-04	5.11E-04
174A-1071F-								
1R-1, 59-61	252.59	5.35E-04	336.8	6.6	6.83E-05	4	4.86E-05	1.00E-04
1R-2, 56-58	254.06	5.58E-04	249.8	76.6	5.94E-04	0	4.46E-05	1.06E-04
1R-3, 9-11	254.49	5.57E-04	353.8	79.7	3.39E-04	22	5.27E-05	1.14E-04
6R-1, 114-116	321.34	2.38E-04	177.0	-19.0	2.14E-04	10	4.59E-05	1.10E-04
7R-1, 58-60	330.18	2.09E-04	80.9	33.5	1.47E-04	13	4.05E-05	8.53E-05
7R-2, 51-53	331.11	2.89E-04	44.0	-44.6	2.61E-04	0	7.84E-05	1.04E-04
8R-1, 63-65	339.63	9.87E-05	270.1	-12.3	1.24E-04	0	6.08E-05	9.26E-05
9R-3, 123-125	351.39	2.50E-04	199.2	49.1	4.98E-04	0	4.59E-05	7.99E-05
10R-2, 102-104	360.42	1.73E-03	351.0	25.2	1.15E-03	29	1.03E-04	6.07E-04
10R-3, 95-97	361.85	4.37E-04	284.2	-36.0	1.07E-03	0	1.47E-04	6.09E-04
11R-1, 29-31	367.69	2.30E-04	249.8	-44.6	3.74E-04	0	9.05E-05	1.20E-04
16R-CC, 11-13	414.91	4.19E-04	203.8	74.6	2.39E-04	24	7.50E-05	7.36E-05

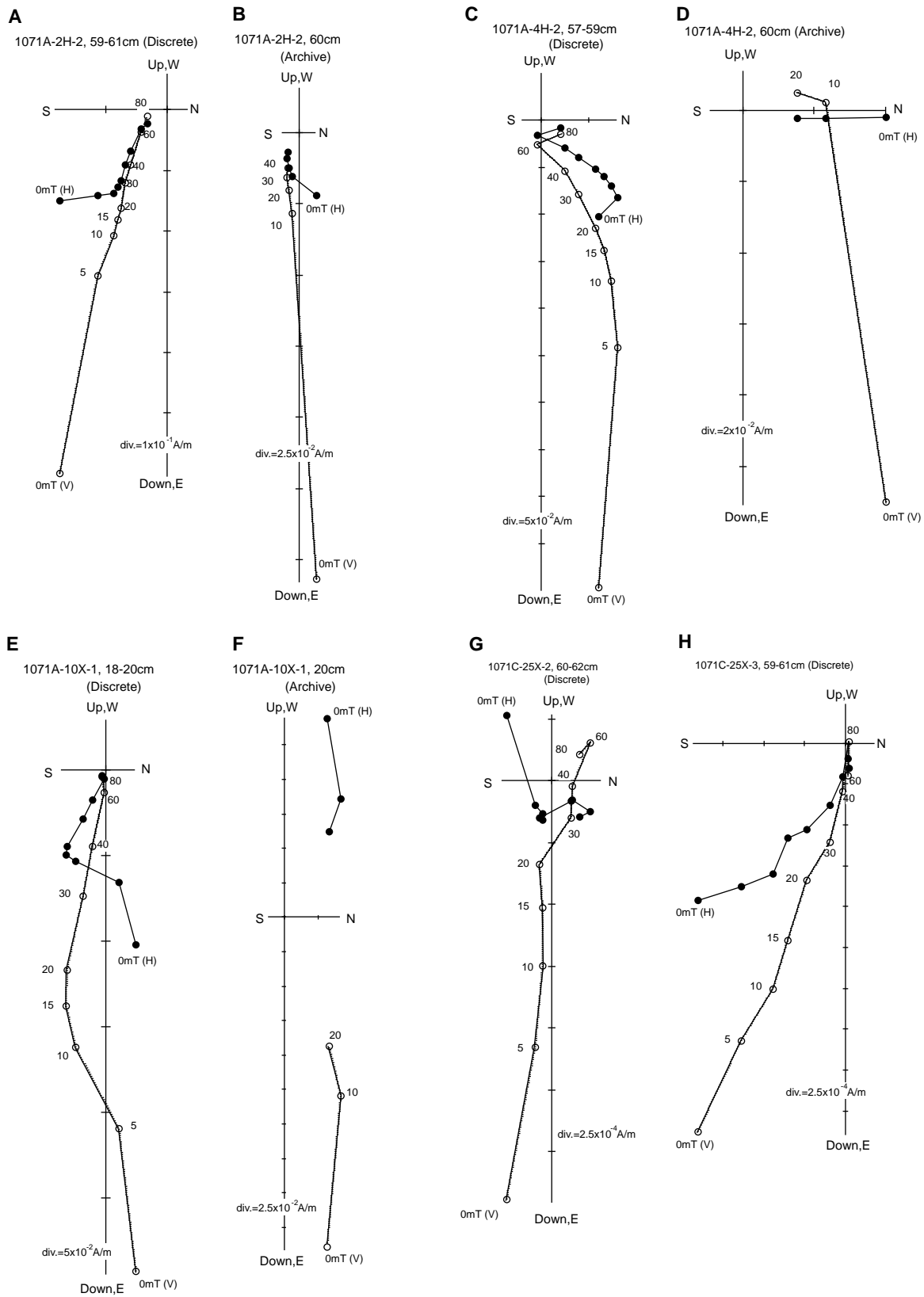Note: MDF = median destructive field, K_{arm} = susceptibility of ARM.

A

1071A-2H-2, 59-61cm (Discrete)

B

1071A-2H-2, 60cm
(Archive)

C

1071A-4H-2, 57-59cm
(Discrete)

D

1071A-4H-2, 60cm (Archive)

E

1071A-10X-1, 18-20cm
(Discrete)

F

1071A-10X-1, 20cm
(Archive)

G

1071C-25X-2, 60-62cm
(Discrete)

H

1071C-25X-3, 59-61cm (Discrete)

Figure 17. Typical examples of vector endpoint diagrams for discrete samples (**A**, **C**, **E**, **G**, and **H**) and archive-half sections (**B**, **D**, and **F**) from Holes 1071A and 1071C. Solid circles and open circles represent projections of magnetization vectors onto a horizontal plane and a vertical plane, respectively. Numbers denote demagnetization levels in milliteslas (mT).

Table 25. Polarity chrons identified for Site 1071.

Hole	Depth (mbsf)	Polarity	Polarity chron	Age (Ma)
1071B	0.0-61.5	N	C1n–Brunhes	0.0-0.78
	61.5-65.5	R	C1r.1r	0.78-(0.99)
	67.8-68.2	N	C1r.1n?	
1071C	0.0-61.3	N	C1n–Brunhes	0.0-0.78
	61.3-61.4	R	C1r.1r	0.78-(0.99)
	67.8-68.4	N	C1r.1n?	
	96.8	N	?	
	114.9-116.4	N	?	
	124.5-129.1	N	?	
	134.4-175.4	N	C3An / C4n-C3Bn?	
	200-257	?		

Note: N = normal, R = reversed, ? = uncertain.
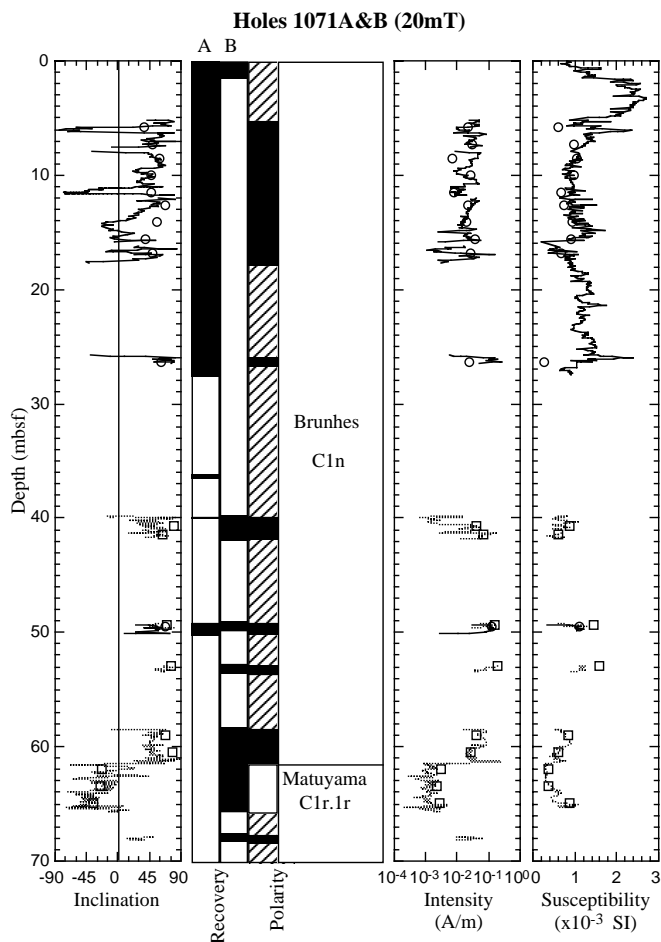
Holes 1071A&B (20mT)

Figure 18. Inclination, magnetic polarity zones, magnetization intensity, and volume magnetic susceptibility for Holes 1071A and 1071B. Inclination and intensity of magnetization are after 20-mT AF demagnetization. Solid lines and open circles indicate pass-through data and discrete data for Hole 1071A, respectively. Dotted lines and open squares denote pass-through data and discrete data for Hole 1071B, respectively. In the polarity column, black = normal polarity, white = reversed polarity, and cross-hatched = uninterpretable.

see "Lithostratigraphy" section, this chapter). The magnetization intensity is high and stable in Subunit IIA, especially for the finer grained part. Magnetic polarity for Subunit IIA is normal throughout and can be correlated with Chron C3An (5.89–6.57 Ma) or a composite sequence between C3Bn and C4n (6.94–8.07 Ma), according to the biostratigraphic constraint that Sample 174A-1071C-14X-CC (163.11 mbsf) is 5.9–7.4 Ma (dinocysts).
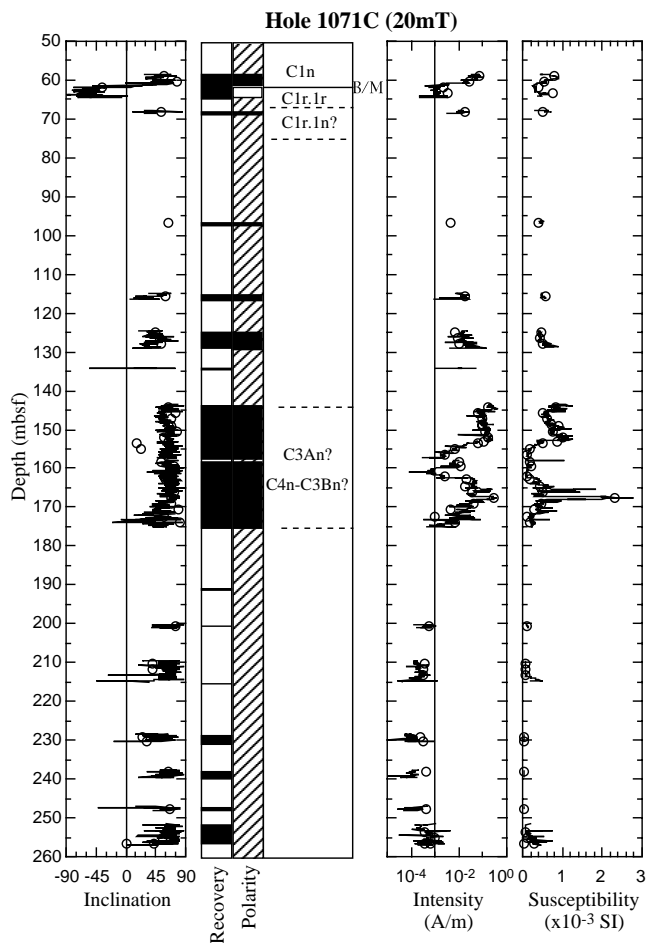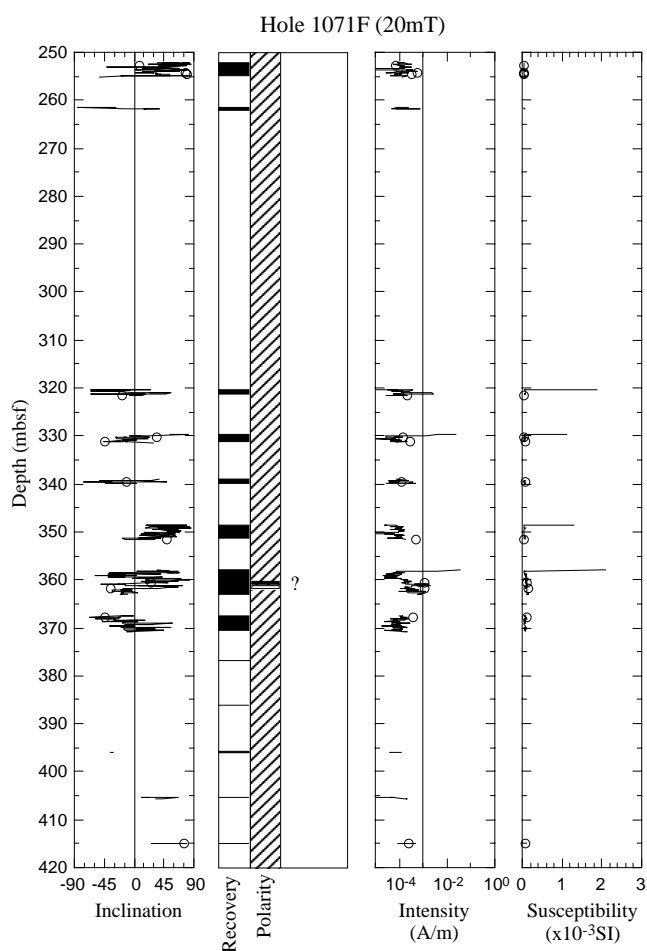
Hole 1071C (20mT)

Figure 19. Inclination, magnetic polarity zones, magnetization intensity, and volume magnetic susceptibility for the B/M interval for Hole 1071C. Inclination and intensity of magnetization are after 20-mT AF demagnetization. Solid lines and open circles indicate pass-through data and discrete data, respectively. In the polarity column, black = normal polarity, white = reversed polarity, and cross-hatched = uninterpretable.

Because the magnetization intensity is low and unstable below 200 mbsf for Hole 1071C, where sediments are silty or muddy sand, it is difficult to identify the polarity of the magnetic field. Following the cut-off value used on Leg 150 (Shipboard Scientific Party, 1994a), the paleomagnetic data where magnetization intensity is <1 mA/m after 20-mT demagnetization are regarded as uninterpretable. Figure 20 shows the paleomagnetic results from Hole 1071F. Following the cut-off process, only two discrete samples remain reliable. One (Sample 174A-1071F-10R-2, 102–104 cm) is normal polarity, and the other (Sample 174A-1071F-10R-3, 95–97 cm) is reversed polarity. Because of poor recovery, unstable magnetization, and poor age constraints (see "Biostratigraphy" section, this chapter), no magnetic polarity chron was determined for Hole 1071F.

Brunhes/Matuyama Boundary

Measurements were made at intervals of 5 mm on Sections 174A-1071B-5X-2 through 5X-5, and Sections 174A-1071C-2X-2 through 2X-4 at demagnetization steps of 20 mT and 30 mT, because Cores 174A-1071B-5X and 174A-1071C-2X were less disturbed (i.e., no observable "biscuiting" except at the boundary between sand and clay/silt layers). Figure 21 shows enlarged plots of inclination and intensity of magnetization after 20-mT AF demagnetization, and magnetic susceptibility spanning the Brunhes/Matuyama (B/M) polarity

transition for Holes 1071B (Fig. 21A) and 1071C (Fig. 21B). These results clearly indicate that the B/M boundary is at 61.5 mbsf for Hole 1071B (10 cm from the top of Section 174A-1071B-5X-3) and between 61.3 and 61.4 mbsf (at the boundary between Section 174A-1071C-2X-2 and Section 174A-1071C-2X-3) for Hole 1071C. The base of a sand layer is at the very top of Section 174A-1071B-5X-3, which is 10 cm above the polarity boundary. In contrast, at Hole 1071C the sand layer sits at 60.9 mbsf, which is 40–50 cm above the polarity boundary (see "Lithostratigraphy" section, this chapter).

Figure 21C shows the results of deconvolution (small solid circles with horizontal bars) on Section 174A-1071B-5X-3 after 20-mT AF demagnetization, along with the pass-through data before deconvolution (dotted lines). The deconvolution was conducted successfully by the ABIC-minimization method (Oda and Shibuya, 1996), and the results show ~3 cm maximum spatial resolution. The direction of magnetization after deconvolution shows that the B/M polarity reversal at 61.4–61.5 mbsf shows somewhat fluctuating features in both declination and inclination. Although there is a possibility that this feature was introduced by drilling disturbance, this may be close to the real geomagnetic fluctuation, as there is no clear evidence of disturbance on the cutting surface of the section. There is also a marked increase in intensity of magnetization from 61.5 to 61.4 mbsf (top of the section).

To confirm whether the polarity reversal is real and whether the silty clay layer beneath the sand layer recorded the B/M polarity reversal, vector endpoint diagrams are plotted for several samples (Fig. 22). Discrete Sample 174A-1071C-2X-1, 59–61 cm (58.99 mbsf; Fig. 22A), shows stable positive inclination through AF demagnetization, whereas Sample 174A-1071C-2X-4, 59–61 cm (63.49 mbsf; Fig. 22C), shows stable negative inclination. These measurements indicate that the polarity reversal is real. In addition, Figure 22B shows the results of demagnetization of pass-through measurement for archive Section 174A-1071C-2X-4 at 100 cm (61.1 mbsf), which is 20 cm below the sand layer previously mentioned. The diagram shows very stable positive inclination toward the origin, indicating normal polarity. The difference in thickness between the B/M transition and the base of the sand layer in Holes 1071B and 1071C suggests that the thickness of the silty clay layer left after erosion at the two holes is different. Although there is a possibility that the silty clay layer was remagnetized during erosion and deposition of the sand layer above, the top of the silty clay layer seems to have experienced the B/M polarity transition. Detailed paleomagnetic and rock magnetic shore-based measurements on discrete samples are needed.

Demagnetization Behavior at Higher Fields

Some discrete samples, especially the samples from Subunit IIA, showed spurious magnetization at demagnetization steps >60 mT. In an attempt to reveal the source of this feature and to get true magnetic polarity of the samples, AF demagnetization experiments up to 200 mT were conducted on selected samples using the DTECH demagnetizer. The demagnetization, both in the demagnetizer, which is in line with the 2G cryogenic magnetometer, and in the DTECH demagnetizer, was performed in X-, Y-, and Z-axis directions, successively. Figure 23 shows the results of some examples. These plots demonstrate that anomalous horizontal magnetizations were acquired after demagnetization at >60 mT. The curves are continuous through switching from the 2G demagnetizer to the DTECH demagnetizer. The directions are not consistent from sample to sample, but seem to be predominantly horizontal. These features were also found during Leg 161 (Shipboard Scientific Party, 1996d) using the previous cryogenic magnetometer; they were considered to be spurious ARM acquired along either the X or –X directions.

Figure 23 shows that the spurious magnetization is neither in the X (–X) nor in the Y (–Y) directions, but in an intermediate direction. A combination of the magnetic grains with higher coercivity aligned parallel to bedding planes and the residual magnetic field (which changes somewhat randomly as the ship's heading changes) in the

Figure 20. Inclination, magnetic polarity zones, magnetization intensity, and volume magnetic susceptibility for the B/M interval for Hole 1071F. Inclination and intensity of magnetization are after 20-mT AF demagnetization. Solid lines and open circles indicate pass-through data and discrete data, respectively. In the polarity column, black = normal polarity, white = reversed polarity, and cross-hatched = uninterpretable.

demagnetizers could explain the different horizontal direction from sample to sample. However, it still remains a mystery as to why each sample has acquired so steady a magnetization in one direction.

Rock Magnetism

Anhysteretic remanent magnetization (ARM) was imparted with a DTECH demagnetizer at an AC field of 80 mT and DC field of 0.1 mT. ARM intensity was expressed as a susceptibility of ARM (K_{ARM}) for normalization, divided by the strength of the biasing DC field. K_{ARM} was divided by volume magnetic susceptibility (K) to show the relative abundance of smaller grain-size fraction of magnetic minerals. Median destructive field (MDF) of NRMs was also calculated from decay curves of NRM during stepwise AF demagnetization, which is a rough analog of coercivity (inverse to magnetic grain size), except that it is sometimes overprinted by drilling-induced magnetization. The measured and calculated rock magnetic parameters are plotted (Fig. 24) with relative peak intensity of pyrite and siderite determined by XRD analysis (see "Lithostratigraphy" section, this chapter).

The primary magnetic mineral is assumed to be magnetite, based on the rock magnetic results from Leg 150 sediments (Urbat, 1996). Above 61.5 mbsf (Unit I), NRM intensity is 7–200 mA/m, K_{ARM} is 1 × 10^{-3} to 1 × 10^{-2} SI, and K is around 10^{-3}, indicating a high concen-

A **Hole 1071B (20mT)**
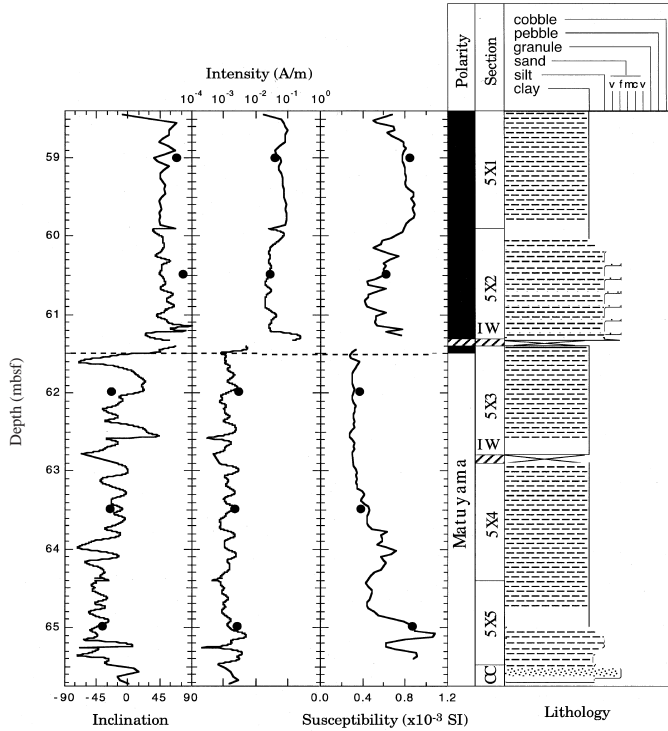
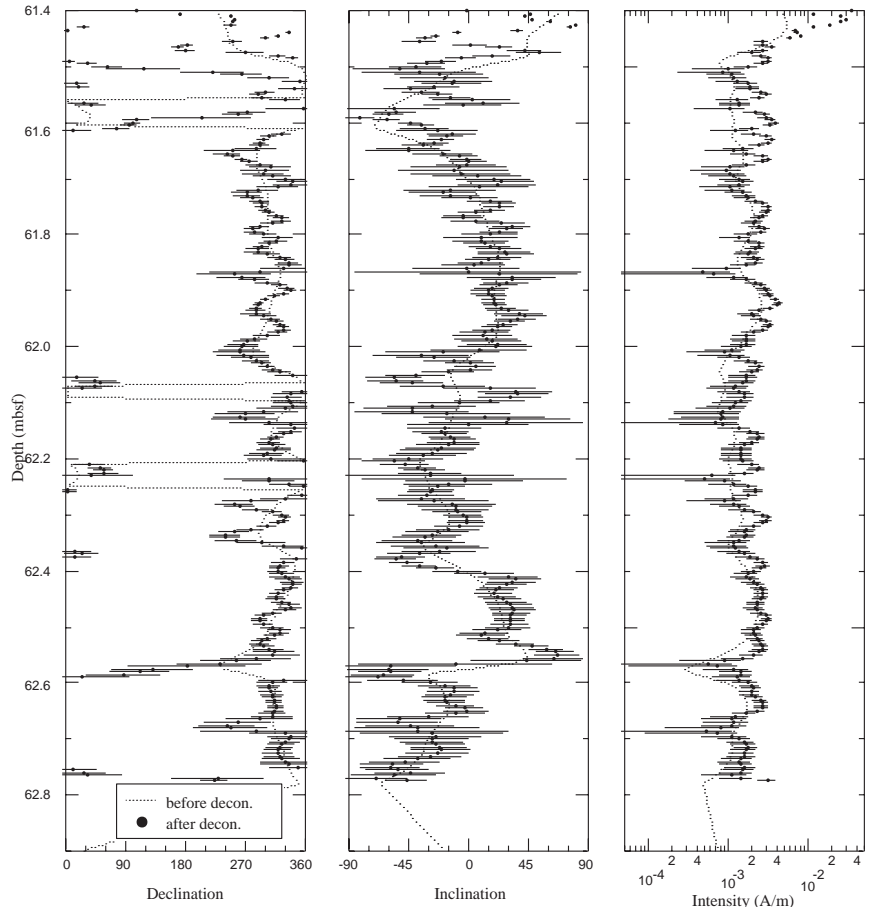**B** **Hole 1071C (20mT)**
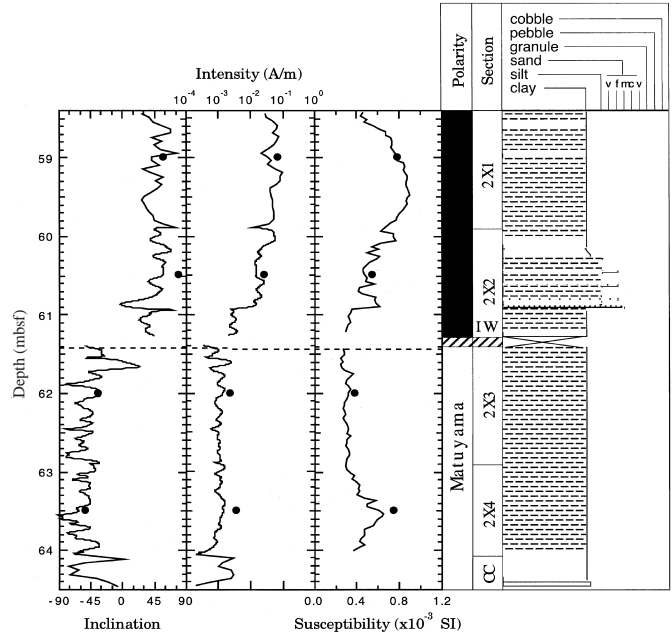
C **Hole 1071B (20mT)**

Figure 21. Inclination and intensity after AF demagnetization, and magnetic susceptibility at 20 mT are plotted vs. depth for the B/M polarity boundary of Holes 1071B (**A**) and 1071C (**B**). Solid lines show pass-through data and solid circles represent discrete data, respectively. Polarity column, section numbers, and simplified lithology are on the right side of both plots. Cross-hatched zones indicate the measurement gap where whole-round interstitial water (IW) samples were taken. **C.** Declination, inclination, and intensity of magnetization for Section 174A-1071B-5X-3 at 20 mT AF demagnetization before (dotted lines) and after (small solid circles with horizontal bars) deconvolution. The length of the horizontal bars represents 95% confidence limits. The bottom 12 cm is missing because of interstitial water sampling.

tration of magnetic minerals in this interval. NRM intensity is relatively low (<10 mA/m) below 61.5 mbsf down to 130 mbsf (Subunit IC). K_{ARM} and K are slightly low for this interval, ranging from 5×10^{-4} to 3×10^{-3}, and from 4×10^{-4} to 6×10^{-4}. K_{ARM}/K is <5 mT, and MDF is <10 mT, indicating larger magnetic grain size (multi-domain magnetite is dominant). This is consistent with the coarse-grained lithofacies of Subunit IC (see "Lithostratigraphy" section, this chapter).
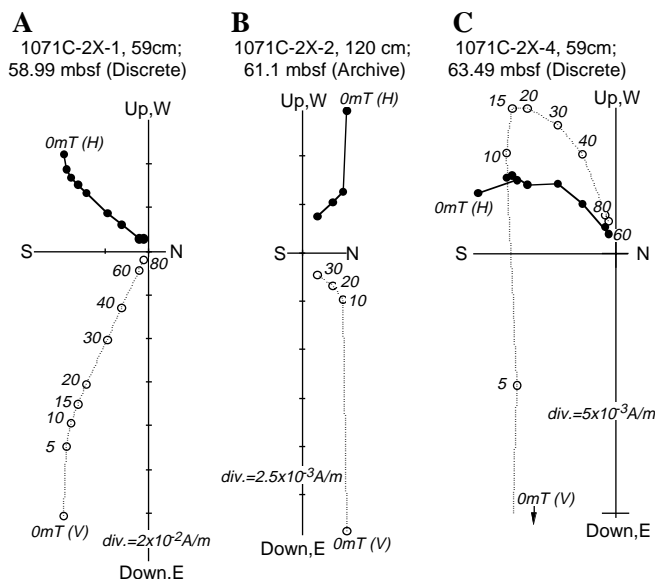
Between 143 and 175 mbsf (Subunit IIA), NRM intensities are 1–300 mA/m, and the upper part is especially high. K_{ARM} and K are also high for this interval, ranging from 10^{-3} to 10^{-2} and from 10^{-4} to 10^{-3}. These indicate high concentrations of magnetic minerals. For this interval, K_{ARM}/K is 5–10, and MDF is 10–40. MDF is higher in the upper part of this interval, indicating the relative abundance of small-grain magnetic particles (single-domain magnetite). This is consistent with the clayey or silty lithofacies of this interval. Below 200 mbsf down to the bottom of the hole (Subunit IIB and IIC), NRM, K_{ARM}, and K are low, indicating low magnetic mineral concentration. K_{ARM}/K is <3, and MDF is <10, except at the bottom of the hole, demonstrating the dominance of larger grain size, multi-domain magnetite. The larger magnetic grain size is consistent with the coarse lithofacies.

Considering the above, Unit I contains a large amount of magnetic minerals, with fluctuation of grain size related to lithofacies. Subunit IIA shows evidence of high concentrations of magnetic minerals and a relative abundance of small magnetic grains. The grain size of the sediment may have controlled the magnetic grain size parameters (K_{ARM}/K, MDF). Although the dissolution of primary magnetite and formation of secondary magnetite may have occurred after deposition, some fraction of magnetic minerals recording primary magnetic polarity may have survived. The remarkable lowering of all magnetic concentration parameters in Subunits IIB and IIC compared with Subunit IC may indicate that extensive magnetite dissolution has occurred in these intervals.

INORGANIC GEOCHEMISTRY

Thirty-three whole-round samples were taken from Holes 1071A (four samples), 1071B (four samples), 1071C (11 samples), 1071D (6 samples), and 1071F (8 samples) for routine interstitial water (IW) analyses. Concentrations of HPO_4^{2-} were determined twice, with in-

Figure 22. Vector endpoint diagrams for discrete samples (**A, C**) and an archive-half sample (**B**) of Core 174A-1071C-2X across the presumed B/M polarity transition.
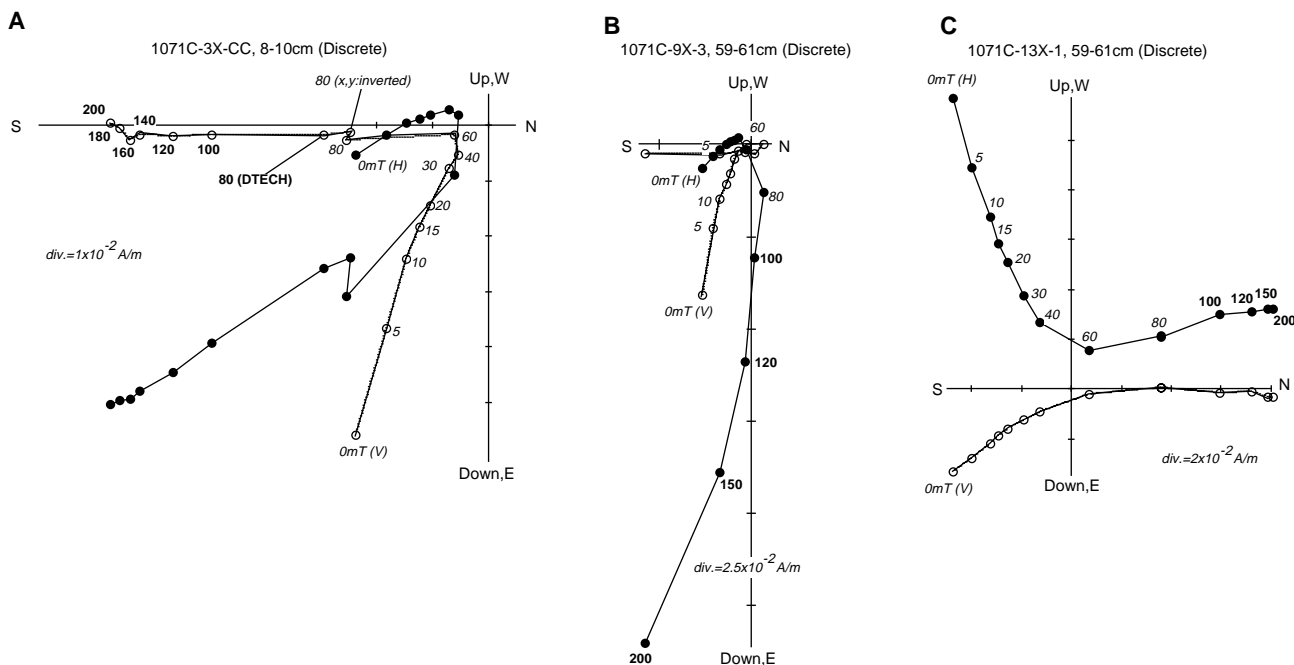
Figure 23. Vector endpoint diagrams for discrete samples showing spurious magnetizations at higher demagnetization fields. AF demagnetizations up to 80 mT were conducted on 2G demagnetizer and from 80 to 200 mT were done on DTECH demagnetizer. "80" denotes the data point measured with the 2G demagnetizer; the data point labeled "80 (x, y:inverted)" indicates measurements were made after demagnetization of 80 mT using a 2G cryogenic magnetometer with x and y axes inverted (rotated along z axis). The data point labeled "80 (DTECH)" denotes measurements were made after demagnetization at 80 mT on the DTECH demagnetizer. Because these three points agree very well, it is unlikely that only the direction of the residual magnetic field controls the direction of these anomalous magnetizations (maybe ARM).
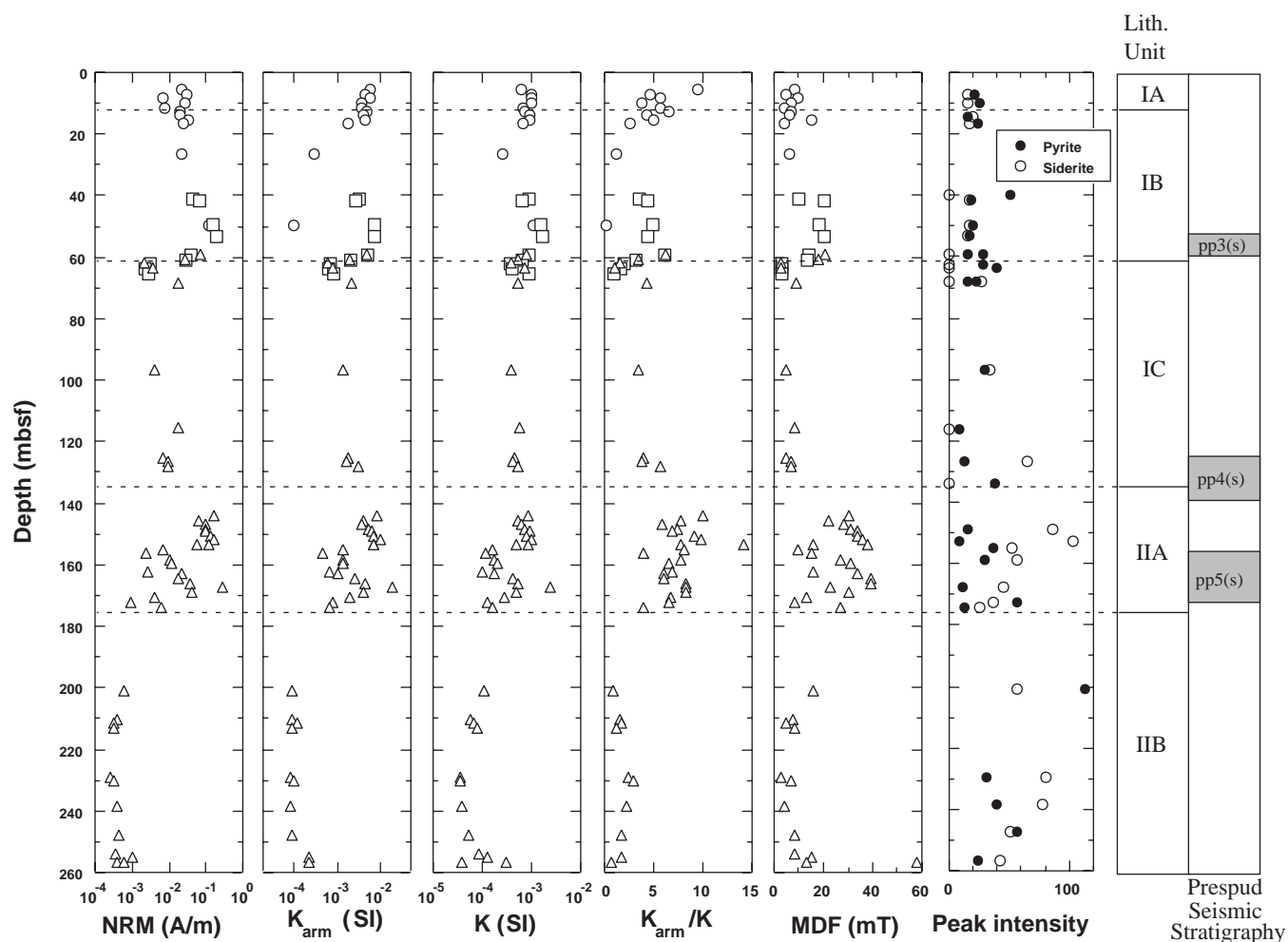
Figure 24. Rock magnetic properties plotted vs. depth for Holes 1071A, 1071B, and 1071C. Natural remanent magnetization (NRM) after 20-mT demagnetization, ARM susceptibility (K_{ARM}), susceptibility (K), K_{ARM}/K, and median destructive field (MDF) are plotted from left to right. Open circles, open rectangles, and open triangles represent data points of discrete cube samples from Holes 1071A, 1071B, and 1071C, respectively. Relative peak intensities of pyrite and siderite identified from XRD analysis are also plotted at right. Lithostratigraphic units within the prespud seismic stratigraphic framework (see Table 40 and "Lithostratigraphy" and "Seismic Stratigraphy" sections, this chapter) are plotted at far right.

dependent replicates (including standards) to evaluate overall precision of analyses. Average deviation between HPO_4^{2-} analyses was 0.2 µm.

Operations at Site 1071 were highlighted by a spectacular fountain of water that flowed from the drill pipe at pressure upon reaching a depth of ~250 mbsf (Fig. 25). Three additional water samples were collected at Site 1071 to understand the origin of this fountain. A water sample was collected from the fountain in a bucket ~10 min after initiation of fountain flow. This water contained significant quantities of coarse to pebbly sand. After filtering, the water was analyzed for all species except pH and alkalinity. Two samples of surface seawater then were collected in a bucket near the bow of the *JOIDES Resolution* and filtered through a 45-µm filter. One sample was collected in the morning and analyzed for salinity and dissolved species; the other was collected in the afternoon and analyzed for salinity only.

Results

The International Association for the Physical Sciences of the Ocean (IAPSO) standard has concentrations of dissolved species approximately equivalent to "average" seawater. Surface seawater at Site 1071 has a salinity, measured by refractive index, of 32, ~90%

of IAPSO (34.99). Major ions (Cl^-, SO_4^{2-}, K^+, Ca^{2+}, Mg^{2+}) in surface seawater range between 87% and 90% of IAPSO concentrations (Table 26).

Salinity, concentrations of major ions, and Sr^{2+} decrease with depth in an uppermost zone (6.55–26.45 mbsf) and appear to lie on diffusional gradients between IAPSO and subsurface minima at ~30 mbsf (Table 26; Fig. 26). Gradients are significantly different for various dissolved species. Chloride (Cl^-) decreases by 23% to 431 mM, Sr^{2+} by 48% to 45 µM, Mg^{2+} by 47% to 28.52 mM, K^+ by 60% to 4.21 mM, Ca^{2+} by 70% to 3.13 mM, and SO_4^{2-} by 79% to 6.17 mM. In contrast to the above ions, alkalinity, NH_4^+, and HPO_4^{2-} increase to local maxima of 8.36 mM, 1.18 mM, and 12.0 µM, respectively, in the upper 30 m of pore-water freshening.

Salinity and concentrations of major ions and Sr^{2+} increase with depth between 30 mbsf and a depth approximately equivalent to the lithologic Subunit IB/IC boundary at 61.4 mbsf (Table 26; Fig. 26). Relative increases occur on the same order as concentration decreases in overlying pore water. Chloride increases to 456 mM (82% of IAPSO), Sr^{2+} to 56 µM (64%), Mg^{2+} to 34.96 mM (65%), K^+ to 5.51 mM (53%), Ca^{2+} to 5.56 mM (53%), and SO_4^{2-} to 14.05 mM (49%). Alkalinity, NH_4^+, and HPO_4^{2-} are relatively low between 30 and 61.4 mbsf.

Figure 25. A fountain of water gushing from the drill pipe at the rig floor at Site 1071. Initial fountain height was estimated at half the height of the derrick (~30 m). Note the significant quantity of sand deposited on the rig floor by the fountain.

Between 61.4 mbsf and a depth approximately equivalent to the lithologic Unit I/II boundary (~150 mbsf), concentrations of all species are relatively constant except Cl^-, Sr^{2+}, and K^+ (Table 26; Fig. 26). Chloride increases to 515 mM (92% of IAPSO), Sr^{2+} to 66 µM (76%), and K^+ to 8.32 mM (80%). Concentrations of alkalinity, NH_4^+ and HPO_4^{2-} increase significantly below 150 mbsf; concentrations of H_4SiO_4 increase markedly in lithologic Subunit IIC below 200 mbsf (Table 26; Fig. 26).

Between 200 and 370 mbsf, a second salinity minimum is centered around 300 mbsf, a zone of no recovery. The minimum Cl^- value in this zone is 500 mM, an 11% decrease relative to IAPSO values. Below 300 mbsf, Cl^- increases to values (576 mM) greater than IAPSO (559 mM) at the bottom of the sampled section. Alkalinity and NH_4^+ decrease through the salinity minimum, then increase to maximum values obtained for Site 1071 at 370 mbsf. Sulfate increases slightly through the lower salinity minimum, and then decreases to ~1 mM at 360 mbsf.

The chemistry of fountain water is similar to that of surface seawater (Table 26; Fig. 26). Concentrations of all major ions and Sr^{2+} are within 5% for both waters; concentrations of NH_4^+, HPO_4^{2-}, and H_4SiO_4 are at or near detection limit for both waters. The composition of fountain water is significantly different from that of pore water at depths near the bottom of the drill pipe at ~250 mbsf, where the fountain occurred.

Preliminary Interpretations

Downhole pore-water profiles at Site 1071 (Table 26; Fig. 26) reflect a combination of processes, including diffusion, organic-matter decomposition, carbonate precipitation, and silica dissolution. These processes occur at many ODP sites and are discussed thoroughly in previous *Initial Reports* volumes (e.g., Mountain, Miller, Blum, et al., 1994). However, unlike at most ODP locations, pore-water profiles at Site 1071 are conspicuously out of steady state. In particular, there are (1) shallow salinity minima, and (2) multiple depth zones with relatively high abundance of dissolved species.

Salinity Minima

The shallow salinity minimum is a zone between the seafloor and ~150 mbsf where salinity and Cl^- profiles exhibit decreases to about 70%–80% of IAPSO values (Fig. 26). A second salinity minimum is centered around 300 mbsf where salinity and Cl^- decrease to about 10% of IAPSO values. These minima most likely reflect oscillations in the salinity of overlying water between glacial and interglacial stages of the Pliocene–Pleistocene, particularly over the last 18 k.y. Sea level was ~130 m below that of present day during the last glacial maximum (LGM) at 18 ka. Because Site 1071 is at a water depth of 88–90 mbsl, the top of the sediment column probably was above sea level and received fresh (or brackish) water during the LGM. The subsequent transgression over the last 18 k.y. covered the sediment column with seawater. Dissolved ions then began to diffuse downward from the surface (and upward from more saline pore waters at depth) into relatively fresh interstitial waters at Site 1071. Ionic diffusion continues today, as evidenced by the shallow subsurface Cl^- minima. A somewhat similar explanation was offered for freshwater excursions in uppermost sediments from five Atlantic Margin Coring Project (AMCOR) holes on the New Jersey shelf (Hathaway et al., 1979; Kohout et al., 1988). The fresh-water zone is much thinner with two distinct minima at Site 1071, whereas at the AMCOR sites a broad minimum in salinity had been noted.

Diagenesis

Sulfate reduction of organic matter causes a decrease in SO_4^{2-} concentrations and an increase in titration alkalinity, NH_4^+, and HPO_4^{2-} (e.g., Gieskes, 1983). The upper maximum in alkalinity, NH_4^+, and HPO_4^{2-} at ~30 mbsf is related to SO_4^{2-} reduction. The 79% decrease in pore water SO_4^{2-} at this depth greatly exceeds the amount caused by pore-water freshening discussed above (20%). The maximum in alkalinity, NH_4^+, and PO_4^{3-} centered at ~200 mbsf coincides with an interval of increased sedimentation rates and organic-matter accumulation (see "Biostratigraphy" and "Organic Geochemistry" sections, respectively, this chapter). However, direct evidence for SO_4^{2-} reduction is not obvious because a significant decrease in pore water SO_4^{2-} does not occur in this depth interval. In contrast, the lowermost maximum in alkalinity (~30 mM), HPO_4^{2-}, and NH_4^+ at ~350 mbsf is associated with almost complete sulfate reduction.

Subsurface maxima in organic-matter decomposition products are atypical and suggest different depth zones of bacterial activity. Because the upper maximum is depth coincident with the shallow salinity minimum, pronounced oscillations in salinity over time may affect rates of organic decomposition at different depths. For example, times of freshwater input during subaerial exposure may contribute dissolved O_2 to upper parts of the sediment column and effectively halt SO_4^{2-} reduction. However, similar profiles with multiple peaks of alkalinity, NH_4^+, and HPO_4^{2-} were documented ~50 km away at ODP Site 903 on the upper New Jersey slope (Mountain, Miller, Blum, et al., 1994). Although these maxima also were attributed to local zones of organic-matter degradation (Mountain, Miller, Blum, et al., 1994), the water depth of Site 903 (445 mbsl) precludes an explanation involving subaerial exposure and major salinity fluctuations. Lithologic variations may instead control organic-matter decomposition rates across a wide area.

Organic-matter diagenesis, with attendant decrease in SO_4^{2-} and increase in carbonate alkalinity, promotes precipitation of diagenetic

Table 26. Interstitial water data for Site 1071.

Core, section, interval (cm)	Depth (mbsf)	pH	Alkalinity (mM)	Salinity	Cl⁻ (mM)	SO_4^{2-} (mM)	NH_4^+ (mM)	HPO_4^{2-*} (μM)	Sr^{2+} (μM)	Mg^{2+} (mM)	Ca^{2+} (mM)	K⁺ (mM)	H_4SiO_4 (μM)
174A-1071A-													
2H-1, 145-150	6.55	7.6	NM	32.0	540	20.80	0.58	0.9	NM	46.19	7.50	8.63	160
3H-2, 145-150	10.80	7.4	5.93	28.0	482	13.68	0.62	1.8	66	38.49	4.21	5.82	190
4H-2, 145-150	14.90	7.5	6.89	27.5	465	9.27	1.11	10.7	58	34.15	3.46	4.50	171
6H-1, 75-80	26.45	7.8	8.36	26.0	431	6.17	1.18	12.0	45	28.52	3.13	4.21	218
174A-1071B-													
2X-1, 140-150	41.20	7.8	8.23	26.0	436	9.05	0.58	2.5	49	30.09	4.21	5.30	417
3X-CC, 0-50	49.64	7.5	5.96	27.0	451	12.43	1.18	0.8	52	32.66	4.88	4.80	196
5X-2, 145-150	61.35	7.7	5.66	28.0	456	14.05	1.00	1.5	55	34.96	5.56	5.51	143
5X-3, 140-150	62.80	7.8	6.51	27.0	450	11.88	1.24	3.7	52	32.88	5.07	4.54	252
174A-1071C-													
2X-2, 140-150	61.30	7.9	7.24	27.0	451	12.42	1.04	2.8	56	33.54	5.17	4.63	241
6X-CC, 21-29	97.09	7.9	5.39	28.0	471	10.74	1.33	1.4	56	32.89	5.29	6.35	175
7X-CC, 13-23	105.73	7.8	4.79	28.5	474	11.67	1.22	1.0	59	34.22	5.39	6.50	145
8X-CC, 17-27	116.34	8.1	5.04	28.5	484	6.17	1.12	2.8	59	27.45	5.28	8.12	173
9X-2, 140-150	127.40	7.6	4.76	29.0	495	9.40	1.25	0.6	62	32.52	5.48	7.08	222
12X-2, 140-150	151.40	7.6	8.54	30.5	515	8.28	1.24	0.6	66	34.18	5.70	8.32	273
15X-5, 140-150	169.80	7.5	13.40	31.0	528	12.67	2.23	2.0	69	47.55	8.12	10.24	286
19X-CC, 0-16	201.16	7.5	18.81	31.0	527	9.52	3.03	1.0	NM	37.15	6.90	9.67	288
22X-1, 140-150	229.80	7.3	16.50	31.0	523	11.32	2.73	9.9	68	37.67	7.82	8.68	785
23X-1, 140-150	239.10	7.4	14.88	31.0	515	13.08	2.96	12.1	70	36.69	7.38	8.50	866
25X-2, 140-150	254.50	7.32	13.90	31.0	501	14.36	2.50	3.5	71	39.65	7.25	8.18	740
174A-1071D-													
1R-1, 52-62	0.52	7.72	4.09	31.0	521	18.65	0.76	1.7	77	43.73	6.61	8.00	190
4R-CC, 6-12	28.36	8.04	9.02	25.5	449	6.21	1.28	6.0	53	29.49	3.62	4.63	286
5R-1, 24-30	38.24	7.82	8.04	26.0	441	7.46	1.35	1.7	49	29.37	3.77	4.69	322
6R-1, 97-107	48.67	7.85	7.50	26.0	447	8.29	1.05	0.8	52	30.45	3.89	4.39	300
7R-1, 33-43	57.73	7.81	5.87	26.5	459	11.00	1.62	1.3	53	32.55	4.43	4.16	196
8R-1, 17-27	62.57	7.80	8.23	26.5	456	11.72	1.50	1.7	56	33.13	4.44	4.55	203
174A-1071F-													
1R-1, 140-150	253.40	7.31	14.79	31.0	518	12.46	3.01	19.3	74	39.10	7.95	8.51	778
2R-1, 39-45	261.79	7.30	12.54	31.0	500	16.54	2.57	10.5	74	41.04	9.05	7.46	646
6R-1, 118-128	321.38	7.25	22.44	32.0	531	7.68	3.27	23.8	69	39.67	7.60	8.15	568
7R-1, 90-100	330.50	7.79	21.34	32.5	544	6.42	3.46	NM	68	38.43	6.64	8.26	756
8R-1, 0-10	339.00	7.28	22.20	33.0	551	4.09	3.40	23.6	NM	38.37	7.11	7.98	905
9R-2, 74-86	350.04	7.32	27.64	34.0	570	1.19	4.19	NM	70	38.84	6.68	8.34	884
10R-3, 140-150	362.30	7.63	27.84	34.0	575	1.07	4.21	30.2	68	38.89	6.80	8.29	867
11R-2, 58-68	369.48	7.88	26.92	34.0	576	2.12	4.41	22.8	67	38.53	6.56	8.46	905
Fountain		NM	NM	32.0	505	25.59	0.00	0.2	79	48.66	9.56	9.48	10
SSW	NA	NM	NM	32.0#	497	25.96	0.00	0.2	75	47.99	9.14	9.20	9
IAPSO†	NA	NA	NA	35.0	559	28.90	NA	NA	87	54.00	10.55	10.44	NA

Notes: * = average of two independent runs. NM = not measured. # = two samples. SSW = surface seawater. IAPSO = International Association for the Physical Sciences of the Ocean. NA = not applicable. † = reported values (from Gieskes et al., 1991).

carbonates (e.g., Baker and Burns, 1985; Compton, 1988). At the depth of the shallow alkalinity maximum, X-ray diffraction analyses document the presence of dolomite (see "Lithostratigraphy" section, this chapter). Dolomite precipitation is consistent with a decrease in Mg^{2+} and Ca^{2+} in excess of that predicted by pore-water freshening, as well as by relatively high Mg^{2+}/Ca^{2+} values in pore water (~2× seawater). Dolomite and siderite also are present in sediment at the depth of the lower alkalinity maximum (see "Lithostratigraphy" section, this chapter).

Elevated concentrations of dissolved silica (H_4SiO_4) typically reflect an interval of relatively abundant opaline silica (opal-A). An increase in opal-CT abundance occurs at the depth of high dissolved silica concentrations (see "Lithostratigraphy" section, this chapter).

Fountain Origin

The unexpected fountain at Site 1071 (Fig. 25) was of immediate operational concern: pressurized water flowing up the drill pipe prevented core recovery and presented a potential safety hazard. Consequently, there was a concerted effort to understand the origin of the fountain. Two general explanations were forwarded: (1) direct drilling into an overpressurized aquifer, and (2) backflushing of seawater pumped down the annulus from the surface. The latter explanation can be understood by considering that surface seawater is pumped down the hole at pressure (greater than hydrostatic) during drilling. Chemical similarity of fountain water and surface seawater strongly indicates that the fountain was caused by backflushing. A plausible

scenario is that porous sand intervals were charged with pressurized water when the unstable walls of the overlying hole caved in on and packed off the drill string (see "Lithostratigraphy" and "Operations" sections, this chapter). Pressurized water then returned up the drill pipe to the rig floor when the ROP slowed at ~250 mbsf.

ORGANIC GEOCHEMISTRY

Shipboard organic geochemical studies of cores from Holes 1071A–1071F included monitoring of hydrocarbon gases, carbonate carbon and organic carbon contents, total sulfur and nitrogen contents, and Rock-Eval pyrolysis assays on selected samples. The procedures are summarized in the "Explanatory Notes" chapter (this volume).

Volatile Gases from Sediments

All cores recovered from Holes 1071A through 1071D and 1071F were monitored for presence of gaseous hydrocarbons by the headspace gas technique. No significant amounts of hydrocarbons above background (5–10 ppmv) were detected, except at the bottom of Hole 1071F. The four cores recovered and sampled at the bottom of Hole 1071F (Cores 174A-1071F-11R-2, 13R-CC, 14R-CC, and 15R-1) had headspace methane contents of 488, 840, 1268, and 651 ppmv, respectively. This depth interval (369–405 mbsf) of increased methane content corresponds with the minimum in dissolved sulfate con-
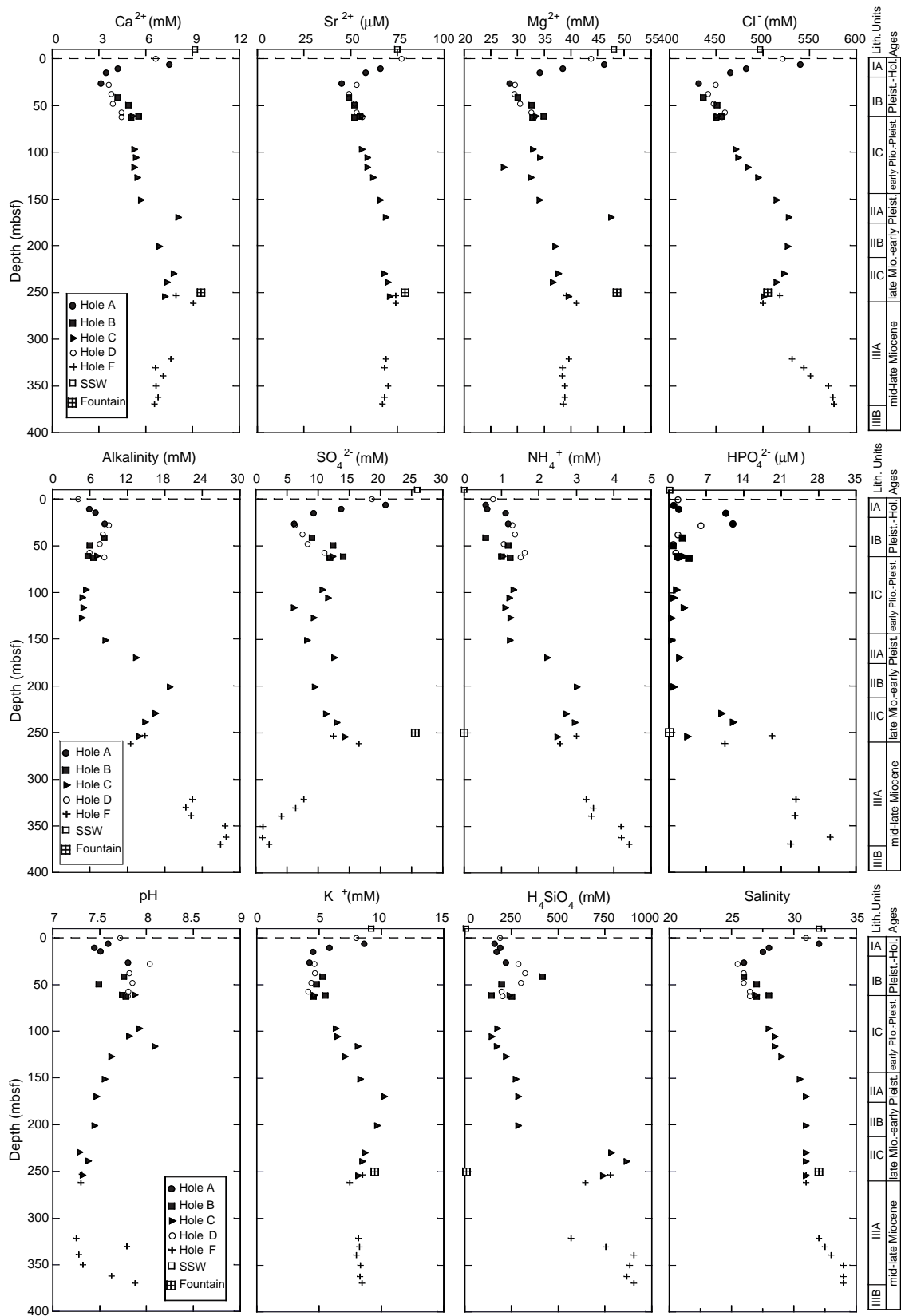
Figure 26. Concentration-depth profiles of interstitial water at Site 1071 with approximate lithostratigraphic boundaries (see "Lithostratigraphy" section, this chapter). Dashed lines at 0 mbsf represent the seafloor. Open squares that are plotted arbitrarily above the dashed lines represent analyses of surface seawater. Apparent overlap in ages reflects biostratigraphic uncertainty. "Early Pliocene–Pleistocene" and "Holocene" assigned ages are in question.

centration for Site 1071. The C_1/C_2 value ranges from 1302 to 2440 over this same depth interval, which is fairly typical for Miocene-age sediments at temperatures of 25°–30°C.

Carbon and Elemental Analyses

Results of carbonate carbon, total carbon (TC), total organic carbon (TOC; by difference), total nitrogen (TN), and total sulfur (TS) analyses on selected sediment samples from Site 1071 are given in Table 27. Organic and carbonate carbon contents are plotted against depth of burial in Figure 27. Carbonate carbon contents are somewhat higher (1–2 wt%) in Pliocene–Pleistocene shelf sediments at burial depths of <134 mbsf, and lower (0.1–0.3 wt%) in the deeper sampled intervals down to 405 mbsf. An exception is the sample at 358 mbsf, which has carbonate carbon contents of 4.91 wt%.

Organic carbon varies inversely with carbonate carbon in samples from Site 1071. Where carbonate carbon is higher than organic carbon in Pliocene–Pleistocene sediments (0–135 mbsf), the reverse is generally true in the deeper sections cored (135–405 mbsf). Organic carbon content increases with depth, with samples from 0 to 135 mbsf having lower organic carbon contents (avg. C_{org} = 0.31 wt%) than those from 149 to 405 mbsf (avg. C_{org} = 0.65 wt%, with lignite-appearing interval excluded).

Nitrogen and sulfur contents are reported but have not been critically interpreted. Nitrogen is generally proportional to organic carbon, with C/N values ranging from 8 to 12. The lignite-appearing interval is exceptional in having C/N values up to 40. Some samples in Hole 1071C have unusually high sulfur contents (4 wt% in Section 2X-3, 8.2 wt% in Section 13X-2), possibly reflecting localized occurrence of iron sulfides (see "Lithostratigraphy" section, this chapter).

Organic-Matter Characterization

Twenty-two samples from Site 1071 were characterized by Rock-Eval pyrolysis, with the results given in Table 28. Samples with >0.5 wt% organic carbon were selected for analysis, and a shallow sample having less organic carbon was selected for stratigraphic coverage. There is a trend of increasing S_2 yield and hydrogen index (HI) with increasing depth of burial. This increased pyrolysis yield with depth may be caused by changes in the primary nature of the organic matter, or it may reflect some reorganization or "diagenetic stabilization" of the organic matter.

There is also a tendency for Rock-Eval oxygen index (OI) values to decrease with increasing depth at Site 1071. Because the Rock-Eval S_3 yields are proportional to carbonate carbon contents, this trend of decreasing OI could be an artifact of thermally unstable car-

Table 27. Carbon and elemental analyses for sediment samples from Site 1071.

Core, section, interval (cm)	Depth (mbsf)	IC (wt%)	CaCO₃ (wt%)	TC (wt%)	OC (wt%)	TN (wt%)	TS (wt%)
174A-1071A-							
2H-2, 62-63	7.22	1.34	11.17	1.65	0.31	0.039	0.13
3H-2, 62-63	10.03	1.93	16.06	2.15	0.23	0.053	0.21
4H-2, 63-64	14.13	1.27	10.61	1.59	0.32	0.057	0.26
5H-1, 63-64	16.83	1.69	14.06	2.07	0.38	0.065	0.53
10X-1, 10-11	49.40	1.49	12.43	1.75	0.25	0.053	0.14
174A-1071B-							
2X-1, 26-27	40.06	0.47	3.87	0.78	0.32	0.045	0.97
2X-1, 42-43	41.72	1.42	11.79	1.62	0.21	0.047	0.27
4X-1, 36-37	53.26	1.33	11.07	1.76	0.43	0.048	0.20
5X-1, 88-89	59.26	1.18	9.81	1.47	0.30	0.054	0.44
5X-4, 65-66	63.55	1.08	9.00	1.49	0.41	0.049	0.16
174A-1071C-							
2X-1, 89-90	59.29	1.05	8.78	1.37	0.32	0.055	0.20
2X-3, 89-90	62.29	1.56	13.01	1.88	0.32	0.05	3.96
3X-CC, 4-5	68.30	0.14	1.17	0.54	0.40	0.029	0.08
6X-CC, 4-5	96.94	0.32	2.70	0.87	0.55	0.049	0.86
8X-1, 115-116	116.05	0.22	1.82	0.38	0.16	0.019	0.07
9X-1, 122-123	125.72	2.66	22.11	2.85	0.19	0.041	0.58
10X-CC, 6-7	134.06	0.03	0.22	0.23	0.20	0.04	0.44
11X-4, 56-57	148.56	0.34	2.84	0.95	0.60	0.061	0.24
12X-3, 91-92	152.41	0.50	4.20	1.02	0.52	0.075	0.16
13X-2, 64-65	155.04	0.16	1.35	0.66	0.50	0.062	8.23
14X-1, 89-90	158.79	0.25	2.04	0.64	0.40	0.044	0.74
15X-4, 86-87	167.76	0.27	2.23	1.51	1.25	0.092	0.60
16X-1, 63-64	172.43	0.21	1.78	1.07	0.86	0.07	1.30
16X-2, 85-86	174.15	1.18	9.86	1.51	0.32	0.039	0.86
19X-1, 65-66	200.75	0.16	1.33	0.52	0.36	0.047	1.04
22X-1, 96-97	229.36	0.10	0.80	0.67	0.57	0.054	1.76
23X-1, 80-81	238.50	0.07	0.57	0.67	0.60	0.054	1.54
24X-1, 46-47	247.46	0.06	0.49	0.59	0.53	0.046	1.39
25X-4, 52-53	256.62	0.21	1.73	0.43	0.22	0.052	2.00
174A-1071D-							
1R-1, 34-35	0.34	1.40	11.66	1.64	0.24	0.038	0.09
5R-1, 15-16	38.15	2.64	21.98	2.91	0.27	0.038	0.06
6R-1, 49-50	48.19	1.46	12.15	1.70	0.25	0.059	0.08
7R-1, 14-15	57.54	1.33	11.05	1.62	0.30	0.056	0.09
8R-1, 54-55	62.94	1.24	10.31	1.64	0.40	0.038	0.50
174A-1071F-							
1R-2, 27-28	253.77	0.11	0.89	0.83	0.72	0.061	1.40
2R-1, 11-12	261.51	0.17	1.45	7.88	7.71	0.224	4.49
2R-1, 16-17	261.56	0.03	0.21	2.59	2.56	0.136	1.33
2R-1, 23-24	261.63	0.06	0.53	18.00	17.93	0.416	14.92
2R-1, 26-27	261.66	0.01	0.06	2.33	2.32	0.119	1.56
6R-1, 43-44	320.63	0.32	2.70	1.03	0.70	0.049	0.87
7R-1, 35-36	329.95	0.18	1.54	0.99	0.80	0.059	0.83
8R-1, 47-48	339.47	0.16	1.31	1.02	0.87	0.063	0.76
9R-3, 84-85	351.00	0.19	1.54	0.87	0.68	0.052	0.69
10R-1, 0-2	357.90	4.91	40.88	5.64	0.74	0.037	1.47
10R-1, 48-49	358.38	0.24	1.99	0.79	0.55	0.051	1.02
10R-1, 117-118	359.07	0.13	1.04	0.88	0.76	0.067	0.35
15R-1, 28-30	405.48	0.08	0.67	1.08	1.00	0.109	0.75

Note: IC = inorganic carbon, CaCO₃ = calcium carbonate, TC = total carbon, OC = organic carbon, TN = total nitrogen, and TS = total sulfur.
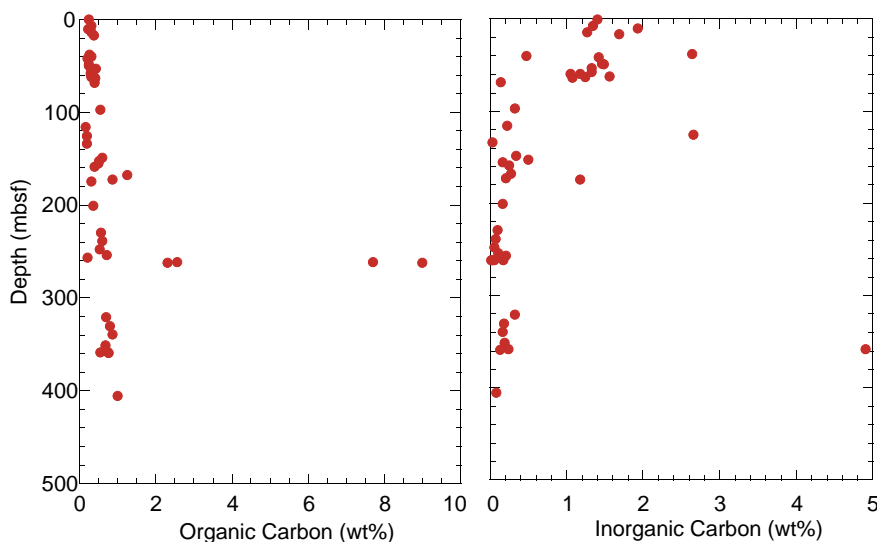

Figure 27. Organic carbon and carbonate carbon content vs. depth for sediment samples from Site 1071.

bonates in the sediments at shallower depths, and thus be unrelated to organic-matter composition.

PHYSICAL PROPERTIES

Introduction

Physical properties data collected at Site 1071 are based on measurements and procedures discussed in the "Explanatory Notes" chapter (this volume). In this section, we present results of physical properties measurements and discuss trends in the data and correlations between physical properties and other shipboard measurements at Site 1071. Data acquired at this site are included in Tables 29–39 (on CD-ROM, back pocket, this volume).

Density and Porosity

Density measurements were acquired at a variety of resolutions; results are presented in Figures 28 and 29. For Holes 1071A–1071F, we used the gamma-ray attenuation porosity evaluator (GRAPE) component of the MST to estimate whole-core density at a sample spacing of 4 cm (Table 29 on CD-ROM). For cores recovered from Hole 1071A, index properties samples were taken from alternating sections; for Holes 1071B, 1071C, 1071D, and 1071F, index properties samples were taken at a nominal spacing of 75 cm (two samples per section). Index properties samples were used to calculate wet, dry, and grain density; water content; porosity; and void ratio (Figs. 28, 29; Table 30 on CD-ROM).

Wet bulk density data in Holes 1071A–1071D (Fig. 28) show several small-scale trends, as well as a gradual overall increase, consistent with effects of compaction. The greatest downhole increase in density appears in the upper 10 m of Hole 1071A. Smaller scale trends in density in Holes 1071A–1071D (Fig. 28) include an interval of downward-decreasing density (~59–65 mbsf) near sequence boundary pp3(s), as well as four distinct intervals of downward-increasing density at ~125–130 mbsf (near pp4[s]), 168–174 mbsf (across pp5[s]), 210–215 mbsf, and 250–255 mbsf, at the base of the recovered section, near m0.5(s) (see "Seismic Stratigraphy" and "Downhole Logging" sections, this chapter). With the possible exception of the ~210–215 mbsf downward-increasing interval, the other small-scale intervals of changing density are approximately coincident with inferred seismic and/or lithologic boundaries (see "Lithostratigraphy" and "Seismic Stratigraphy" sections, this chapter). These trends are not simply a result of differences in sedimentary sources, as indicated by the fact that grain density (Figs. 28, 29) is nearly constant throughout the recovered interval at Site 1071. The lithified horizon near m0.5(s) that was seen in Hole 1071C at ~256 mbsf (Core 174A-1071C-26R; Fig. 45) was not recovered in Hole 1071F (Fig. 29). Recovery in Hole 1071F was low, and density measurements were correspondingly sparse. Density increases downhole to ~2.6 g/cm^3 at ~415 mbsf in a second lithified layer, just below the inferred position of m1(s) (see "Seismic Stratigraphy" and "Downhole Logging" sections, this chapter).

GRAPE density data were edited for outliers (densities <~1 g/cm^3 were discarded); the most common cause of such outliers was gaps in the cores. GRAPE density estimates from the MST system generally agree with index properties bulk density measurements. In particular, excellent agreement is observed between both values and trends in the two sets of density data for intervals where good core recovery was achieved using APC or XCB (e.g., 0–27.5 and 145–175 mbsf; Fig. 28). This agreement between the two independent measures of density in these intervals validates the GRAPE technique for APC and completely filled XCB cores. In most of the remaining intervals, GRAPE density values are systematically lower than index properties bulk density values, although overall trends in the two data sets are similar (Figs. 28, 29). This suggests that it is possible to apply a simple correction to the GRAPE data to account for the lower volume in incompletely filled intervals. One possible procedure could make

Table 28. Organic carbon and Rock-Eval pyrolysis on selected samples from Site 1071.

Core, section, interval (cm)	Depth (mbsf)	OC (wt%)	S$_1$ (mg/g)	S$_2$ (mg/g)	S$_3$ (mg/g)	HI (mg/gC)	OI (mg/gC)	T$_{max}$ (°C)
174A-1071B-								
4X-1, 36-37	53.26	0.43	0.03	0.02	0.47	5	109	399
174A-1071C-								
6X-CC, 6-7	96.94	0.55	0.07	0.30	0.70	55	127	387
12X-3, 91-92	152.41	0.52	0.06	0.90	2.66	173	512	543
13X-2, 64-65	155.04	0.50	0.08	0.73	0.33	146	66	536
15X-4, 86-87	167.76	1.25	0.09	1.36	3.23	109	258	426
16X-1, 63-64	172.43	0.86	0.09	1.26	1.62	147	188	425
22X-1, 96-97	229.36	0.57	0.10	0.90	0.39	158	68	419
23X-1, 80-81	238.50	0.60	0.11	1.15	0.35	192	58	420
24X-1, 46.47	247.46	0.53	0.09	1.26	0.25	238	47	421
174A-1071F-								
1R-2, 27-28	253.77	0.72	0.11	1.90	0.22	263	30	419
2R-1, 11-12	261.51	7.71	0.62	11.94	3.85	154	49	417
2R-1, 16-17	261.56	2.56	0.33	4.01	0.94	156	36	423
2R-1, 23-24	261.63	17.93	0.70	12.56	7.25	70	40	378
2R-1, 26-27	261.66	2.32	0.31	4.09	1.08	176	46	426
6R-1, 43-44	320.63	0.70	0.10	1.46	0.98	208	140	418
7R-1, 35-36	329.95	0.80	0.04	1.01	0.80	126	100	423
8R-1, 47-48	339.47	0.87	0.09	1.40	0.81	160	93	422
9R-1, 84-85	351.00	0.68	0.08	1.28	0.83	188	122	419
10R-1, 0-2	357.90	0.74	0.02	0.75	1.54	101	208	428
10R-1, 48-49	358.38	0.55	0.06	1.36	0.64	247	116	423
10R-1, 117-118	359.07	0.76	0.26	1.51	1.08	198	142	420
15R-1, 28-30	405.48	1.00	0.07	1.63	0.71	163	71	427

Note: OC = organic carbon, HI = hydrogen index, OI = oxygen index.

use of shipboard core photographs to estimate the percent of filling of cores. However, the index properties density data have a spatial resolution more than adequate to support the development of postcruise seismic impedance functions, and shipboard index properties data should also allow for correlation with pre-existing and shipboard density logging data.

Porosity measurements made on cores from Holes 1071A through 1071D and 1071F (Figs. 28, 29) range from nearly 50% to lows of ~4% for fully lithified samples from 256 mbsf (near m0.5[s]) in Hole 1071C, and ~7% from 415 mbsf in Hole 1071F (below m1[s]; see "Seismic Stratigraphy" and "Downhole Logging" sections, this chapter). Although porosity shows a slight overall decrease downhole, porosity trends do not in general appear to be characteristic of compaction processes. Instead, the data define a series of small-scale trends. For example, the interval from ~50 to 65 mbsf shows downhole-increasing porosity, whereas the interval from ~96 to 175 mbsf is composed of a series of intervals, of varying thickness, of downhole-decreasing porosity (Fig. 28). In Hole 1071F (Fig 29), porosity increases downhole from ~254 to 262 mbsf and peaks at the base of Subunit IIC, before resuming an overall trend of gradual downhole decrease in porosity. The physical evidence provided by the porosity and density data suggests a dynamic, nonsteady-state sedimentary environment during the late Neogene.

Magnetic Susceptibility

Magnetic susceptibility was measured on whole cores at 4-cm intervals using the MST. No correction was made to the data to account for incompletely filled cores, and no filtering was applied to the raw data. Therefore, susceptibility data for Holes 1071A–1071D and 1071F (Figs. 28, 29; Table 31 on CD-ROM) are likely to be useful for interpreting overall trends, but not necessarily for determining specific, precise values, except for the APC-cored interval in Hole 1071A (~0–27 mbsf; Fig. 28). Susceptibility trends are commonly used to infer changes in depositional environment and/or diagenetic changes. In particular, terrigenous influx and accompanying iron content of sediments are related to increases in susceptibility. In Figure 28, the upper ~27 m contains two intervals of downward-increasing susceptibility; the boundary between these intervals is near the boundary between lithostratigraphic Subunits IA and IB (Fig. 28; see "Lithostratigraphy" section, this chapter). Another interval of down-
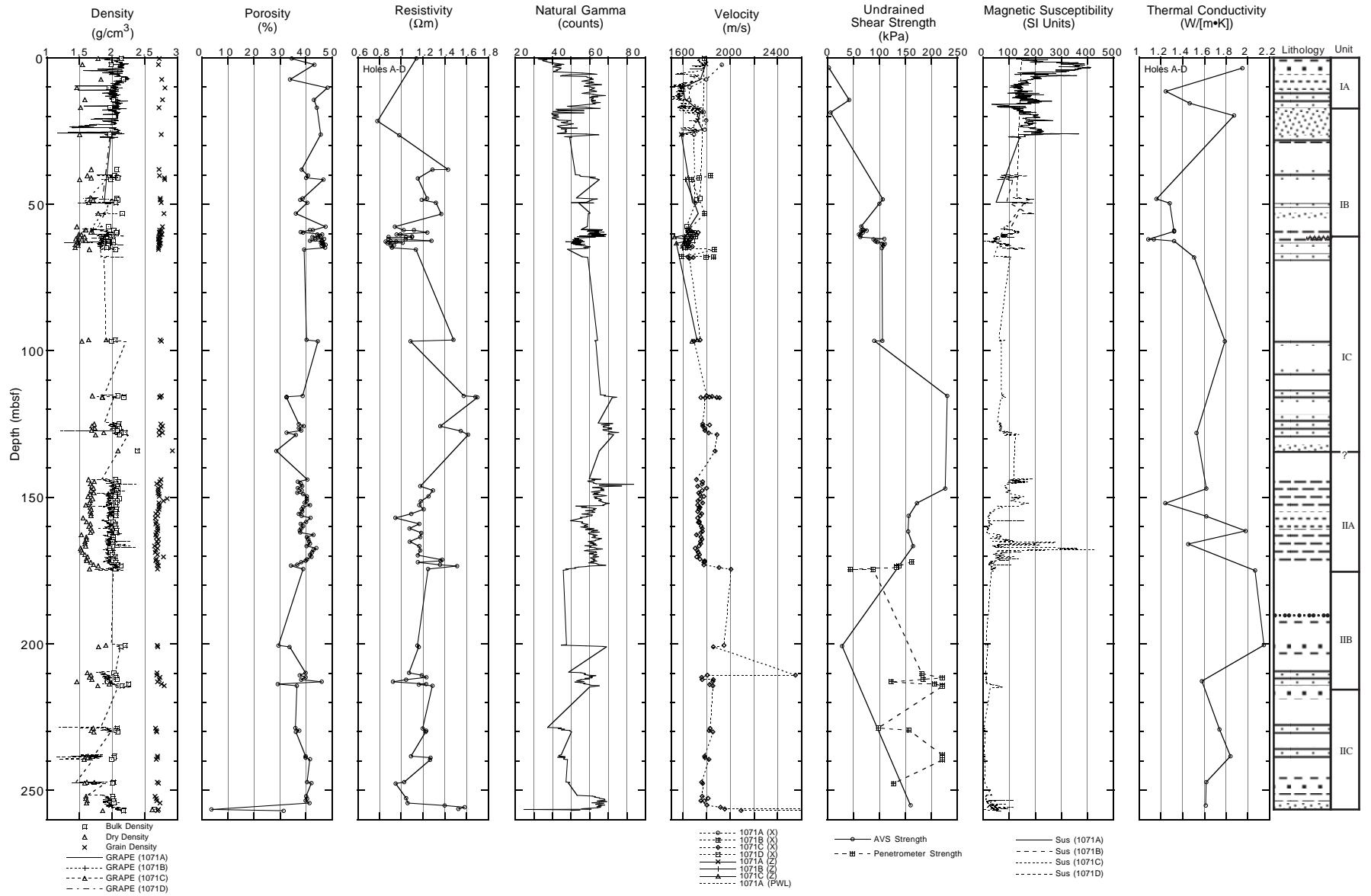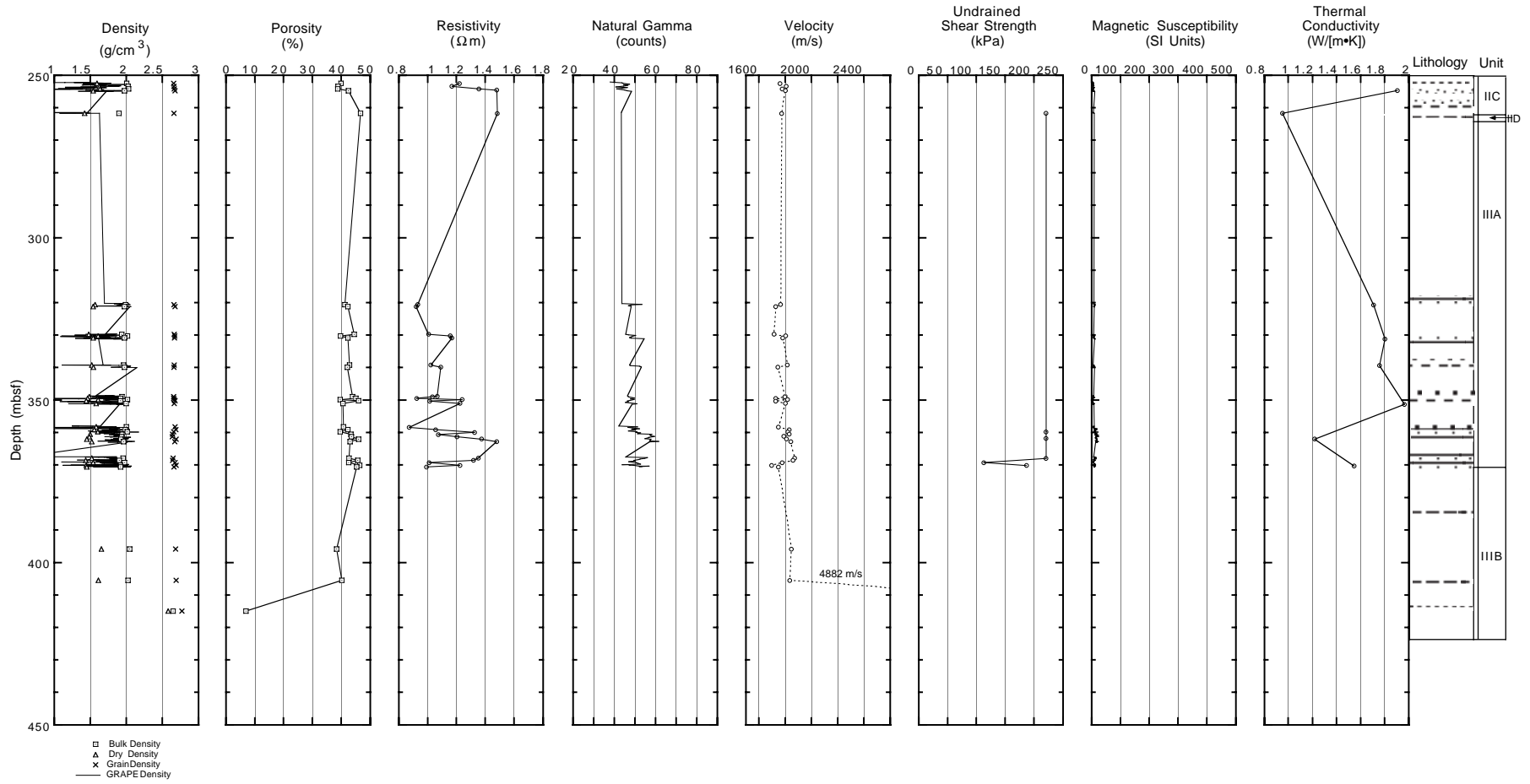
Figure 28. Index properties (IP), multisensor track (MST) GRAPE density, discrete IP porosity, resistivity, natural gamma radiation (for comparison, a partial gamma-ray log from the COST-B2 well is shown in Figure 44), MST- and PWS-derived *P*-wave velocity, undrained shear strength, MST magnetic susceptibility, and thermal conductivity from Holes 1071A–1071D. Physical properties data are plotted along with a simplified lithologic summary; units and lithologic symbols are those used in the "Lithostratigraphy" section (this chapter). *P*-wave velocity measurements used three different measurement techniques and orientations (i.e., the x [PWS3], y [PWL], and z [PWS1] directions) with respect to the cores. These are represented by different symbols in this plot. Note the similarities between velocities obtained using the different measurement techniques and orientations. Shear strength measurements were made using the AVS and hand-held penetrometer. For comparison with the MST magnetic susceptibility measurements, the inferred depth of the B/M boundary (see "Paleomagnetism" section, this chapter) is ~60 mbsf, which is the approximate location of the boundary between lithologic Subunits IB and IC.

Figure 29. Index properties (IP), multisensor track (MST) GRAPE density, discrete IP porosity, resistivity, natural gamma radiation, MST- and PWS-derived *P*-wave velocity, undrained shear strength, MST magnetic susceptibility, and thermal conductivity from Hole 1071F. For comparison with natural gamma radiation measurements, a partial gamma-ray log from the COST-B2 well is shown in Figure 44. All velocities were measured using the PWS3 frame (x-direction). Shear strength measurements were made using the hand-held penetrometer.

ward-increasing susceptibility is located between ~144 and 152 mbsf in lithologic Subunit IIA. Magnetic susceptibilities from Hole 1071F (Fig. 29) are uniformly low. However, recovery was also low, and intervals of higher susceptibility may have been missed.

Magnetic susceptibility is a useful measurement for hole-to-hole correlation, the construction of composite stratigraphic sections at multiple-hole sites, and paleomagnetic studies. Trends and values in susceptibility records from Holes 1071B and 1071C match, suggesting that the overlapping depth ranges of the two holes (~58–65 mbsf; Fig. 28) represent approximately the same stratigraphic interval.

Natural Gamma-ray Emission

Natural gamma-ray (NGR) emission measurements, coupled with discrete resistivity measurements (see below), are important for core-to-log correlation. NGR measurements were made using the MST at 20-cm intervals in each section, with a counting period of 30 s. In general, NGR results (Figs. 28, 29; Table 32 on CD-ROM) reflect sand vs. clay content, with higher counts in clay-rich intervals. For example, downward-increasing NGR counts in the upper 10 m (Fig. 28) correlate with a decrease in sand content. A sharp downhole decrease occurs at the base of lithostratigraphic Subunit IA, where interbedded silt/clay and sand overlie an interval of sand (see "Downhole Logging" section, this chapter, for evidence that the thickness of this sand may have been exaggerated by flow-in), and a downhole decrease of lesser magnitude was observed at the base of Subunit IB (see "Lithostratigraphy" section, this chapter). The upward increase in NGR counts from 160 to 150 mbsf suggests that the interval of silt noted on the lithologic log must fine upward into the overlying clay (see "Lithostratigraphy" section, this chapter). The base of this silt interval also appears gradational, based on the NGR results. A decrease in NGR counts occurs at the bottom of Hole 1071C, where lithified sandstone was encountered (~256 mbsf). NGR trends in Hole 1071F (Fig. 29) are obscured by limited core recovery.

Thermal Conductivity

Thermal conductivity was measured once per core in all holes (Figs. 28, 29; Table 33 on CD-ROM). The wide sampling interval, coupled with low recovery, allows only the most general observations. Values range between 1.13 and 2.15 W/(m·K), with the higher values generally associated with coarser grained intervals.

Compressional Wave Velocity

P-wave velocity is one of the physical properties of primary interest on Leg 174A because of its use in linking coring and logging results to seismic profiles. *P*-wave velocities are used for traveltime-depth conversion and, when coupled with density measurements, production of synthetic seismograms (see "Seismic Stratigraphy" and "Downhole Logging" sections, this chapter).

PWL measurements on whole-round cores were made using the MST only to the base of Core 174A-1071A-5H (25.48 mbsf; Table 34 on CD-ROM). The PWL was then turned off because of incompletely filled core liners. Discrete *P*-wave velocity measurements were made on split-core sections using the PWS1 transducers (parallel to the core axis, z-direction; Table 35 on CD-ROM) and PWS3 frame (orthogonal to core axis, x-direction; Table 36 on CD-ROM). Measurement frequency was the same as that for index properties, two per section after Hole 1071A (~75 cm spacing), with velocity and index properties measurements made at the same core locations. Use of PWS1 was discontinued after Section 174A-1071C-6X-1 (96.68 mbsf) because cracking of sediment during insertion prevented the sound signal from passing between the transducers. Thereafter, all velocity measurements were made with the PWS3 apparatus.

Measured velocities in Holes 1071A–1071D are generally between 1600 and 1800 m/s (Fig. 28). Intervals of uniform, or gradually

varying, velocity predominate. These are separated by short intervals of abrupt downhole increase, notably at ~128 mbsf (near pp4[s]), 174 mbsf (near pp5[s]), 210 mbsf, and 256 mbsf (near m0.5[s]) (see "Seismic Stratigraphy" and "Downhole Logging" sections, this chapter). These depths also lie close to lithologic boundaries (Fig. 28), and all but the 210 mbsf change correspond to intervals in which clay-rich sediments overlie sandier sediments (see "Lithostratigraphy" section, this chapter). The lithified sandstone at the base of Hole 1071C has a *P*-wave velocity of ~5500 m/s. The sandstone appears to be thin; its potential to generate a strong seismic reflection is uncertain, given the vertical resolution of the Oc270 site-survey seismic data.

Measured velocities at Hole 1071F (Fig. 29) in the interval between 0 and 359 mbsf are in the range of 1700–1800 m/s, with scatter and lack of systematic trends a result of poor core recovery in this hole. Most velocities in this interval cluster at ~1800 m/s. Between ~359 and ~370 mbsf, velocities increase downhole from ~1800 to ~1900 m/s; below this, velocities decrease downhole to 1700–1800 m/s. This velocity change at ~370 mbsf corresponds to the boundary between lithostratigraphic Subunits IIIA and IIIB (see Fig. 29 and "Lithostratigraphy" section, this chapter). Below ~370 mbsf, only three velocity measurements were obtained because of poor core recovery; noteworthy among these is a velocity of 4882 m/s taken from an indurated sandstone at ~415 mbsf, below m1(s). Velocity changes at ~370 and ~415 mbsf bracket m1(s) (inferred depth 392 mbsf; see "Seismic Stratigraphy" section, this chapter). It is possible that the observed seismic character of m1(s) is in part the result of acoustic interference between reflections from these two impedance contrasts.

Shear Strength

Undrained shear strength was measured at a variable rate, between one per core and two per section. AVS measurements were made in suitably soft sediments in Holes 1071A–1071D (Fig. 28; Table 37 on CD-ROM), whereas measurements below 170 mbsf (Holes 1071C and 1071F) were primarily made using the penetrometer (Figs. 28, 29; Table 38 on CD-ROM). However, the penetrometer can measure only within the range 0–220 kPa. Shear strengths above this range are plotted at 220 kPa; true shear strengths are higher. Because of low core recovery, data are sparse (Figs. 28, 29), and overall trends should be evaluated with caution. In general, undrained shear strength increases downhole, which is consistent with effects of compaction. In Subunits IA and IB (0–65 mbsf), undrained shear strength increases from 3 to ~100 kPa (Fig. 28). A small but distinct downward increase in strength coincides with the boundary between Subunits IB and IC (~61.4 mbsf), and a similar downward increase was observed above the boundary between Subunits IIB and IIC (~213 mbsf). A downward decrease in strength is coincident with the boundary between Subunits IIA and IIB (~175 mbsf). These trends, therefore, probably reflect depositional processes. Data from Hole 1071F (Fig. 29) are minimal, because the strength of the sediment is generally above the range of the penetrometer (220 kPa).

Electrical Resistivity

Resistivity measurements were acquired with varying resolution. Measurements were made in the longitudinal (z) direction, once per core in Hole 1071A, and once or twice per section in Holes 1071B, 1071C, 1071D, and 1071F. Resistivity values (Figs. 28, 29; Table 39 on CD-ROM) range from ~0.8 to 1.8 Ωm. Because grain density is fairly constant (Figs. 28. 29), changes in resistivity predominantly reflect changes in porosity and pore-water composition (see "Inorganic Geochemistry" section, this chapter).

High porosities near the top of Hole 1071A (Fig. 28) correspond to low resistivities. In general, resistivities increase downhole from 0.8 to 1.8 Ωm in lithostratigraphic Unit I (~0–135 mbsf), except for a well-defined, sharp downhole decrease near the boundary between Subunits IB and IC (sequence boundary pp3[s]; see "Seismic Stratig-

raphy" section, this chapter). In the upper part of Subunit IB (~20–53 mbsf), resistivity increases downhole from ~0.8 to 1.35 Ωm, but this trend is based on a sparse data set. In the clay-rich boundary zone between Subunits IB and IC (~57–66 mbsf), resistivity decreases downhole from 1.2 to 0.8 Ωm, but small variations occur as a result of local changes in porosity (see Fig. 28) and the presence of interbedded fine sand. Core recovery was low in Subunit IC, and the sparse resistivity values vary between 1.0 and 1.8 Ωm. Resistivities decrease slightly downhole in Unit II (~135–255 mbsf). Variations in interstitial water chemistry in this interval could be the explanation for the lack of resistivity response to the downhole increase in porosity at ~200 mbsf (see "Inorganic Geochemistry" section, this chapter). Subunits IIA, IIB, and IIC are generally characterized by values of ~1.15 Ωm. Low core recovery in Subunit IIB resulted in a gap in the measurements except near the bottom of the subunit, where values are generally between 1.0 and 1.2 Ωm, with low values corresponding to higher porosity and clay content. Near the bottom of Subunit IIC, resistivity increases to ~1.6 Ωm as the lithology becomes more silty.

Resistivity increases downhole at the top of Hole 1071F (base of Subunit IIC; Fig. 29), despite the fact that porosity also increases in this interval. This could be related to a Cl⁻ concentration minimum at ~250–300 mbsf (see "Inorganic Geochemistry" section, this chapter). Resistivity is more responsive to porosity changes deeper in Hole 1071F. However, the stiff sediment from cores in Hole 1071F often cracked when the resistivity probes were inserted, and this may also have influenced resistivity values.

Summary

A large number of discontinuities and trends in physical properties measurements coincide with observed lithologic changes and unit boundaries and also with interpreted seismic discontinuities (see "Seismic Stratigraphy" section, this chapter). Several sharp changes in density correlate with changes in velocity that should reinforce each other in the generation of impedance contrasts. Furthermore, the locations of these physical properties changes support the estimated depths to seismic discontinuities. For example, both density and velocity decrease downhole at ~59–65 mbsf (~pp3[s]), and they both increase downhole at ~125–130 mbsf (~pp4[s]), ~168–174 mbsf (~pp5[s]), ~210 mbsf (no correlative seismic boundary), and ~250–256 mbsf (~m0.5[s]). The lithified sandstone at ~256 mbsf has a *P*-wave velocity of ~5500 m/s, but appears to be only a thin layer (<1 m thick at COST-B2; see "Downhole Logging" section, this chapter). Its potential to generate a strong seismic reflection is therefore open to question. The seismic character of sequence boundary m1(s) may in part be the result of acoustic interference between reflections from impedance contrasts associated with bracketing velocity changes at ~370 and ~415 mbsf.

Resistivity appears to respond mainly to porosity. The peak in Cl⁻ concentration at ~175–225 mbsf has little influence on resistivity values, but variations in interstitial water chemistry might be the cause of the lack of resistivity response to the downhole increase in porosity at ~200 mbsf (see "Inorganic Geochemistry" section, this chapter). A Cl⁻ concentration minimum at ~250–300 mbsf corresponds to high resistivities at the top of Hole 1071F (base of Subunit IIC), but cracking on insertion of resistivity probes also occurred in Hole 1071F cores (see "Inorganic Geochemistry" section, this chapter). Physical properties data from Site 1071 provide another basis for correlating cores recovered at Site 1071 with data from the COST-B2 well (see "Downhole Logging" section, this chapter).

SEISMIC STRATIGRAPHY

Introduction

In this section, we summarize regional geophysical information available prior to Leg 174A in the vicinity of Site 1071 (Holes 1071A–1071E, proposed Mid-Atlantic Transect [MAT] site 8B3; Holes 1071F–1071G at a new site not approved precruise, MAT-8B4, the intersection of MAT-8B grid Profiles 801 and 814, see Fig. 30) and detail in a preliminary fashion its use in deciphering the relationships between the sampled section and possible fluctuations of sea level in the late middle Miocene–Pleistocene. One key component is a set of high-resolution multichannel seismic (MCS) profiles acquired during *Oceanus* Cruise 270 (Oc270, summer 1995), collected both in site-specific "hazards" grids (Fig. 30) and as a regional survey stretching from Leg 150 sites on the continental slope to the south to the Hudson Apron in the east (see "Introduction" chapter, this volume). These data were collected using a 48-channel receiver (6.25 m groups; 22 m offset to the near-trace) and a single generator-injector (GI) air gun towed at 2–3 m below the sea surface. Resolution is estimated to be ~5 m vertically throughout the interval anticipated for Leg 174A drilling and sampling (to ~1.2 s two-way traveltime [TWTT]). The Oc270 data build upon two other primary geophysical data sets: (1) preexisting (late 1990) regional MCS profiles collected by *Maurice Ewing* (Cruise 9009), and (2) downhole logs and velocities from a checkshot survey collected in an adjacent industry well, the Continental Offshore Stratigraphic Test (COST) B2 (Scholle, 1977).

We illustrate sequence-stratigraphic surfaces penetrated and sampled at Holes 1071A–1071E, along Oc270 seismic Profiles 885 and 806 (Figs. 31, 32) and Holes 1071F–1071G, located at the intersection of Profiles 801 (Fig. 33) and 814; structure maps to selected horizons are also shown (Figs. 34, 35). Using velocity functions derived from semblance analyses of Oc270 Profile 51, and the checkshot survey results from the COST-B2 well (Fig. 36), traveltime-depth conversions of selected seismic surfaces (Table 40) were used first to predict, then to attempt to tie lithologies sampled at Site 1071 to the regional sequence-stratigraphic framework (see below). Geological conditions in the COST-B2 well, primarily as inferred from its logs, were also used to predict hole conditions and the nature of the geologic section at Site 1071 (see "Downhole Logging" section, this chapter). Traveltime-depth predictions at Site 1071 were also made using a Site 1072 checkshot survey (see "Downhole Logging" sections, this chapter and "Site 1072" chapter, this volume).
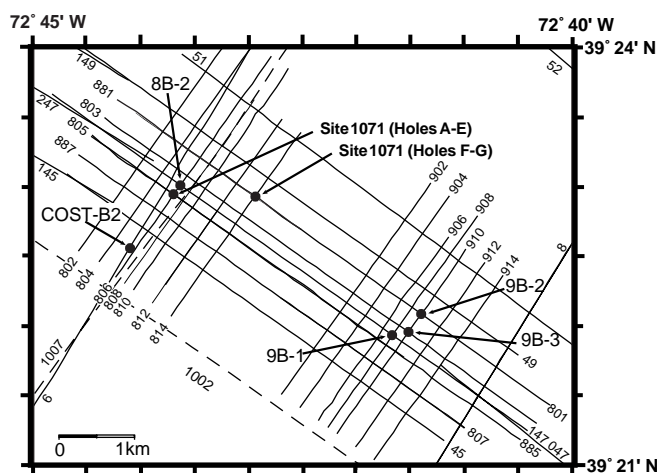

Figure 30. Map of proposed Leg 174A shelf sites (MAT-8B2, 8B3/Site 1071, Holes 1071A–1071E and Holes 1071F and 1071G; MAT-9B1/Site 1072, MAT-9B2, and 9B3), the COST-B2 well, and track lines of MCS profiles collected during Cruises Oc270 (solid lines) and Ew9009 (dashed lines). COST-B2 is ~950 m south-southwest of the proposed MAT-8B3/Site 1071, Holes 1071A–1071E, ~75 m northwest of cdp 10435 of Profile 806 (Fig. 32), and ~180 m northwest of cdp 4652 on Ew9009 Profile 1007. Stacking velocities were measured at ~1-km intervals along Oc270 Profile 51 (see Fig. 36) and Ew9009 Profile 1002 in the vicinity of the MAT-8B grid.
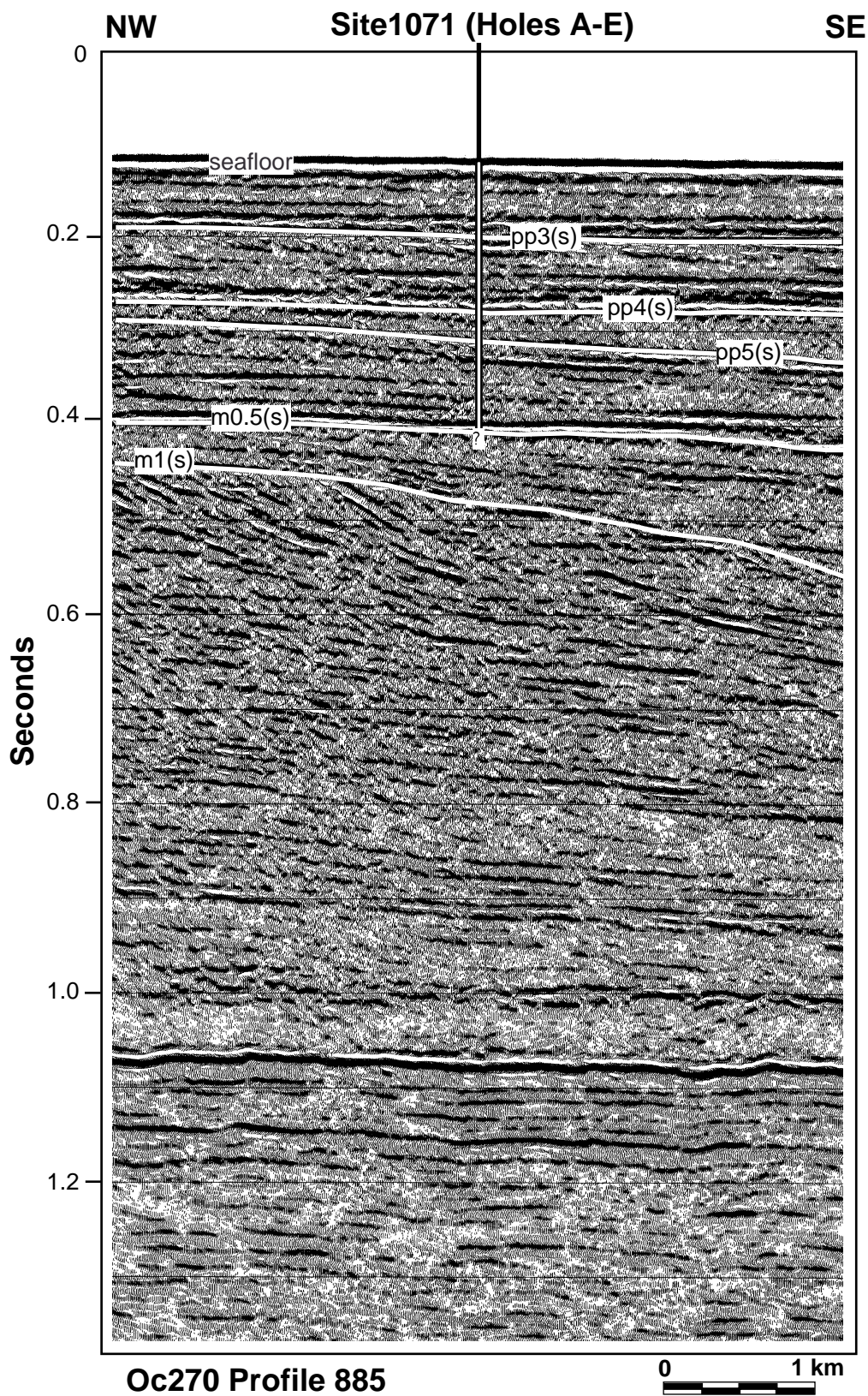
Figure 31. Interpreted version of part of Oc270 Profile 885, a dip section running through Site 1071 (see Fig. 30). The approximate total depth (TD) penetrated in Holes 1071A–1071E at the site is indicated (vertical white bar), as are the locations of prominent stratigraphic discontinuitie s/sequence boundaries identified by tying previously interpreted regional Ew9009 profiles to the Oc270 profiles (Christie-Blick et al., 1992; Mountain, Miller, Blum, et al., 1996; Austin et al., 1996).
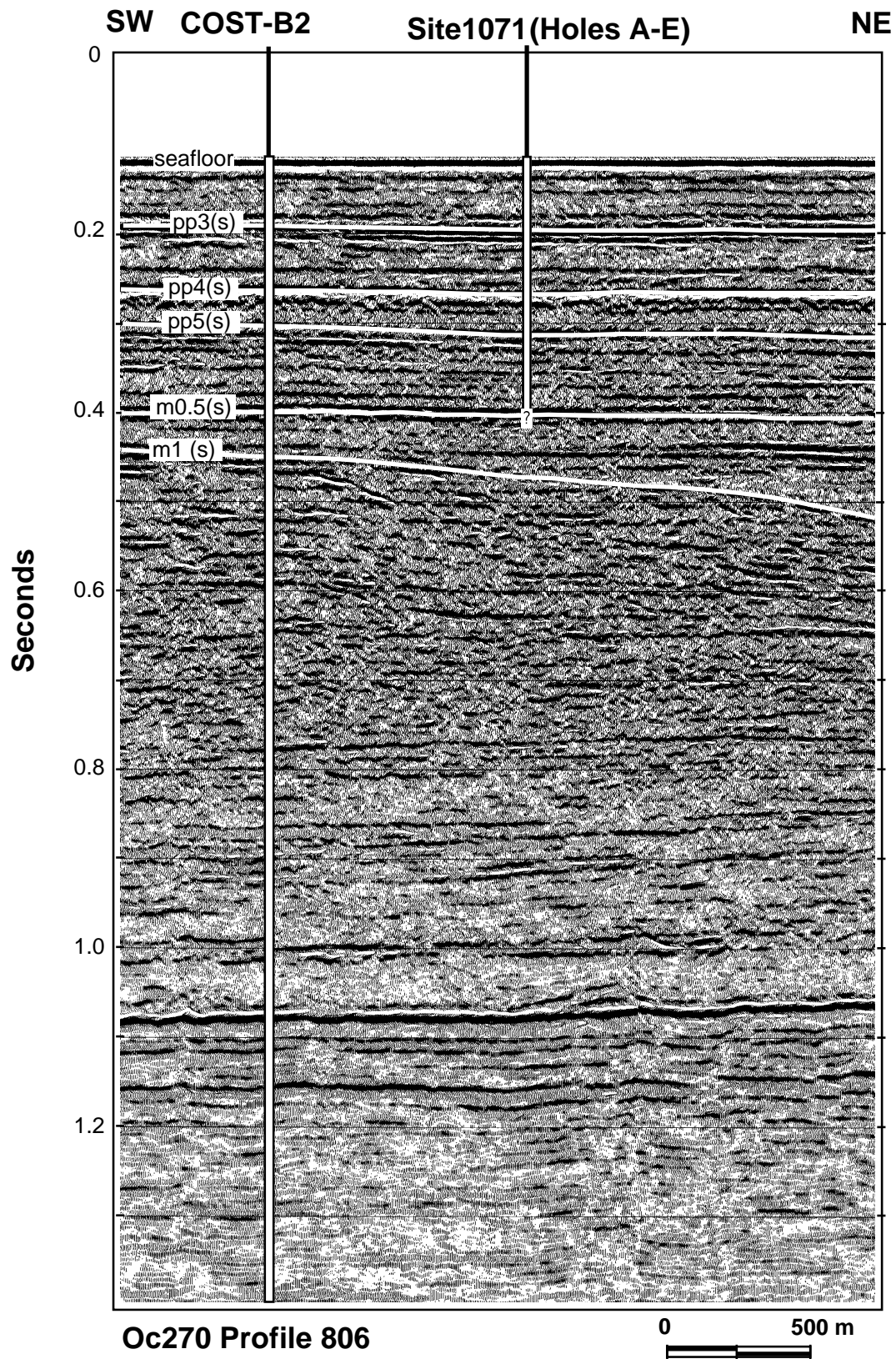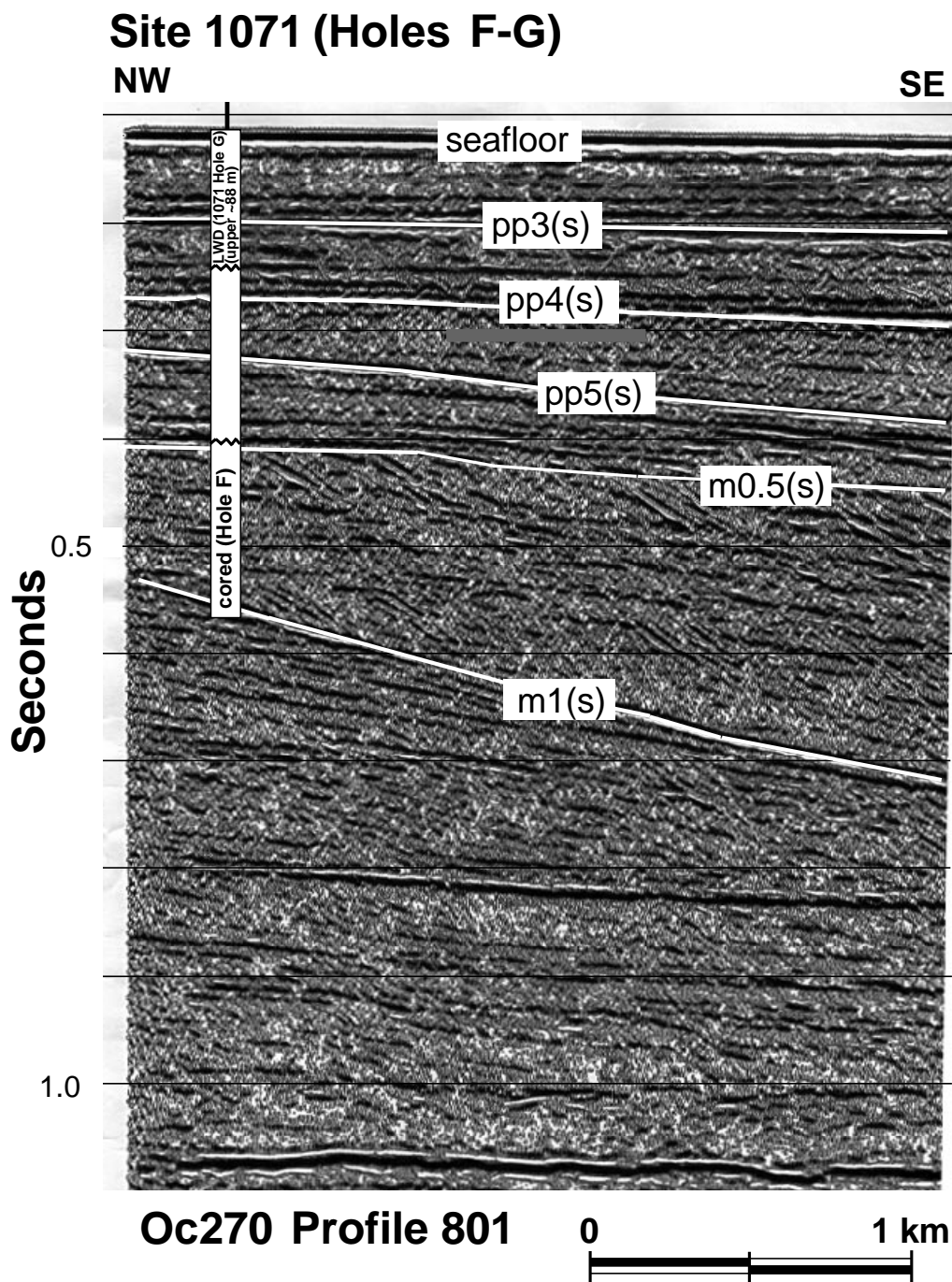
Figure 32. Interpreted version of part of Oc270 Profile 806, a strike section running through Site 1071, Holes 1071A–1071E (see Fig. 30) and near COST-B2 (see "Downhole Logging" section, this chapter). The TD penetrated in Holes 1071A–1071E at the site and at COST-B2 are indicated (vertical white bars), as are the locations of prominent stratigraphic discontinuities/sequence boundaries identified by tying previously interpreted regional Ew9009 profiles to the Oc270 profiles (Christie-Blick et al., 1992; Mountain, Miller, Blum, et al., 1996; Austin et al., 1996).

Figure 33. Interpreted version of part of Oc270 Profile 801, a dip profile running through Site 1071, Holes 1071F and 1071G (see Fig. 30). Hole 1071F was cored only from the approximate level of m0.5(s) to m1(s); LWD was attempted to 95.1 mbsf in Hole 1071G (see "Downhole Logging" section, this chapter).

Predicting and Mapping Sequence Boundary Depths

A base map of the area (Fig. 30) displays the Oc270 seismic data, two *Ewing* 9009 regional profiles that cross this region, the COST-B2 well location, and the proposed and approved MAT-8B and 9B drilling locations. MAT-8B3 became Holes 1071A–1071E, and the intersection of Profiles 814 and 801 (a new site, MAT-8B4, proposed and approved during the leg) became Holes 1071F–1071G. Figures 31 (dip seismic Profile Oc270-885) and 32 (strike seismic Profile Oc270-806, which crosses dip seismic Profile Oc270-885 approximately at Holes 1071A–1071E; see "Operations" section, this chap-

ter) illustrate some of the key seismic sequence boundaries that were mapped into the Oc270 data using a sequence-stratigraphic framework derived from previous (e.g., Greenlee et al., 1992) and ongoing (Fulthorpe and Austin, 1998) interpretations of industry MCS data and extrapolations from Leg 150 (Mountain, Miller, Blum, et al., 1994; Miller et al., 1996) and Ew9009 profiles (e.g., to Oc270 MCS profiles; Christie-Blick et al., 1992; Mountain et al., 1996; Austin et al., 1996; see "Introduction" chapter, this volume). The primary stratigraphic goal for initial drilling and logging at Site 1071 was the m1(s) clinoform, presumed from Leg 150 results to be ~11 Ma (Miller et al., 1996). The "s" designations following the "pp" (provi-
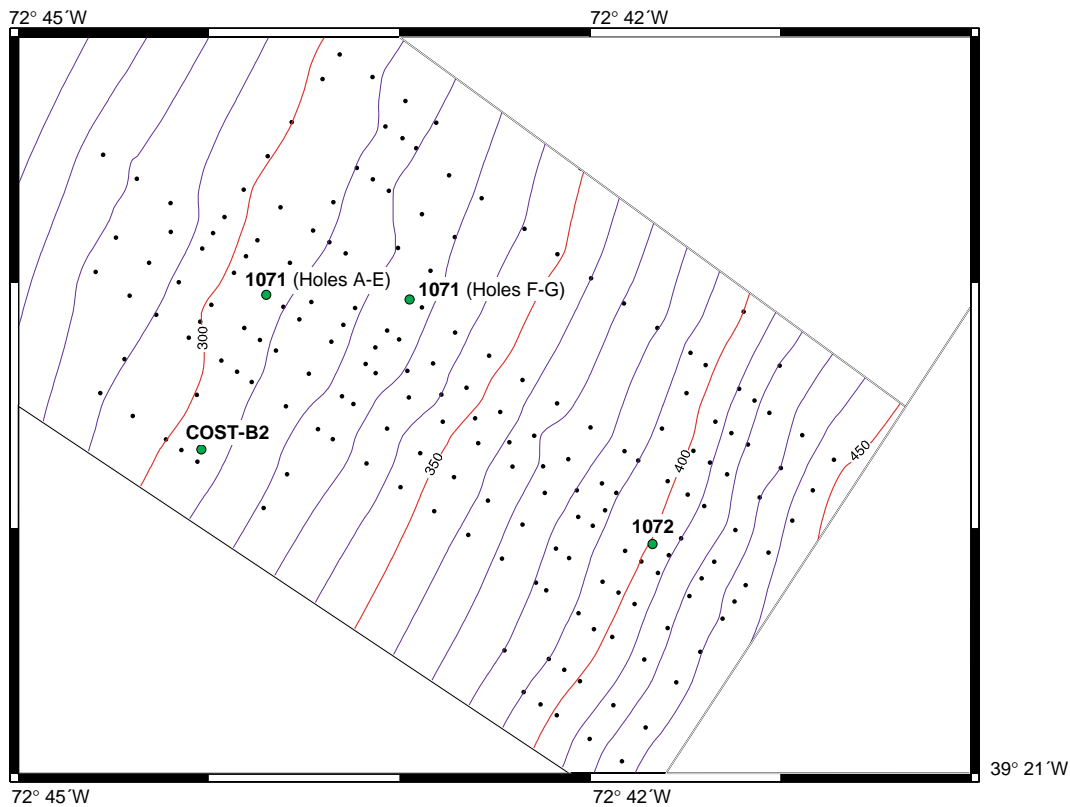
Figure 34. Structure of pp5(s) in meters below the sea surface, derived from a map of the same feature in traveltime. The COST-B2 checkshot survey (see Table 40) was used for the traveltime-depth conversion. This surface, which may be a flooding surface located within a transgressive interval rather than a sequence boundary (see Fig. 37 and "Summary and Conclusions" section, this chapter), dips uniformly seaward at ~1.5° between Sites 1071 and 1072 (see Fig. 30).

sionally Pliocene–Pleistocene) and "m" (provisionally Miocene) sequence boundary identifications are meant to distinguish the shelf sequence boundaries targeted for sampling and logging by Leg 174A from similarly labeled surfaces calibrated on the slope during Leg 150 (Mountain, Miller, Blum, et al., 1994). Holes 1071A–1071E were placed to sample m1(s) near its rollover/breakpoint (see "Introduction" chapter, this volume). Unstable conditions in Holes 1071A–1071E prevented drilling to m1(s); however, Hole 1071F (~1.1 km to the east; Figs. 30, 33, and 37) succeeded in penetrating to that sequence boundary, although core recovery was extremely poor (see "Lithostratigraphy" section, this chapter). Prospective sequence boundaries pp3(s), pp4(s), and pp5(s) were sampled; their stratigraphic significance is discussed below. Hole 1071C ended at or very near a sequence boundary termed m0.5(s) that lies between the "pp" discontinuities and the m1(s) surface. The possible tie of m0.5(s) to COST-B2 logs is also discussed briefly below and more extensively elsewhere (see "Downhole Logging" section, this chapter).

Time-Depth Estimation Technique

Two different techniques were used to predict depths from traveltimes using Oc270 MCS profiles at or near Site 1071. The first involved using the COST-B2 vertical seismic profile (VSP) or checkshot survey (Smith et al., 1976; see also "Downhole Logging" section, this chapter). These data were converted to two-way traveltime (TWTT) in milliseconds below seafloor (msbsf) and meters below seafloor (mbsf); they are well-described by a third-order polynomial fit down to ~1400 mbsf (Fig. 36):

$$\text{Depth (mbsf)} = M0 + M1(\text{msbsf}) + M2(\text{msbsf})^2 + M3(\text{msbsf})^3, \quad (1)$$

where M0 = 0.25963, M1 = 0.94, M2 = –1.18 × 10⁻⁵, and M3 = 7.70 × 10⁻⁸.

The second was a compilation of semblance or stacking velocity analyses used for normal moveout corrections of Oc270 Profile 51 near the site (Fig. 30). Semblance or stacking velocities were also used from adjacent *Ewing* 9009 and other *Oceanus* Oc270 profiles. This analysis was accomplished by picking coherency maxima on semblance plots at ~1-km intervals along track in both data sets. The actual number of discrete velocity picks at any one common depth point (cdp) was determined by the operator; typically, five to seven traveltime-velocity pairs were chosen in the interval of seafloor to 1000 mbsf. Then, these data were converted to interval velocities below seafloor. As with the COST-B2 checkshot survey (Eq. 1), a third-order polynomial (coefficients: M0 = –16.189, M1 = 0.97222, M2 = –0.00015, M3 = 1.49 × 10⁻⁷) was fitted to all traveltime vs. interval-velocity picks adjacent to the MAT grids in water depths between 100 and 150 ms (~75–112 m); this curve was then used to calculate TWTT below seafloor vs. mbsf at 100 ms increments. A comparison of plots of both curves (Fig. 36) shows that at any given traveltime below seafloor, the COST-B2 curve predicts depths that are 6%–10% deeper than those from the site-specific MCS results (see "Downhole Logging" section, this chapter). Both curves were used in advance of the drilling for predicting depths to sequence boundaries/stratigraphic discontinuities interpreted using the Oc270 data at or near Holes 1071A–1071E (Figs. 30–32). As Holes 1071F–1071G were further from the COST-B2 well, only the Oc270 velocities were initially used for time-depth conversion there (Table 40). However, after the Site 1072 checkshot survey was conducted (see "Site 1072" chapter, this volume), those velocities were also used for time-depth conversion at Site 1071 (Table 40).
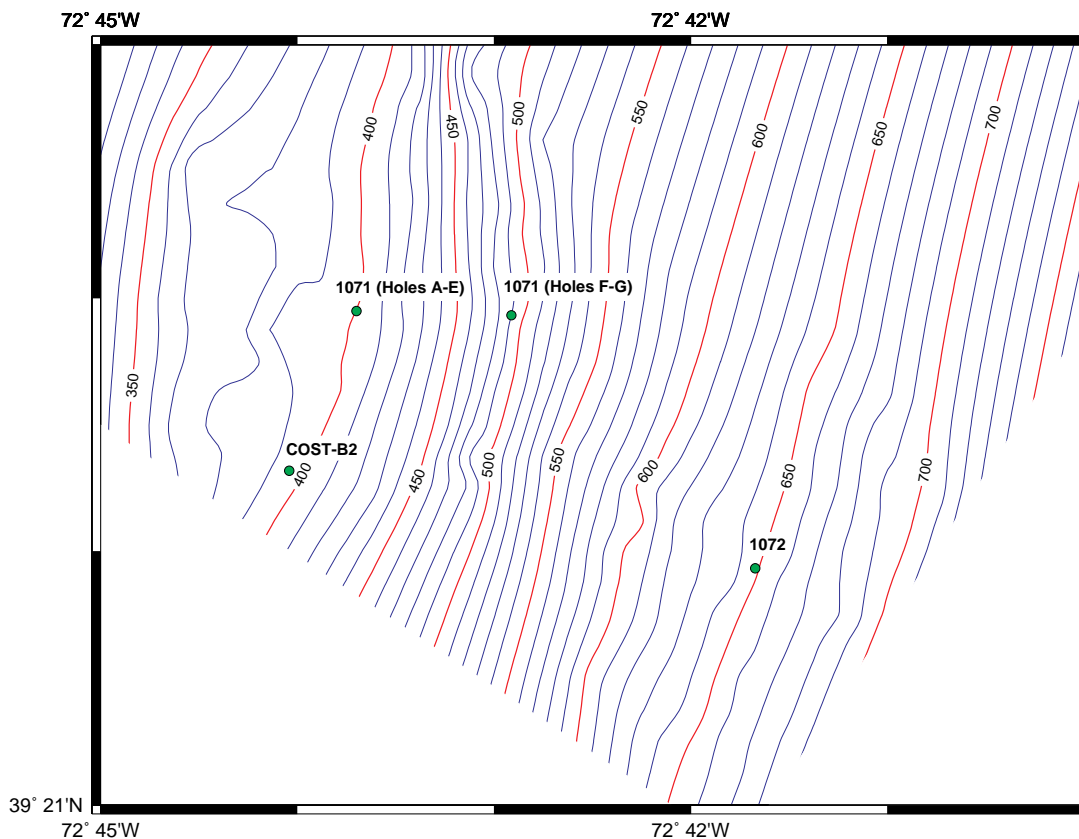
Figure 35. Structure of m1(s) in meters below the sea surface, derived from a map of the same sequence boundary in traveltime. The COST-B2 checkshot survey (see Table 40) was used for the time-depth conversion. This sequence boundary, ~11 Ma (Miller et al., 1996), marks the top of a late middle Miocene clinoform that was the primary goal for drilling and sampling at Site 1071; m1(s) was probably penetrated in Hole 1071F (see Fig. 33). The clinoform front southeast of the rollover/breakpoint, and located near Site 1071, Holes 1071A–1071E, dips seaward at ~4.1° (avg.) and exhibits >200 m of relief.
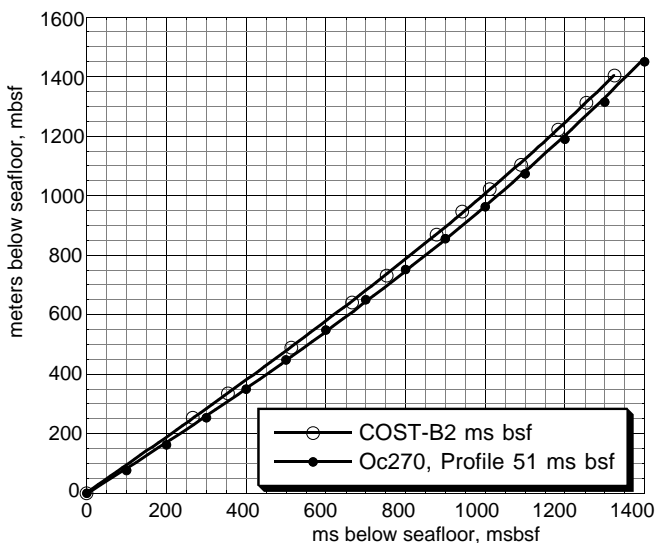
Figure 36. Traveltime-depth ties at the crossing of Oc270 Profiles 806 and 885 at the location of Site 1071, using a checkshot survey/VSP from the COST-B2 well and an average velocity-traveltime relationship derived from semblance picks interpreted at ~1-km intervals from adjacent Oc270 Profile 51 (see Fig. 30 and Table 40).

Calculation of Sequence Boundary Depths

Using both the Oc270 Profile 51 and COST-B2 time-depth conversion equations, depths to sequence boundaries interpreted on Oc270 profiles in the MAT-8B grid (Fig. 30) were calculated (Table 40). These depths were used by the Shipboard Scientific Party as guides for interpretation of lithostratigraphy (see "Lithostratigraphy" section, this chapter), magnetostratigraphy (see "Paleomagnetism" section, this chapter), and biostratigraphy (see "Biostratigraphy" section, this chapter) during drilling of all seven holes at Site 1071. A preliminary synthesis of those results is presented below (Fig. 37).

Structural Mapping of Sequence Boundaries

As another predictive tool, traveltime and depth structure maps to selected sequence-stratigraphic horizons were prepared during drilling at Site 1071. Two such maps are shown, one for pp5(s) (Fig. 34) and the other for m1(s) (Fig. 35). Both initially presumed sequence boundaries dip to the southeast, toward the modern shelf edge. The pp5(s) surface dips seaward at an almost constant dip of ~1.5° (avg.). The m1(s) clinoform dips ~4.1° (avg.) seaward of its rollover/breakpoint at Site 1071; however, the clinoform dips reach 6° just seaward of Site 1071, before flattening beyond MAT-9B1/Site 1072 to ~3° (Fig. 30).

Outer Shelf Late Miocene/Pleistocene Sequence Boundaries: Preliminary Lithostratigraphic/ Chronostratigraphic Correlations

Figure 37 summarizes preliminary ties between sequence boundaries identified regionally on Oc270 Profile 885 and the lithostratig-

Table 40. Traveltimes and equivalent depths for Site 1071 surfaces interpreted on seismic data from around Site 1071.

	TWTT (s)	TWTT (sbsf)	Depth (mbsf*)	Depth range (mbsf**)	Depth (mbsf***)	TWTT (s/mbsf COST-B2†)	Comments
Sequence boundaries at 806/885 (Holes 1071A–1071E)							
Seafloor (Depth: 88 m)	0.117	0.000	0				
late Miocene–Pleistocene (provisional)							
pp3(s)	0.192	0.075	56	53-59 (71)	62	0.080/75	Hiatus/offlap/onlap
pp4(s)	0.271	0.154	131	124-138 (145)	137	0.151/142	Hiatus/offlap/onlap
pp5(s)	0.307	0.190	164	156-172 (179)	171	0.183/172	Possible onlap
Miocene (Miller et al., 1996)							
m0.5(s)	0.394	0.277	245	233-257 (261)	253	0.283/267	Hiatus/offlap/onlap
m1(s)	0.470	0.353	314	298-330 (334)	325	0.337/319	Hiatus/offlap/onlap (Note: not sampled at Site 1071, Holes 1071A–1071E)
Sequence boundaries at 801/814 (Holes 1071F-1071G)							
Seafloor (Depth: 90 m)	0.120	0.000	0				
pp3(s)	0.197	0.077	58	55-61	64		
pp4(s)	0.282	0.162	138	131-145	not sampled		
pp5(s)	0.323	0.203	176	167-185	not sampled		
m0.5(s)	0.414	0.294	260	247-273	269		
m1(s)	0.557	0.437	392	372-412	405		

Notes: TWTT = two-way traveltime, sbsf = seconds below seafloor. * = calculated using semblance velocities from Oc270, Profile 51 (Fig. 36). ** = representing a potential error of ±5% in traveltime-depth conversion (using the Oc270, Profile 51 input velocity curve). Depth using COST-B2 checkshot velocity function (Fig. 36) is in parenthesis. *** = calculated using Site 1072 checkshot survey, see "Downhole Logging" sections, this chapter and "Site 1072" chapter (this volume). † = depth of sequence boundary at closest-point-of-approach of COST-B2 to Oc270, Profile 806 (Fig. 32): ~75 m northwest of cdp 10435, ~0.95 km south-southwest of Site 1071. The depths in this table were used for prediction purposes prior to drilling; the stratigraphic significance of each boundary, based upon the cores, is discussed in the text (see also "Lithostratigraphy," "Biostratigraphy," and "Downhole Logging" sections, this chapter). The relationships illustrated in Figure 36 were used for interpretations.
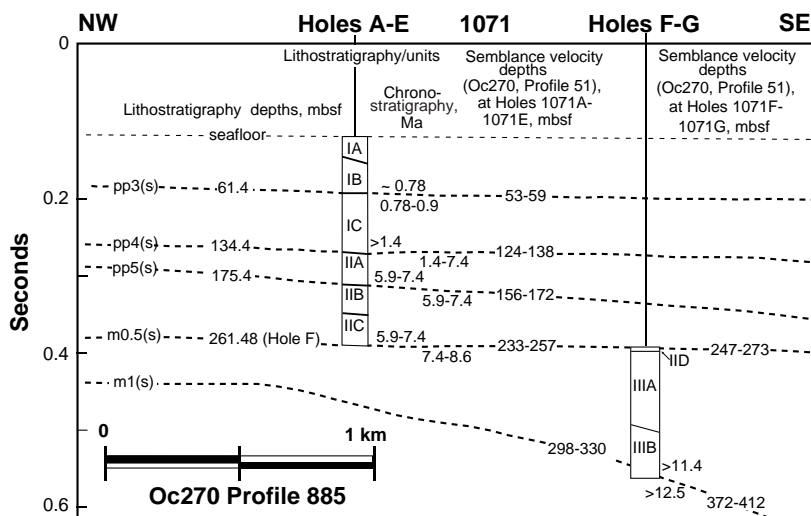
Figure 37. Schematic of a portion of Oc270 Profile 885 in the vicinity of Site 1071, summarizing tentative correlations between the lithostratigraphy and chronostratigraphy at the site, Holes 1071A–1071G, and interpreted late Miocene–Pleistocene surfaces. (Further details are found in the "Lithostratigraphy," "Biostratigraphy," and "Summary and Conclusions" sections, this chapter.)

raphy and chronostratigraphy developed at Site 1071. From the top down, three "Pliocene–Pleistocene" discontinuities were identified: pp3(s), pp4(s), and pp5(s). The pp3(s) boundary may correlate with the transition between lithostratigraphic Subunits IB and IC at ~61.4 mbsf; the predicted depth range for this surface is 53–59 mbsf (Table 40). Compressional wave velocity and density both decrease downhole at ~59–65 mbsf, and a small downhole increase in shear strength occurs at ~61.4 mbsf (see "Physical Properties" section, this chapter). This surface is <0.78–0.9 Ma, based in part upon its close association with the B/M boundary (see "Biostratigraphy" and "Paleomagnetism" sections, this chapter). The transition from lithostratigraphic Subunit IC to IIA at 134.4 mbsf corresponds approximately with pp4(s) (within an unrecovered interval between 134.4 and 143.5 mbsf). The predicted depth range of pp4(s) is 124–138 mbsf (Table 40), slightly shallower than the depth interpreted using checkshot velocities from the COST-B2 well (~145 mbsf; Fig. 43). Compressional wave velocity and density both increase downhole at ~125–130 mbsf (see "Physical Properties" section, this chapter). Sequence boundary pp4(s) may mark a Miocene/Pleistocene hiatus; it is tentatively dated

at >1.4 Ma (above) and 1.4–7.4 Ma (below; Fig. 37). The pp5(s) discontinuity is a prominent seismic reflection close to the transition between Subunits IIA and IIB at 175.4 mbsf. Its predicted depth range is 156–172 mbsf (Table 40). Density and compressional wave velocity both increase downhole at ~168–174 mbsf, coincident with a downhole decrease in shear strength at ~175 mbsf (see "Physical Properties" section, this chapter). The pp5(s) discontinuity appears to correspond with a prominent facies change (fining upward) at 173.5 mbsf (Fig. 4). The age of pp5(s) is 7.4–5.9 Ma, relying on biostratigraphic information alone (see "Biostratigraphy" section, this chapter). This may make pp5(s) a flooding surface rather than a sequence boundary and late Miocene rather than Pliocene–Pleistocene in age (see "Lithostratigraphy" and "Summary and Conclusions" sections, this chapter).

Hole 1071C ended at 257.4 mbsf, 1 m below a highly indurated pebbly glauconitic sandstone with a P-wave velocity of ~5.5 km/s (see "Physical Properties" section, this chapter). Correlation with the COST-B2 well (see "Downhole Logging" section, this chapter) suggests that this sandstone in part causes the high-amplitude, flat-lying

reflection associated with m0.5(s) (~267 mbsf at COST-B2; Table 40; see below), and at Hole 1071C the sequence boundary may lie slightly below the bottom of the hole (predicted depth range of 233–257 mbsf; Table 40). Sediments at the bottom of Hole 1071C are tentatively dated at 8.6–5.9 Ma (Fig. 37), making m0.5(s) roughly the same age as the analogous surface calibrated by Leg 150 (Mountain, Miller, Blum, et al., 1994).

Holes 1071F and 1071G were placed ~1.1 km east of Holes 1071A–1071E (Figs. 33, 37); the goal was to sample to and through m1(s) about one-third of the way down the m1(s) clinoform front, where sediments were predicted to be finer grained than at the top of the clinoform at Holes 1071A–1071E (see "Background and Objectives" section, this chapter). Coring began at 252 mbsf, just above the TD of Hole 1071C and the presumed position of m0.5(s) sequence boundary. Based upon the lithostratigraphic results from Hole 1071F, m0.5(s) may correspond to the Subunit IIC/IID transition at (or near) 261.48 mbsf (Fig. 37; see "Lithostratigraphy" section, this chapter). This surface was predicted to be at a depth range of 247–273 mbsf on the basis of semblance velocities but, by comparison with other information, could be deeper than that by perhaps 5% (~13 m) (Table 40). Hole 1071F terminated at 424.2 mbsf, having presumably penetrated surface m1(s) (Figs. 33, 37); the predicted depth range to m1(s) was 372–412 mbsf (Table 40). Unfortunately, core recovery in Hole 1071F was very poor in predominantly muddy sands (see "Lithostratigraphy" section, this chapter), and attempts at LWD in Holes 1071F and 1071G resulted in only ~88 m of logs (see "Downhole Logging" section, this chapter), so a penetration of m1(s) could not be confirmed. However, fluctuations in *P*-wave velocities on discrete samples recovered between 370 and 415 mbsf may signify the presence of m1(s) within this interval (see "Physical Properties" section, this chapter).

DOWNHOLE LOGGING

Introduction

Several operational difficulties prevented downhole logging at Holes 1071A through 1071D, and although lowered to 60 mbsf (15 m below the pipe) in Hole 1071E, the sonic-resistivity logging string (DIT-E/SDT/NGT) was unable to go deeper and logging was canceled in this hole (see "Operations" section, this chapter). At Hole 1071F, hole conditions again thwarted wireline logging efforts when the sonic-resistivity string (DIT-E/LSS/NGT) was unable to pass a bridge at 74 mbsf, 21 m below the bottom of the pipe. Consequently, LWD operations at Hole 1071G constituted the only substantial logging at this site, down to ~95 mbsf, where the LWD BHA became stuck.

Despite the small amount of downhole logging data acquired on Leg 174A, wireline logs collected at the COST-B2 well provided useful and relevant information (Scholle, 1977). The COST-B2 well is located 950 m south-southwest of Holes 1071A through 1071E and 1800 m west-southwest of Holes 1071F and 1071G. These short distances, and the moderately level gradient of most surfaces seen in seismic profiles (see "Seismic Stratigraphy" section, this chapter), suggest that meaningful insight into the stratigraphy at Site 1071 can be inferred from ties to the COST-B2 well data. In this chapter, we discuss the LWD data at Hole 1071G and summarize the COST-B2 log data over the interval cored at Site 1071.

Hole 1071G Logging Operations

Hole 1071G was spudded at 1200 hr on 12 July 1997 with the Compensated Dual Resistivity (CDR)/Compensated Density Neutron (CDN) LWD tools mounted on the BHA. The BHA stuck abruptly after the drill bit reached 95 mbsf. After several unsuccessful attempts to free the BHA, we retrieved the recorded data and the CDN nuclear sources using a specially designed wireline logging tool

(LWD Inductive Coupling [LINC] tool). Data from the CDN and CDR tools from 0 to 88 mbsf were successfully retrieved from the hole. After securing the nuclear sources on the rig floor and rigging down the wireline LINC tool, the BHA became unstuck, and the logging run was terminated.

Hole 1071G Data Quality

LWD data at Hole 1071G are adversely affected in some intervals by borehole washouts and an excessively high ROP (>35 m/hr; Fig. 38). However, both the caliper and the ROP data are to a large extent controlled by lithology, and thus both are useful in log evaluation and interpretation. The deep and shallow resistivity measurements are offset within the low gamma-ray intervals, suggesting early invasion of coarser grained, more permeable intervals by the lower resistivity borehole fluid. In high gamma-ray intervals, shallow and deep resistivity are nearly identical, suggesting little or no invasion.

The caliper tools are a valuable indicator of log quality (Fig. 38). Where the differential caliper records values >1, the tool is more than 1 in from the borehole wall; in these cases, the density, neutron porosity, and PEF (photoelectric factor) logs may not record physical properties accurately. Where the differential caliper reads 0, it is likely that the hole diameter was too large for the differential caliper to detect any change in diameter. In these cases, the phase-shift caliper often records a large borehole diameter because it measures farther from the tool than the differential caliper. Where the differential caliper reads between 0 and 1, density measurements are reliable.

Prominent peaks and troughs in gamma-ray, resistivity, and density logs suggest interbedding of sands and shales at a meter to decimeter scale (especially in the interval from 15 to 45 mbsf). Zones with a low differential caliper are associated with higher gamma-ray values and higher densities than zones with large differential caliper values. This suggests that the shale-prone intervals are less subject to borehole washout and are denser than sandy intervals.

Core-log Comparison

The uppermost 20 m of logs at Hole 1071G correlates well with the recovered lithology (Fig. 38). Gamma ray and resistivity decrease upward from 5 to 0 mbsf; this interval corresponds to muddy sands and silty sands in Core 174A-1071A-1H (see "Lithostratigraphy" section, this chapter). Between 20 and 15 mbsf, gamma-ray values increase upward, consistent with the thinning- and fining-upward trend of sand beds observed at the top of Core 174A-1071A-5H. This interval is overlain by silty clays and clayey silts that correspond to higher gamma-ray values. Between 20 and 40 mbsf, only partial core recovery was achieved. In this interval, there is a complex alternation of high and low gamma-ray peaks that are interpreted to record interbedded sands and muds.

An abrupt boundary at 45 mbsf separates sand-rich sediments (low gamma ray) above from clay-rich sediments below (high gamma ray). Within the high gamma-ray interval (45–67 mbsf) there was only partial core recovery, yielding mostly small sections of muddy sediment. The overall high gamma-ray values indicate that this interval is composed primarily of muddy sediments. A second abrupt boundary occurs at 67 mbsf, below which gamma-ray and resistivity values are low and progressively decrease downhole. We correlate the contact at 67 mbsf to correspond to a prominent flooding surface (Fig. 38). The pp3(s) sequence boundary is interpreted at 65 mbsf, which corresponds to the top of a 2-m interval of upward-decreasing gamma-ray and upward-decreasing resistivity values. This trend suggests a coarsening-upward unit immediately beneath pp3(s).

Physical properties measured in Holes 1071A–1071C show good correlation with the logs, except for the interval just below 20 mbsf, where a thick interval of low gamma-ray sand was recovered; the LWD gamma ray increases toward the base of the same interval (Fig. 39). We suspect that suck-in effects of piston coring may have in-
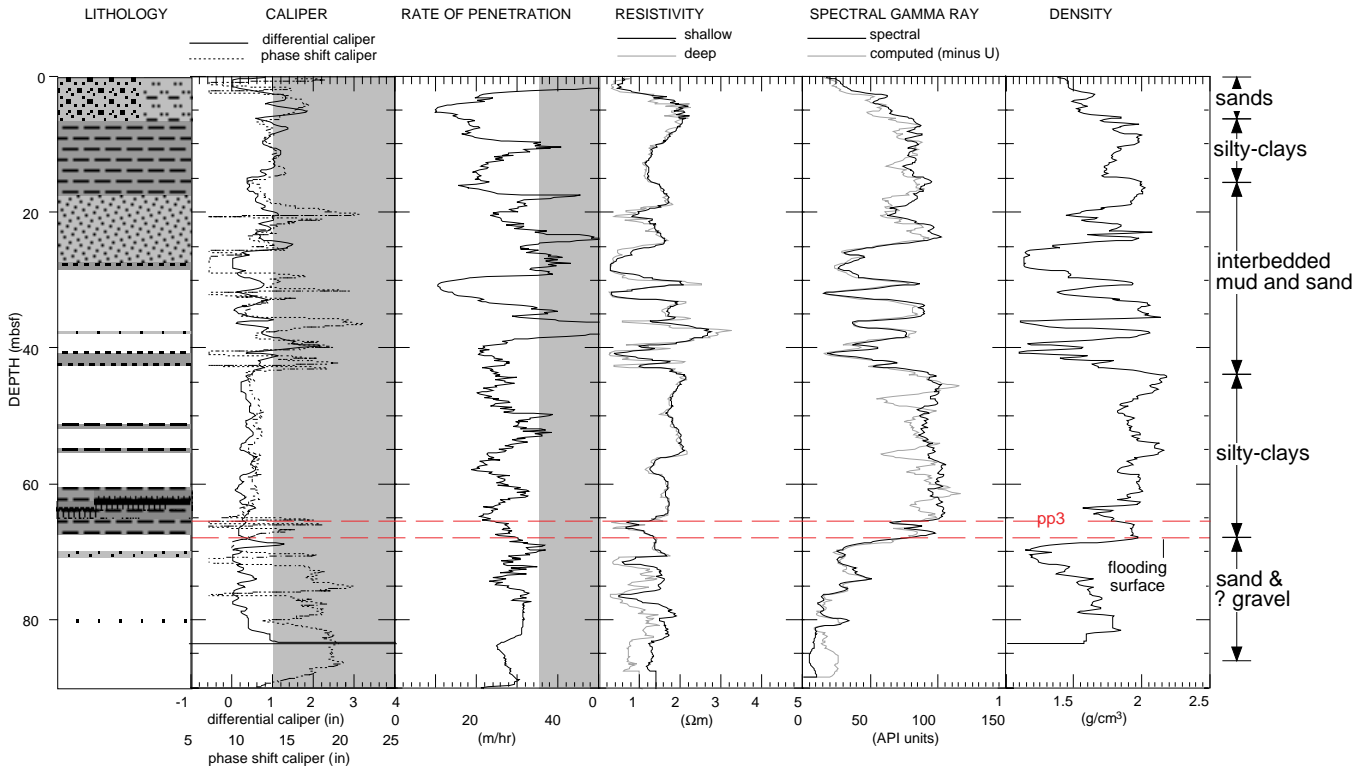
Hole 1071G

Figure 38. Summary of LWD data obtained at Hole 1071G. Schematic lithology column was derived from Holes 1071A, 1071B, and 1071C. Lithology symbols are described in "Lithostratigraphy" section, this chapter; white corresponds to intervals of no recovery.

creased the recovered sand thickness in this interval (see "Physical Properties" section, this chapter).

COST-B2 Well

The COST-B2 well was drilled in 1976 to a depth of 4766 mbsf from a semisubmersible platform anchored in 90.8 m (298 ft) of water (Scholle, 1977). The kelly bushing was 27.4 m above sea level. Thirty-inch casing was set from the seafloor to 60 mbsf, and additional 20-in casing was set inside from the seafloor to 207.8 mbsf. A gamma-ray log was run from TD to the casing at 207.8 mbsf, and then up to the seafloor. The remaining suite of wireline logs was run entirely below casing. We have incorporated the following wireline log data in our analysis: caliper, gamma-ray, conductivity, velocity, and checkshot survey.

Time-Depth Estimates

Before drilling, we used two independent methods for calculating depths to seismic surfaces targeted for drilling. These surfaces are shown on Oc270 Profile 806, a profile that goes through Site 1071 and passes 75 m south-southeast of the COST-B2 well (see Figs. 36, 40, and description of this time-depth correlation in "Seismic Stratigraphy" section, this chapter). One method was based on the checkshot velocity data from the COST-B2 well. The other was based on stacking velocities prepared for normal moveout corrections of the Oc270 site-survey seismic data.

Velocity-depth patterns derived by these methods provide overlapping estimates that are further corroborated by shipboard *P*-wave velocity measurements (Fig. 41; also see "Physical Properties" section, this chapter). The first checkshot measurement in the COST-B2 well was taken at 252 mbsf, which coincides with the deepest ship-
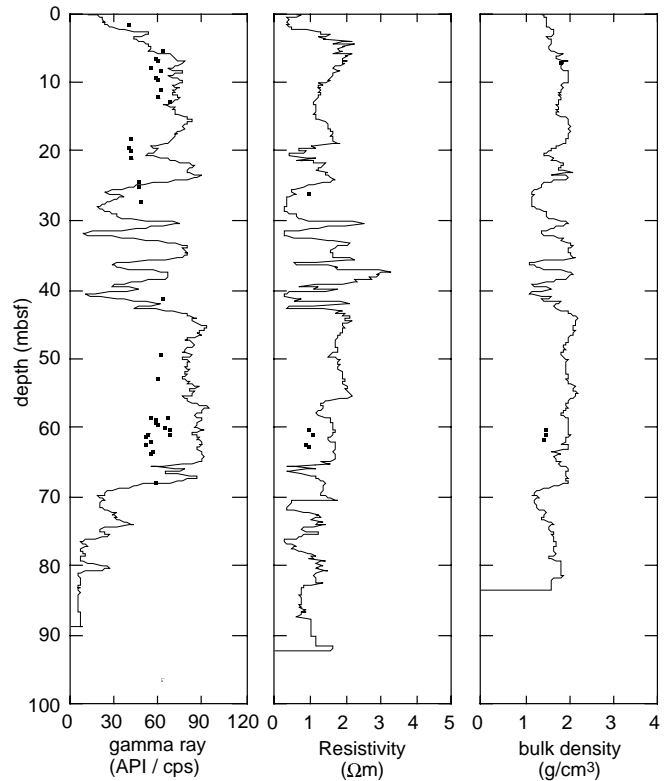
Figure 39. Comparison of LWD logs (lines) collected in Hole 1071G and physical properties (squares) measured in cores from Holes 1071A, 1071B, and 1071C (see "Physical Properties" section, this chapter).
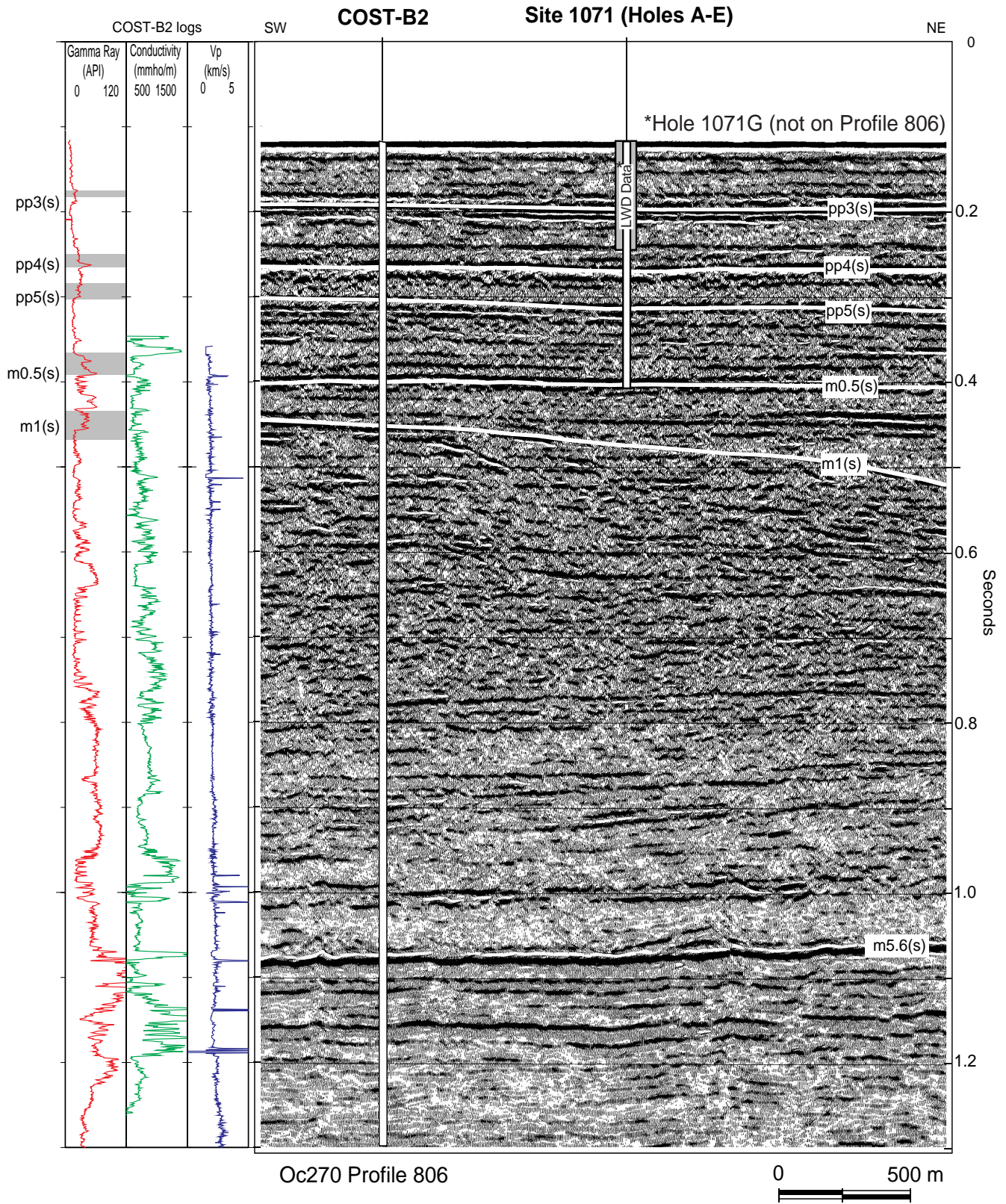
Figure 40. Oc270 Profile 806 with COST-B2 wireline log data converted to traveltime and shown at the same scale. Traveltime-depth correlations were made with COST-B2 checkshot data (see "Seismic Stratigraphy" section, this chapter). Location shown in Figure 30. Gray bars represent depth ranges of surfaces at Site 1071 calculated using Oc270 Profile 51 velocity curve (see Table 40).
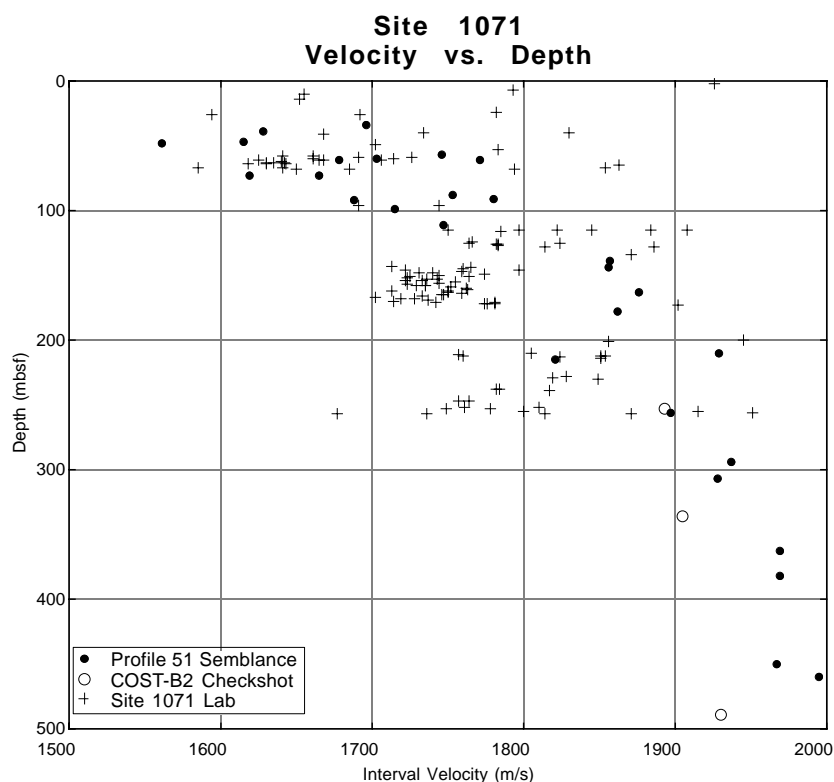
Site 1071
Velocity vs. Depth

Figure 41. Velocity vs. depth plot of COST-B2 checkshot data, Site 1071 V_p measurements made on split cores, and stacking velocities estimated from analysis of Oc270 Profile 51. Note the scatter of split-core measurements relative to those from COST-B2 and Oc270 semblance velocities. However, depths predicted from COST-B2 and Profile 51 differ only slightly (see Fig. 36).

board *P*-wave velocity measurement in Holes 1071A–1071E. For the first 200 m, Oc270 stacking velocities increase rapidly from a seafloor value of 1550 m/s. Below 250 mbsf, both the checkshot and stacking velocity data show a more gradual increase in velocity with depth.

A checkshot survey was completed at Site 1072 (see Table 23, "Site 1072" chapter, this volume). Because of the short distance from Site 1071, the similarities of the two geologic settings, and the nearly horizontal aspect of stratal surfaces throughout the drilled interval in both locations, we have used Site 1072 checkshot velocities to derive depths to sequence boundary reflections at Site 1071. All figures in this section show reflections placed at depths calculated in this way.

Log-Seismic Tie: COST-B2 Well

We describe the COST-B2 log characteristics and show how seismically mapped surfaces on Oc270 Profile 806 tie to this well using the checkshot survey data from Site 1072 (see Table 23, "Site 1072" chapter, this volume). Above 60 mbsf, the gamma-ray logging tool was recording measurements through two strings of casing; consequently, formation properties are highly attenuated (Fig. 42). Beneath the 30-in casing, yet within the 20-in casing (60–207.8 mbsf), the same log exhibits considerable variation, which we interpret to reflect changes in lithology. Below the 20-in casing (>207.8 mbsf), a full suite (gamma ray, sonic, resistivity, density, and caliper) of wireline logs was run within the open hole.

In general, low gamma-ray values are attributed to sand-prone lithologies. This is based on the assumption that, in contrast to shales, sands contain few radioactive components. Thus, zones with high gamma-ray values are often qualitatively interpreted to indicate shale-rich sediments, while zones with low gamma-ray values are sand prone. This analysis is simplistic and may not be correct where glauconitic sands are encountered. However, with the exception of the glauconitic sands, this analysis was confirmed by log-core comparison at Site 1071.

The COST-B2 log data suggest sandy to very sandy sediments to ~238 mbsf (Fig. 42). Within this sandy interval, there are two intervals that are more mud prone and/or glauconitic (i.e., higher formation radioactivity), at 50–65 mbsf and 120–170 mbsf. A sharp gamma-ray peak at 137 mbsf suggests a thin radioactive zone within this second, more mud-prone/glauconitic interval. Three of the seismic surfaces examined during Leg 174A lie within this interval (Fig. 42): pp3(s) correlates approximately with the base of the upper interval; pp4(s) approximately correlates with the radioactive spike at 137 mbsf and is likely to be slightly below that level; and pp5(s) correlates approximately with the base of the lower mud-prone/glauconitic interval. As discussed above, traveltime-depth ties are not exact. They are based on checkshot data from Site 1072, which is 3.6 km southeast of Hole 1071A (see Fig. 30); a precise match in depth of data from these two locations should not be expected.

Between 238 and 350 mbsf, a more heterogeneous log profile is observed (Fig. 42). This change lies 20 m beneath the casing point of 208 mbsf and is interpreted to record changing formation properties. This interval was logged in open-hole conditions, and there is a range of log data to examine formation properties.

Between 238 and 320 mbsf, the gamma-ray log records at least four coarsening-upward units capped by abrupt increases in mud/glauconite content (i.e., a gradual decrease followed by an abrupt increase in formation radioactivity; Fig. 42). Very low gamma-ray values are recorded below 318 mbsf; this interval is interpreted to be very sandy. Surfaces m0.5(s) and m1(s) are located approximately within this span (Fig. 42).

The caliper log, from 221 mbsf downward, records a varying borehole diameter that ranges from 13 to 19 in. Large borehole diameters are associated with low gamma-ray (sand-prone) intervals. The bit size was 17.5 in, and the maximum diameter that the caliper tool could record was 19.5 in; much of the log records this maximum value, which suggests that borehole washout occurred in the sand-prone intervals. The presence of washout zones affects log quality. Most suspect are those properties measured with logging tools that
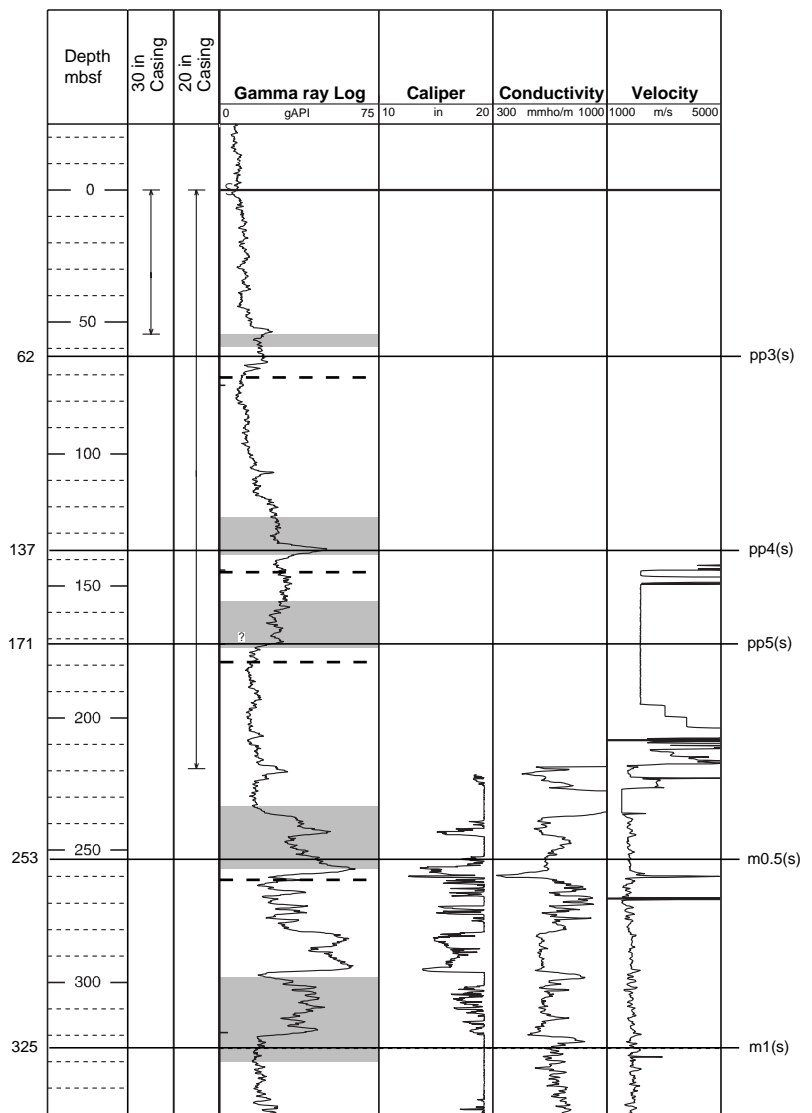
Figure 42. COST-B2 well logs for the depth range 0–350 mbsf. From left to right: casing = the casing present within which the GR log was run; GR = gamma-ray log; Caliper = borehole diameter; Conductivity = electrical conductivity; and Velocity = compressional velocity. Traveltimes to surfaces pp3(s), pp4(s), pp5(s), and m0.5(s), measured from Oc270 Profile 806 in the vicinity of Holes 1071A–1071E, were converted to depths using the checkshot velocity data from Site 1072 (see "Downhole Logging" section, "Site 1072" chapter, this volume). Depth ranges of seismic surfaces superimposed on log character at COST-B2 (shown with gray bars) were calculated from the Oc270 Profile 51 velocity curve (see Table 40). Dashed lines in "Gamma ray Log" column are depths to surfaces calculated using the COST-B2 checkshot velocity function (see Table 40).

require contact with the borehole wall (padded tools), such as the density log.

The conductivity log (Fig. 42) illustrates that sands (low gamma-ray zones) are more electrically conductive than shales. This is expected if the formation fluids are the same composition in both the sands and the shales, because sands have greater permeability due to their larger grain size. There is a slight upward decrease in the conductivity of the sands in the interval 250–350 mbsf (Fig. 42) that may indicate moderate freshening (decreasing salinity). The velocity log suggests that sands have a lower velocity than shales. This may account for the association of significant seismic reflections with lithologic contrasts, because the amplitude of seismic reflections is proportional to the contrast in density and velocity at any acoustic interface (see "Physical Properties" and "Seismic Stratigraphy" sections, this chapter)

Comparison of COST-B2 with Site 1071

The COST-B2 well is only 950 m south-southwest of Site 1071, and not surprisingly, the depths to major seismic horizons at COST-B2 and Site 1071 are very similar down to ~250 mbsf (see "Seismic Stratigraphy" section, this chapter; Fig. 40). Thus, the COST-B2 and Site 1071 holes may record similar characteristics at similar depths.

To compare observations at these two locations, we plot the gamma-ray log from the COST-B2 well adjacent to core data acquired at Site 1071 (Fig. 43).

Core was recovered in Holes 1071A, 1071B, 1071C, and 1071F; however, recovery was low (Fig. 43). Recovery was highest at depths indicated to be more clay rich, according to COST-B2 log data. The exception to this is from 0 to 30 mbsf, where there was good recovery despite the fact that gamma-ray values were low. However, this is the zone that was double-cased (Fig. 42) in COST-B2; the gamma-ray log may not record the formation properties as accurately as where there was only one casing string present. Spectral gamma-ray log data from Hole 1071G (Fig. 38) show considerably greater detail. A moderately strong correlation between high gamma-ray values and core recovery suggests that recovery was biased to shale-prone facies.

Comparison of the COST-B2 gamma-ray log with shipboard natural gamma measurements on unsplit cores (MST; Fig. 44) and with lithostratigraphy from Site 1071 shows that the COST-B2 well is a useful proxy for formation lithology (Fig. 42). Shale-rich, radioactive zones in the core correlate with high gamma-ray values in the COST-B2 well, except near the seafloor at Site 1071 (~10–20 mbsf). Another match to the COST-B2 well is the highly cemented sandstone encountered at ~256 mbsf (Fig. 45). In this narrow bed (<1 m thick),
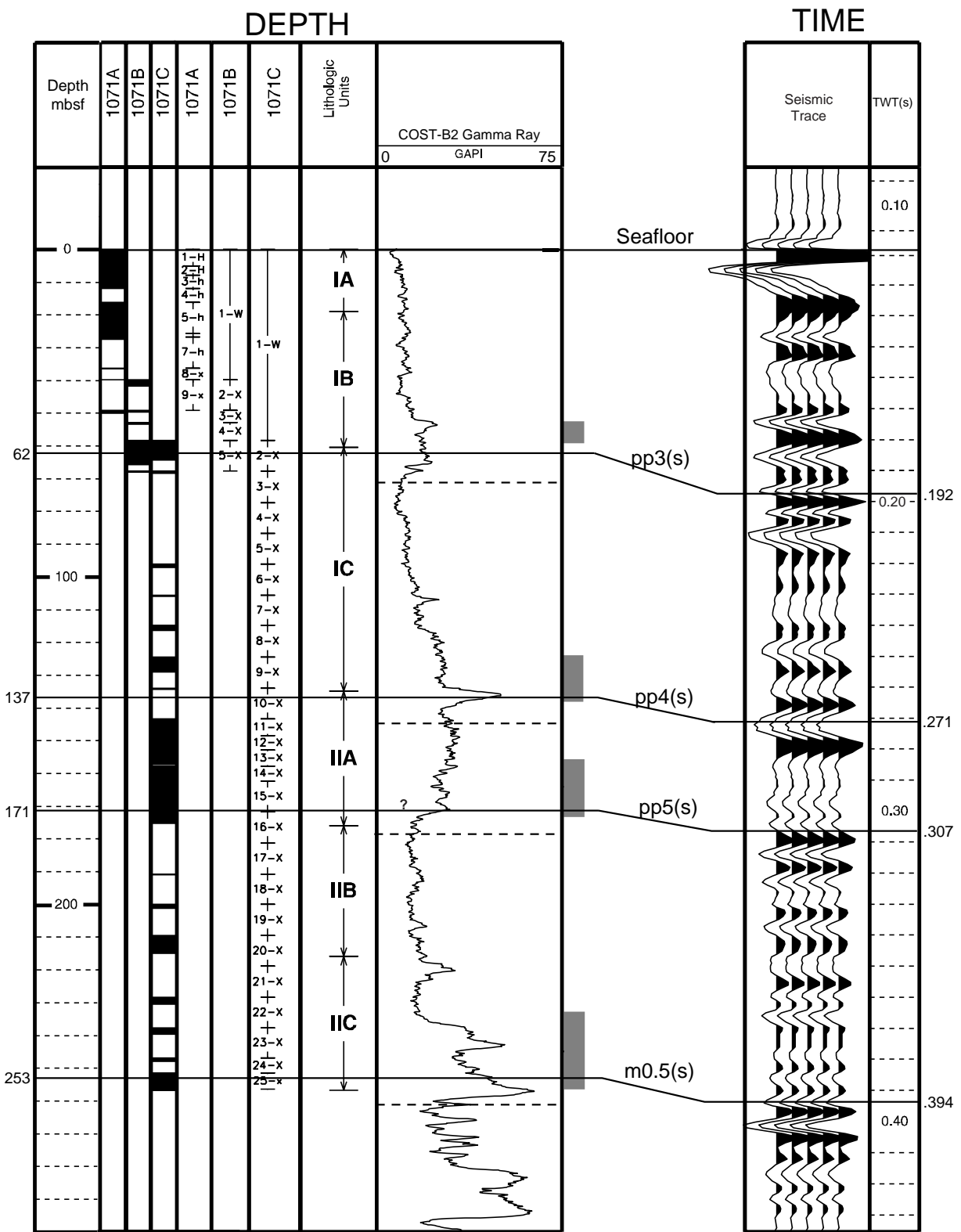
Figure 43. Correlations between depths to features in various boreholes (left) and traveltimes in a seismic profile crossing within a few tens of meters of Hole 1071A (right). Depth below seafloor is in column 1; core recovery, core depths, and lithologic units compose columns 2–8. Gamma-ray log data from COST-B2 (950 m southwest of Hole 1071A) are shown in column 9. The processed seismic trace from Oc270 Profile 806 cdp 10275 is in column 10, and the measured traveltime in seconds below sea level is in column 11 (see Table 40). Lines connecting the depth and time summaries identify four major surfaces that have been tied to the core, log, and seismic records. The vertical gray bars mark calculated depths (±5%) to these surfaces, based on the Oc270 Profile 51 stacking velocities (see Table 40). The horizontal lines that extend to the depth scale at the far left are calculated depths to these surfaces based on checkshot measurements at Site 1072 (see "Down-hole Logging" section, "Site 1072" chapter, this volume). These depths and the traveltimes to the surface are labeled along the left and right edges of the figure, respectively. Depths of surfaces indicated in column 9 (dashed lines) were calculated using the COST-B2 checkshot velocity function (see Table 40; Fig. 42).
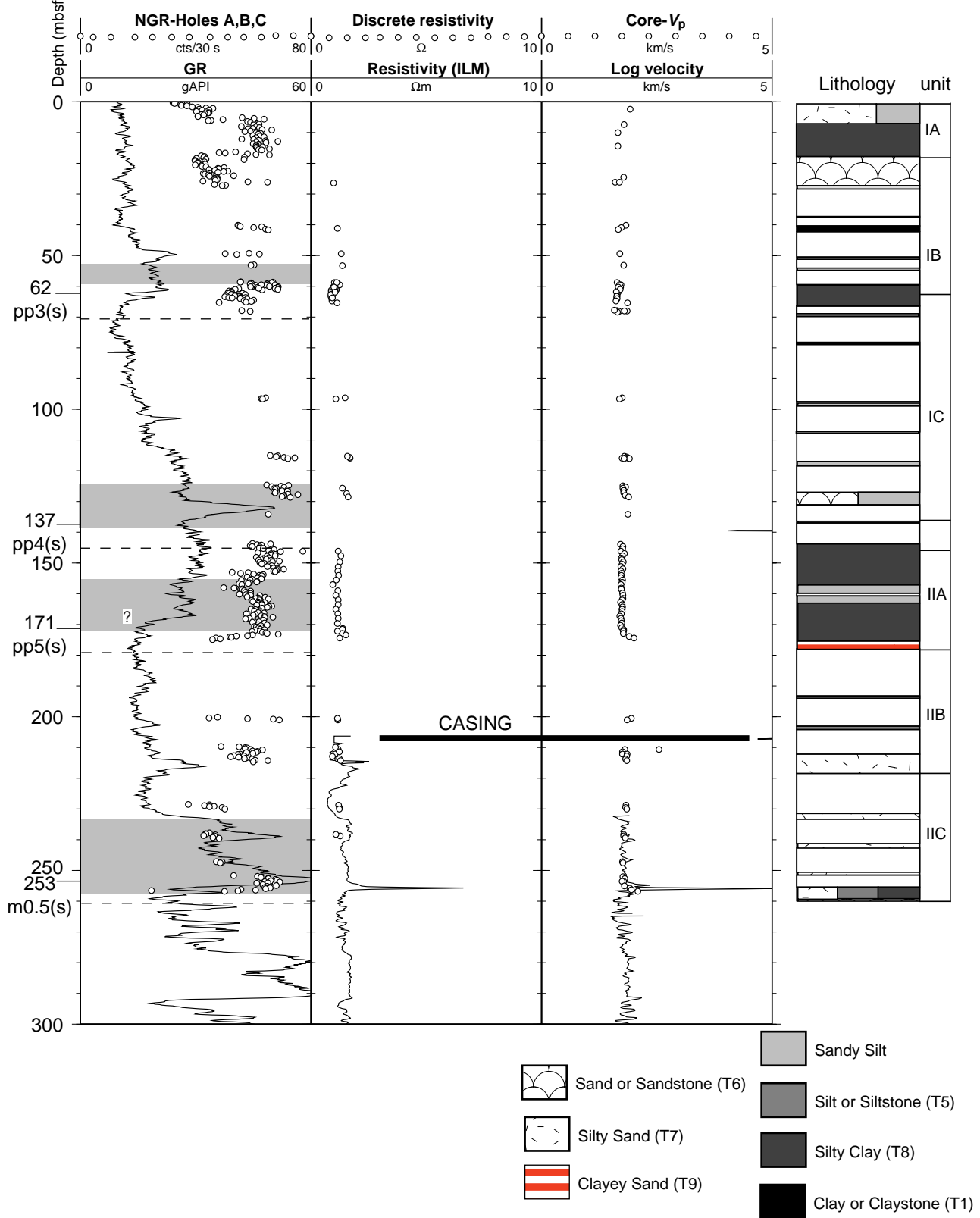
Site 1071 and COST-B2 Well Logs

Figure 44. Comparison of natural GR (MST; units are total counts/30 s), discrete resistivity, and sonic velocity measurements from Holes 1071A, 1071B, and 1071C with wireline logs in the COST-B2 well. Agreement is very good where open-hole logs overlap with the core data. Above casing, the wireline GR is attenuated, but overall trends agree well. The GR peak at 131 mbsf corresponds to a glauconite-rich layer recovered in Core 174A-1071-10X. Seismic surface depths are derived using the Site 1072 checkshot survey (see Table 40). Gray bars represent depth ranges of surfaces calculated using the Oc270 Profile 51 velocity curve (see Table 40). Dashed lines are depths to surfaces calculated from the COST-B2 checkshot velocity function (see Table 40; Figs. 42, 43).
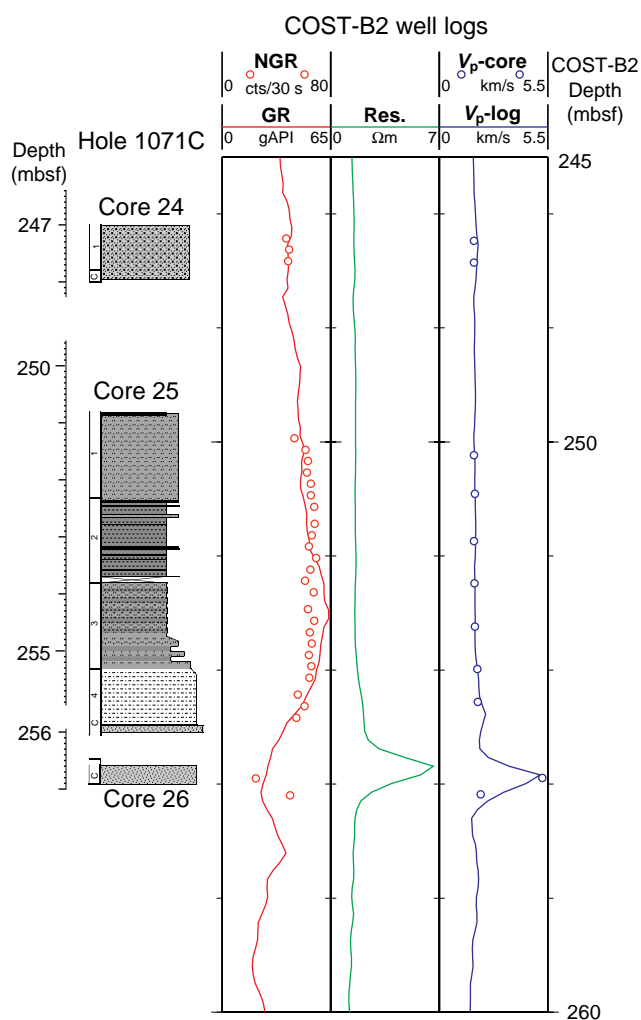
Figure 45. Comparison of lower portion of recovered core in Hole 1071C with COST-B2 well logs. The depth scale to the left is meters below seafloor at Site 1071, and to the right is meters below seafloor at COST-B2. The indurated glauconitic sandstone recovered in Core 174A-1071C-26X is represented by a thin (~1 m) interval of high resistivity and high sonic velocity.

wireline velocities corroborate core-derived velocities of >5 km/s. This indurated, high-velocity interval is indicated by low conductivity in the COST-B2 log at 260 mbsf.

SUMMARY AND CONCLUSIONS

The principal results from Site 1071 are (1) to characterize the late middle Miocene through Pleistocene stratigraphy of the outer shelf of the New Jersey continental margin, (2) to verify the interpretation of four seismically identified offlap surfaces as sequence boundaries of late Miocene and Pliocene–Pleistocene age, (3) to develop a model for the internal architecture of associated sequences, and (4) to place some constraints on variations in paleobathymetry within sequences. The last of these will contribute to ongoing efforts to estimate amplitudes and rates of sea-level change under late Cenozoic Icehouse conditions. Analyses of interstitial waters suggest that distinct observed oscillations of the salinity of pore fluids can be attributed to fluctuations in sea level.

The main elements of the succession are as follows. Unit I (Holocene[?] to lower Pliocene[?]; 0–134.4 mbsf at Holes 1071A and 1071B) consists of sand, silt, and clay that are locally micaceous, glauconitic, fossiliferous, and bioturbated. Unit II (lower Pleistocene

[?] to upper Miocene; 134.4–261.9 mbsf at Holes 1071C and 1071F) is lithologically similar, in places with siderite nodules and cement. Unit III (upper to middle Miocene; 261.9–414.95 mbsf at Hole 1071F) consists predominantly of micaceous sand with minor silt and clay. Sand is poorly represented in recovered samples, and is inferred on the basis of the downhole gamma-ray wireline log for the COST-B2 well (~0.95 km to the south-southwest of Holes 1071A–1071E) and LWD logging to ~88 mbsf at Hole 1071G.

Four surfaces recognized on the basis of prominent offlap in seismic reflection data, and tentatively interpreted as sequence boundaries, were penetrated at Site 1071: pp3(s), pp4(s), m0.5(s), and m1(s). Surface pp3(s) is interpreted in Holes 1071B and 1071C at ~61 mbsf (at 61.4 mbsf in Core 174A-1071B-5X-3 and at 60.9 mbsf in Core 1071C-2X-2). This is very close to the depth predicted from traveltimes, using both semblance velocities from Oc270 seismic reflection data and checkshot data obtained at Site 1072 (53–59 and 62 mbsf, respectively) for traveltime-depth conversion. Surface pp3(s) is characterized by abrupt upward coarsening from homogeneous, burrow-mottled silty clay with scattered pebbles and granules to thoroughly bioturbated fine- to medium-grained glauconitic quartz sand; pp3(s) is also associated with an interval of upward-increasing density, velocity, and resistivity (~65–59 mbsf), and an abrupt upward decrease in shear strength. Surface pp3(s) is tentatively interpreted at 65 mbsf in Hole 1071G, at the top of a 2-m coarsening-upward interval. This is consistent with predicted depths to pp3(s) at that location (55–61 and 64 mbsf, from seismic reflection and checkshot data for Site 1072, respectively).

In the absence of logging data at Site 1071 at depths >88 mbsf, the other three surfaces are less precisely located in depth. Surface pp4(s) is interpreted within an unsampled interval between 134.34 and 143.5 mbsf (Cores 174A-1071C-10X and 11X), consistent with depths predicted from traveltimes using Oc270 semblance velocities and checkshot data from Site 1072 (124-138 and 137 mbsf, respectively). Sediments above the boundary (Core 174A-1071C-10X) are composed of fine-grained glauconitic sand with pebbles and scattered shells, consistent with a prominent excursion in the gamma-ray log for the COST-B2 well at 137 mbsf. Sediments recovered from below pp4(s) at Site 1071 consist of silty clay with rare quartz pebbles (Core 174A-1071C-11X). Surface m0.5(s) is tentatively interpreted at a depth of >256.74 mbsf at Hole 1071C, the deepest core obtained at that location (Core 174A-1071C-26X), and in an unsampled interval between 261.90 and 320.2 mbsf in Hole 1071F (Cores 174A-1071F-2R and 6R). These depths are generally consistent with predicted depths of 233–257 (from semblance velocities) and 253 mbsf (from Site 1072 checkshot data) for Hole 1071C, 247–273 (from semblance velocities) and 269 mbsf (from Site 1072 checkshot data) for Hole 1071F, and with the presence in Core 174A-1071C-26X of abundant glauconite, a mineral that at the New Jersey margin tends to be concentrated in transgressive marine deposits above sequence boundaries, but which is less common below (Pekar and Miller, 1996). Surface m1(s) was intersected at only one location (Hole 1071F); predicted depths for m1(s) at this location are 372–412 (from semblance velocities) and 405 mbsf (from Site 1072 checkshot data), within a very poorly sampled sandy interval between Cores 174A-1071F-11R and 15R. The depth of m1(s) cannot be evaluated with certainty with data acquired at Site 1071.

A fifth seismic surface (pp5[s]), tentatively interpreted prespud as a sequence boundary, is reinterpreted as a flooding surface or interval of upward deepening. The pp5(s) surface is characterized in seismic reflection data by a marked change in seismic facies from a unit below with laterally persistent high-amplitude reflections to a unit above that is comparatively featureless. Unlike the other surfaces described above, pp5(s) is not associated with offlap; apparently onlapping reflections that represented the main evidence for the pp5(s) interpretation as a sequence boundary may instead be peg-leg multiples. The depths of pp5(s) at Hole 1071C predicted from traveltimes using Oc270 semblance velocities and checkshot data from Site 1072 are 156–172 and 171 mbsf, respectively. The principal facies change

at these depths is an upward transition at ~173.5 mbsf from bioturbated muddy sand with scattered pebbles and shells to homogeneous silty clay with shell fragments.

These five surfaces are not well dated at Site 1071. This is related to (1) the absence of age-diagnostic fossils, because of carbonate dissolution during burial and shallow-water conditions of sedimentation that were unfavorable to planktonic marine organisms; (2) intermittent poor sediment recovery; and (3) because marked seismic offlap at interpreted sequence boundaries implies the presence of a significant hiatus in shallow shelf locations. Our best estimates of ages at Site 1071 are as follows (see Fig. 16). Surface pp3(s) is <0.9 Ma on the basis of nannofossils and <0.78 Ma from the interpreted position of the Brunhes/Matuyama magnetopolarity boundary (10 cm below pp3[s] at Hole 1071B and 40–50 cm below this surface at Hole 1071C). Surface pp4(s) is dated as 1.4–7.4 Ma on the basis of dinocysts. Surface pp5(s) is dated as 5.9–7.4 Ma (dinocysts), with an upper age limit as young as 5.2 Ma if the surface is located above 163.11 mbsf (not the preferred interpretation). That is, it is of late Miocene age, and not Pliocene–Pleistocene, as indicated by its informal "pp" designation (see "Introduction" chapter, this volume). The estimated ages of m0.5(s) and m1(s) are also sensitive to their precise stratigraphic location. Assuming the predicted depths of 253 mbsf at Hole 1071C and 269 mbsf at Hole 1071F, m0.5(s) is dated as 5.9–8.6 Ma at Hole 1071C (dinocysts) and >7.4 Ma at Hole 1071F (dinocysts and planktonic foraminifers), a combined range of 7.4–8.6 Ma. Assuming the preferred depth for m0.5(s) at Hole 1071C (>256.74 mbsf), m0.5(s) is >8.6 Ma. If m0.5(s) is between 255.04 and 261.85 mbsf at Hole 1071F, its age is 7.4–9.2 Ma; and if <255.04 mbsf at this location, its age is <8.6 Ma. The last possibility is not consistent with the preferred interpretation at Hole 1071C, both because the surface cannot be simultaneously >8.6 Ma and <8.6 Ma, and because the interpreted seismic boundary appears to be deeper at Hole 1071F than it is at Hole 1071C (see Table 40 and Fig. 37). The most conservative interpretation, taking into account these various possibilities, is that m0.5(s) is >7.4 Ma and probably >8.6 Ma. Assuming a predicted depth of 405 mbsf at Hole 1071F, m1(s) is >11.4 Ma (planktonic foraminifers). If deeper than 405.57 mbsf, it is >12.5 Ma. This older age is not consistent with existing constraints on the age of m1(s) (11.0–11.9 Ma; Miller et al., in press).

Several lines of evidence support the interpretation of pp3(s), pp4(s), m0.5(s), and m1(s) as sequence boundaries: (1) all are associated with marked offlap landward of their respective rollovers/breakpoints and onlap seaward of this position; (2) surfaces pp3(s), pp4(s), and m0.5(s) appear to be characterized by hiatuses, possibly significant; and (3) surface pp4(s) is associated with a marked discontinuity in facies, with pebbly sand abruptly overlying silty clay. Paleobathymetry from benthic foraminifers, combined with physical sedimentology, indicate marked shoaling at this level, from middle neritic (50–100 m) below to inner neritic (0–50 m) above. Facies discontinuities of this sort require the lowering of depositional base level, which is a hallmark of sequence boundaries, and expected for surfaces that are potentially related to rapid and/or large-amplitude glacial-eustatic lowering of sea level. In contrast, surface pp5(s) lacks all of the above characteristics, and appears to be associated with upward deepening.

The overall arrangement of facies within the sequences bounded by surfaces m0.5(s) and pp4(s) and between pp4(s) and pp3(s) differs from our expectations (Greenlee et al., 1992). The lower part of each sequence is comparatively sandy, thins seaward (seismic geometry), and appears to have accumulated in shallower water than the finer grained sediments above. Progradational (highstand) sediments expected beneath these sequence boundaries appear to be poorly developed or absent at Site 1071. These observations lead to the following hypothesis. During times of sea-level rise, the sediment supply was sufficient to fill any available accommodation (a "keep-up" situation), with highstand progradation possible only seaward of the rollover/breakpoint in the underlying sequence boundary. A testable cor-

ollary of this interpretation is that shallow-water sandy sediments ought to be comparatively thick beneath sequence boundary rollovers/breakpoints (for example, at the level of m0.5[s] at Site 1072). An important implication is that the observed offlap at sequence boundaries on the New Jersey margin may be primarily the result of sediment bypassing and gradual development of the surfaces, rather than erosional truncation during short-lived falls in sea level. Some erosion cannot be excluded, but the absence of evidence for significant valley incision in margin-parallel seismic profiles (e.g., Fulthorpe and Austin, 1998) suggests that most erosion took place in a shallow-marine setting during either regression of the shoreline or subsequent transgression.

Observations at Site 1071 place constraints on the amplitudes of water-depth changes within sequences. As indicated above, maximum water depths in the late Miocene were ~50–100 m (benthic foraminifers). The minimum water depth may be associated with an unusual facies observed in Core 174A-1071F-2R (261.48–261.9 mbsf), most likely close to but a few meters above sequence boundary m0.5(s), and no more than 3 km landward of the rollover/breakpoint for this surface. This interval consists of carbonaceous silty clay, with organic detritus scattered throughout but locally concentrated in thin laminated beds 1–2 cm thick (Fig. 11). Unlike much of the fine-grained sediment at Site 1071, this core lacks bioturbation, is virtually barren of planktonic foraminifers and dinocysts, and instead contains abundant pollen and fungal spores. Taken together, these observations imply a lagoonal or estuarine environment of deposition. During development of sequence boundary m0.5(s), the shallow shelf appears to have become subaerially exposed to a point within 3 km of its rollover/breakpoint. Water-depth changes within the overlying sequences were on the order of 50–100 m.

Interstitial water profiles at Site 1071 show the distinct influence of sea-level fluctuations. Pore fluids are significantly fresher than seawater in two intervals. At 26.45 mbsf, Cl⁻ drops to 430 mM (a 23% decrease), and at 321 mbsf to 500 mM (an 11% decrease). These salinity minima may reflect oscillations in the salinity of overlying waters during Pliocene–Pleistocene time. During times of lowered sea level and subaerial exposure of the shelf, fresh (or brackish) water was introduced into the sediment. Renewed flooding led to a return of normal marine salinity at the sediment surface.

REFERENCES

Austin, J.A., Jr., Mountain, G.S., Christie-Blick, N., and Miller, K.G., 1996. Deciphering the sea-level history of the Icehouse: continuation of the New Jersey Transect. *Eos,* 77:F330.

Baker, P.A., and Burns, S.J., 1985. The occurrence and formation of dolomite in organic-rich continental margin sediments. *AAPG Bull.,* 69:1917–1930.

Berggren, W.A., Kent, D.V., Swisher, C.C., III, and Aubry, M.-P., 1995. A revised Cenozoic geochronology and chronostratigraphy. *In* Berggren, W.A., Kent, D.V., Aubry, M.-P., and Hardenbol, J. (Eds.), *Geochronology, Time Scales and Global Stratigraphic Correlation.* SEPM (Soc. Sediment. Geol.), 54:129–212.

Buck, K.F., and Olson, H.C., in press. *Elphidium* faunas of the New Jersey shelf: implications for sea-level fluctuations during late Quaternary glaciation. *J Foraminiferal Res.*

Chaisson, W.P., and Leckie, R.M., 1993. High-resolution Neogene planktonic foraminifer biostratigraphy of Site 806, Ontong Java Plateau (western equatorial Pacific). *In* Berger, W.H., Kroenke, L.W., Mayer, L.A., et al., *Proc. ODP, Sci. Results,* 130: College Station, TX (Ocean Drilling Program), 137–178.

Christie-Blick, N., Miller, K.G., Mountain, G.S., Driscoll, N.W., Reynolds, D.J., and Steckler, M.S., 1992. Sequence stratigraphy and sea-level change: examples from the Atlantic margins of the U.S. and Canada. In *The Tectonics, Sedimentation and Palaeoceanography of the North Atlantic Region.* Geol. Soc. London, Mar. Studies Group.

Compton, J.S., 1988. Degree of supersaturation and precipitation of organogenic dolomite. *Geology,* 16:318–321.

de Verteuil, L., and Norris, G., 1996. Miocene dinoflagellate stratigraphy and systematics of Maryland and Virginia. *Micropaleontology,* 42 (Suppl.).

Ellison, R.L., and Nichols, M.N., 1976. Modern and Holocene foraminifera in the Chesapeake Bay region. *In* Schafer, C.T., and Pelletier, (Eds.), *First International Symposium on Benthonic Foraminifera of Continental Margins*, (Pt. A). Maritime Sediment., Spec. Publ., 1:131–151.

Fulthorpe, C.S., and Austin, J.A., Jr., 1998. Anatomy of rapid margin progradation: three-dimensional geometries of Miocene clinoforms, New Jersey margin. *AAPG Bull.*, 82:251–273.

Gieskes, J.M., 1983. The chemistry of interstitial waters of deep-sea sediments: interpretation of deep-sea drilling data. *In* Riley, J.P., and Chester, R. (Eds.), *Chemical Oceanography* (Vol. 8): London (Academic), 221–269.

Gieskes, J.M., Gamo, T., and Brumsack, H., 1991. Chemical methods for interstitial water analysis aboard *JOIDES Resolution. ODP Tech. Note,* 15.

Greenlee, S.M., Devlin, W.J., Miller, K.G., Mountain, G.S., and Flemings, P.B., 1992. Integrated sequence stratigraphy of Neogene deposits, New Jersey continental shelf and slope: comparison with the Exxon model. *Geol. Soc. Am. Bull.,* 104:1403–1411.

Hathaway, J.C., et al., 1979. U.S. Geological Survey core drilling on the Atlantic shelf. *Science*, 106:515–527.

Keigwin, L.D., Rio, D., Acton, G.D., et al., 1998. *Proc. ODP, Init. Repts.,* 172: College Station, TX (Ocean Drilling Program).

Kohout, F.A., Meisler, H., Meyer, F.W., Johnston, R.H., Leve, G.W., and Wait, R.L., 1988. Hydrogeology of the Atlantic continental margin. *In* Sheridan, R.E., and Grow, J.A. (Eds.), *The Geology of North America* (Vol. I-2): *The Atlantic Continental Margin, U.S.* Geol. Soc. Am., 463–480.

McCracken, S.R., Compton, J., and Hicks, K., 1996. Sequence-stratigraphic significance of glaucony-rich lithofacies at Site 903. *In* Mountain, G.S., Miller, K.G., Blum, P., Poag, C.W., and Twichell, D.C. (Eds.), *Proc. ODP, Sci. Results,* 150: College Station, TX (Ocean Drilling Program), 171–187.

Miller, K., Rufolo, S., Sugarman, P., Pekar, S., Browning, J., and Gwynn, D., 1997. Early to middle Miocene sequences, systems tracts, and benthic foraminiferal biofacies, New Jersey coastal plain. *In* Miller, K.G., and Snyder, S.W. (Eds.), *Proc. ODP, Sci. Results,* 150X: College Station, TX (Ocean Drilling Program), 169–186.

Miller, K.G., Mountain, G.S., Blum, P., Gartner, S., Alm Per, G., Aubry, M.-P., Burckle, L.H., Guerin, G., Katz, M.E., Christensen, B.A., Compton, J., Damuth, J.E., Deconinck, J.F., de Verteuil, L., Fulthorpe, C.S., Hesselbo, S.P., Hoppie, B.W., Kotake, N., Lorenzo, J.M., McCracken, S., McHugh, C.M., Quayle, W.C., Saito, Y., Snyder, S.W., ten Kate, W.G., Urbat, M., Van Fossen, M.C., Vecsei, A., Sugarman, P.J., Mullikin, L., Pekar, S., Browning, J.V., Liu, C., Feigenson, M.D., Goss, M., Gwynn, D., Queen, D.G., Powars, D.S., Heibel, T.D., and Bukry, D., 1996. Drilling and dating New Jersey Oligocene-Miocene sequences: ice volume, global sea level, and Exxon records. *Science,* 271:1092–1095.

Miller, K.G., Mountain, G.S., Browning, J.V., Kominz, M., Sugarman, P.J., Christie-Blick, N., Katz, M.E., and Wright, J.D., in press. Cenozoic global sea level, sequences, and the New Jersey Transect: results from coastal plain and continental slope drilling. *Rev. Geophys.*

Mountain, G.S., Miller, K.G., Blum, P., et al., 1994. *Proc. ODP, Init. Repts.,* 150: College Station, TX (Ocean Drilling Program).

Mountain, G.S., Miller, K.G., Christie-Blick, N., and Austin, J.A., Jr., 1996. Ages and architecture of Neogene sequences, New Jersey shelf and slope: ODP Legs 150 and 174A. *Eos,* 77:S162.

Oda, H., and Shibuya, H., 1996. Deconvolution of long-core paleomagnetic data of Ocean Drilling Program by Akaike's Bayesian Information Criterion minimization. *J. Geophys. Res.*, 101:2815–2834.

Pekar, S.F., and Miller, K.G., 1996. New Jersey Oligocene "Icehouse" sequences (ODP Leg 150X) correlated with global $\delta^{18}O$ and Exxon eustatic records. *Geology,* 24:567–570.

Poag, C.W., Knebel, H.J., and Todd, R., 1980. Distribution of modern benthonic foraminifers on the New Jersey Outer Continental Shelf. *Mar. Micropaleontol.,* 5:43–69.

Scholle, P.A. (Ed.), 1977. Geological studies on the COST No. B-2 well, U.S. mid-Atlantic outer continental shelf area. *Geol. Surv. Circ. (U.S.),* 750.

Shipboard Scientific Party, 1994a. Site 902. *In* Mountain, G.S., Miller, K.G., Blum, P., et al., *Proc. ODP, Init. Repts.,* 150: College Station, TX (Ocean Drilling Program), 63–127.

————, 1994b. Site 906. *In* Mountain, G.S., Miller, K.G., Blum, P., et al., *Proc. ODP, Init. Repts.,* 150: College Station, TX (Ocean Drilling Program), 309–357.

————, 1995. Explanatory notes. *In* Curry, W.B., Shackleton, N.J., Richter, C., et al., *Proc. ODP, Init. Repts.,* 154: College Station, TX (Ocean Drilling Program), 11–38.

————, 1996a. Explanatory notes. *In* Comas, M.C., Zahn, R., Klaus, A., et al., *Proc. ODP, Init. Repts.,* 161: College Station, TX (Ocean Drilling Program), 21–49.

————, 1996b. Site 960. *In* Mascle, J., Lohmann, G.P., Clift, P.D., et al., *Proc. ODP, Init. Repts.,* 159: College Station, TX (Ocean Drilling Program), 151–215.

————, 1996c. Site 976. *In* Comas, M.C., Zahn, R., Klaus, A., et al., *Proc. ODP, Init. Repts.,* 161: College Station, TX (Ocean Drilling Program), 179–297.

————, 1996d. Site 979. *In* Comas, M.C., Zahn, R., Klaus, A., et al., *Proc. ODP, Init. Repts.,* 161: College Station, TX (Ocean Drilling Program), 389–426.

Smith, M.A., Amato, R.V., Furbush, M.A., Pert, D.M., Nelson, M.E., Hendrix, J.S., Tamm, L.C., Wood, G., Jr., and Shaw, D.R., 1976. Geological and operational summary, COST No. B-2 Well, Baltimore Canyon Trough Area, Mid-Atlantic OCS. *Open-File Rep., U.S. Geol. Surv.,* 76–174:79.

Snyder, S.W., Waters, V.J., and Moore, T.L., 1989. Benthic foraminifera and paleoecology of Miocene Pungo River Formation sediments in Onslow Bay, North Carolina continental shelf. *In* Snyder, S.W. (Ed.), *Micropaleontology of Miocene Sediments in the Shallow Subsurface of Onlow Bay, North Carolina Continental Shelf.* Spec. Publ. Cushman. Found. Foraminiferal Res., 25:43–96.

Urbat, M., 1996. Rock-magnetic properties of Pleistocene passive margin sediments: environmental change and diagenesis offshore New Jersey. *In* Mountain, G.S., Miller, K.G., Blum, P., Poag, C.W., and Twichell, D.C. (Eds.), *Proc. ODP, Sci. Results,* 150: College Station, TX (Ocean Drilling Program), 347–359.

Ms 174AIR-103

NOTE: Core-description forms ("barrel sheets") and core photographs can be found in Section 3, beginning on page 195. Thin-section descriptions, smear-slide data, and shore-based log processing data can be found on CD-ROM (back pocket of this volume). See Table of Contents for material contained on CD-ROM.